2021

EXPERIMENTAL EVALUATION AND SIMULATION OF TORQUE TRANSMISSIBILITY FREQUENCY RESPONSE FUNCTIONS OF VIBRATION ISOLATORS AND ABSORBERS FOR DRIVETRAIN APPLICATIONS

Luke Jurmu
Michigan Technological University, ljurmu@mtu.edu

EXPERIMENTAL EVALUATION AND SIMULATION OF TORQUE TRANSMISSIBILITY FREQUENCY RESPONSE FUNCTIONS OF VIBRATION ISOLATORS AND ABSORBERS FOR DRIVETRAIN APPLICATIONS

By

Luke W. Jurmu

A DISSERTATION

Submitted in partial fulfillment of the requirements for the degree of

DOCTOR OF PHILOSOPHY

In Mechanical Engineering-Engineering Mechanics

MICHIGAN TECHNOLOGICAL UNIVERSITY

2021

This dissertation has been approved in partial fulfillment of the requirements for the Degree of DOCTOR OF PHILOSOPHY in Mechanical Engineering-Engineering Mechanics.

Department of Mechanical Engineering-Engineering Mechanics

Dissertation Advisor:	*Darrell Robinette*
Committee Member:	*Jason Blough*
Committee Member:	*James De Clerck*
Committee Member:	*David Labyak*
Department Chair:	*William W. Predebon*

Table of Contents

List of Figures

List of Tables

Author Contribution Statement

Chapters 1 and 6 were written by the dissertation author.

Chapter 2 is the initial submission to the Journal of Vibration and Control. This article was published in 07/2020.

Chapters 3-5 are drafts of articles to be submitted for publication in January 2022.

All articles were written in collaboration with the listed authors.

Acknowledgements

Thank you God for all your blessings: for the love and support, world class mentorship, good and bad luck, embarrassing mistakes, and amazing opportunities.

Thanks to the project sponsor, GM, for sponsoring this research. Thanks to Jean Schweitzer, Mike Grimmer, Mark Gehringer, and Craig Reynolds. You've all played an active part in my development as an engineer.

Thanks to Darrell Robinette and Jason Blough for offering me the opportunity to work in the torque converter test cell, and for asking hard questions in weekly meetings. You guys have played the most active role in my development as a researcher.

Thanks to Ari Pitkänen, who provided me with excellent design experience, and whose flexibility allowed me to work remote, and earn extra income in the initial year of graduate school. It made a huge difference!

Thanks to Eric Little and Jim De Clerck, who opened the doors of opportunity for me at Michigan Tech.

I have reserved my last thank you to my wife Tiffany, who made the largest sacrifice—moving away from friends and family, and taking a pay cut—in supporting me in achieving a PhD. I love you so much honey!

Abstract

Four studies involving torsional vibration isolation performance of automotive drivetrain components, make up this dissertation. One study features a prototype planetary torsional vibration absorber, a unique device that targets low frequency torsion modes in automotive drivetrains. Two studies feature experiments on several torque converters, clutch locked and open, to validate models of the hardware. The last study details experiments on a centrifugal pendulum absorber in a torque converter, to characterize the viscous friction while submerged in automatic transmission fluid (ATF). The enclosed studies improve the state of the art of drivetrain vibration absorbers and isolators, by introducing a new vibration absorber concept and increasing understanding of the underlying physics of torque converters, lock-up clutch dampers, and centrifugal pendulum absorbers.

The design and test of the planetary torsional vibration absorber concept demonstrated the utility of a gear reduction in increasing the apparent inertia of the absorber. By increasing its apparent inertia, the device successfully attenuated a ~20 Hz mode of vibration, and used less packaging volume and mass than a traditional torsional vibration absorber of equivalent performance.

Various lockup clutch designs were characterized with torque transmissibility frequency response function (TTFRF) measurements while spinning at simulated vehicle operating conditions. This in situ testing lent itself useful in characterizing the speed dependent friction in a lockup clutch damper, while also confirming other damper parameters—like stiffness and damping.

The torque converters were also tested in open mode (lockup clutch not engaged). The open mode testing revealed that the hydrodynamic torque converter transmits enough torsional vibration to excite the damper mode for the turbine damper architectures. The open clutch testing contributes a complete data set—encompassing a wide range of speed ratios—to verify torque converter models with. When comparing the test TTFRFs to model TTFRFs, a discrepancy in the damper mode's natural frequency was revealed, and it was hypothesized that this error resulted from a reflected inertia effect of the ATF undergoing toroidal flow.

The locked clutch testing provoked some questions about the centrifugal pendulum absorber (CPA)—a component of one of the tested torque converter clutch dampers. To validate an existing CPA model, and to characterize the equivalent viscous damping of the CPA mechanism, TTFRFs of custom made torque converters were measured. The custom hardware included: pinned damper (CPA active), pinned CPA (damper active), and pinned straight spring (CPA and arc spring active). The torques due to friction and viscous damping of the damper were effectively eliminated from the CPA, and the equivalent viscous damping of the CPA characterized.

1 Introduction

1.1 Automotive Industry Trends

As the title of this dissertation implies, this research concerns passive vibration control in vehicle drivetrains, and concerns torque converters, their lockup clutch dampers, CPAs, and a prototype vibration absorber. Internal combustion engines (ICE) produce large amplitude torque oscillations which need attenuation to preserve durability and passenger comfort. While automotive markets move toward increased electric vehicle (EV) market share, the current market share indicates further use of ICE technology in the near term [1]. Although efforts to develop EV technology are important to reduce environmental impact of transportation sector, further development on ICE powertrains is also merited in the interim.

Technologies employed to improve efficiency of modern ICE powertrains include: cylinder deactivation, hybridization, reduced number of cylinders, turbocharging, increased number of gears, and aggressive torque converter clutch apply. These fuel saving strategies increase the torsional vibration amplitudes while also reducing the frequency of said torsionals. Vibration isolators and absorbers are deployed to attenuate torsional vibrations. Widely used torsional vibration isolators in vehicle powertrains include dual mass fly wheels, torque converters, and lock-up clutch dampers. Examples of torsional vibration absorbers for drivetrain applications include centrifugal pendulum absorbers and turbine tuned mass dampers [2]. In the name of attenuating drivetrain torsional vibrations, this research introduces a unique torsional vibration absorber, quantifies speed dependent friction phenomena in torque converter lockup clutch dampers, evaluates the accuracy of a physics based hydrodynamic torque converter model, and quantifies the equivalent viscous friction of a centrifugal pendulum absorber in a torque converter lockup clutch damper.

1.2 Passive Torsional Vibration Control

When considering vibration problems, consider the source-path-receiver paradigm. Where the source inputs forces to the structure, the path transmits forces, and the receiver perceives the forces. Applying this to an automobile, the ICE (source) inputs forces and torques to the vehicle structure, the forces and torques get transmitted through the drivetrain and chassis structure (path), and the passengers feel vibrations in the seats (receiver).

Vibration isolators and absorbers modify the path of the transmitted forces with the intent of attenuating the received vibrations. Isolators take advantage of the fact that resonant systems attenuate vibrations beyond resonance, and absorbers attenuate vibrations of a specific frequency [3]. With a known frequency range of force inputs, an isolator can be designed to attenuate the incoming forces. This is achieved by placing a spring-damper between the source and the path (force/structure). In the case of a vehicle's drivetrain, the engine produces torsional and translational vibrations. To attenuate the torsional

vibrations from the engine, the isolator needs to have a natural frequency lower than engine firing frequency. Figure 1.1 illustrates the attenuation region of a generic, single degree of freedom (SDOF) torsional system. The torque transmissibility frequency response function (TTFRF) shows the resonant peak of the system and the shaded region indicates frequencies where torque is attenuated.

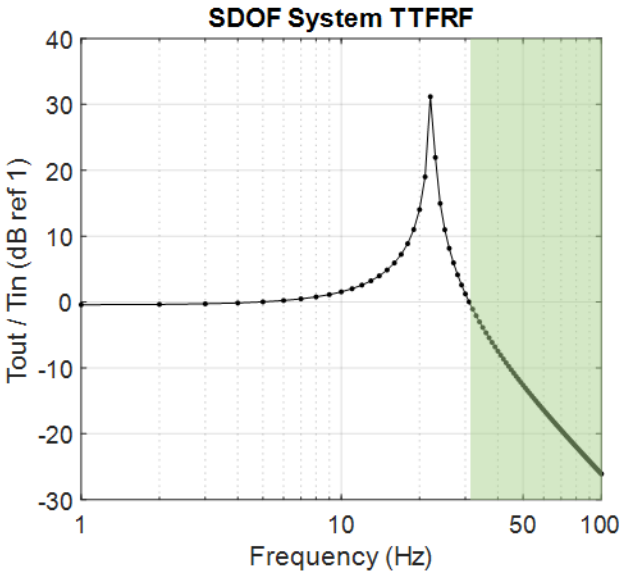

Figure 1.1. Vibrations attenuated beyond 30 Hz (shaded region).

Vibration absorbers target a specific frequency, and can successfully eliminate a troublesome frequency or mode of vibration. Starting with a single degree of freedom (SDOF) system, an attached vibration absorber attenuates vibration of the system at the absorber's natural frequency. A properly tuned absorber divides the vibration energy of the original resonant peak into two, lower amplitude resonances (Figure 1.2). The amplitude of both peaks are the same amplitude with optimized absorber tuning.

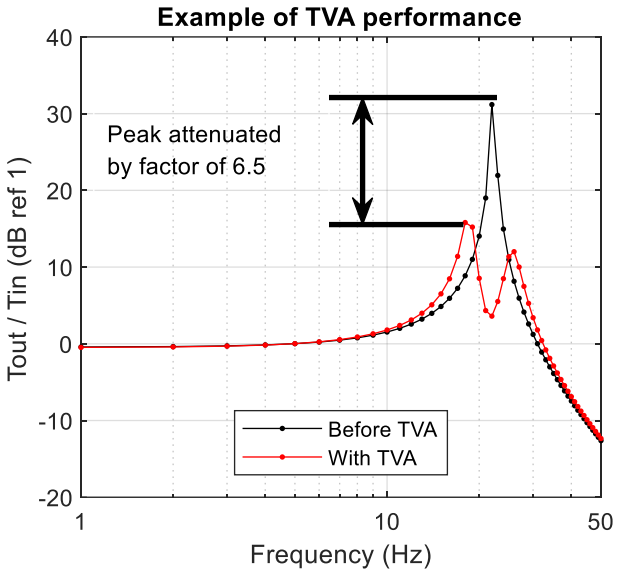

Figure 1.2. Example plot of torsional vibration absorber (TVA) performance. The peak vibration amplitude reduced by a factor of 6.5. More attenuation achieved at the natural frequency of the TVA (22 Hz).

Torsional vibrations in vehicle drivetrains are primarily order based—frequency depends on rotational velocity. The CPA, a torsional vibration absorber tuned to order rather than frequency, provides a robust solution for attenuating engine vibrations when tuned to engine firing order. To visualize how the CPA works, first consider a gravitational pendulum (ex. grandfather clock). A gravitational pendulum has a natural frequency of $\sqrt{g/l}$, where g is gravitational acceleration and l is the length of the pendulum. For a pendulum mounted to a rotating disc (centrifugal pendulum), centrifugal acceleration pulls the pendulum masses out radially. The centrifugal pendulum has a different natural frequency equation than the gravitational pendulum.

$$\omega_n = \sqrt{\frac{\Omega^2 R}{B}} = \Omega\sqrt{\frac{R}{B}}$$

The centrifugal acceleration term ($\Omega^2 R$, where Ω is the rotational velocity of the disc, and R the mounting radius of the pendulum) replaces the gravitational acceleration, and B is the radius of the pendulum motion. As rotational velocity of the disc increases, the centrifugal acceleration on the pendulum increases, thus increasing the natural frequency of a centrifugal pendulum. R and B are then designed to achieve a natural frequency that tracks with engine firing order. A centrifugal pendulum tuned to absorb a particular order of excitation is a CPA.

1.3 Literature Review

The four contributions presented in this dissertation build on past research involving tuned mass dampers, clutch dampers, hydrodynamic torque converters, and centrifugal pendulum absorbers (CPA). A prototype of a planetary torsional vibration absorber (pTVA) demonstrates the utility of a planetary gear set in attenuating low frequency torsional vibrations. The other research concerns torque converter specific hardware, and utilizes a torsional vibration test setup to improve the accuracy of physical hardware models.

1.3.1 Planetary Torsional Vibration Absorber

The fundamental vibration absorber theory at the heart of the pTVA was published in 1956 by Den Hartog [3]. Vibration absorbers have a wide range of applications, and have been used for automotive applications. Examples of automotive torsional vibration absorbers are the turbine tilger (German for tuned mass damper) and the centrifugal pendulum absorber [2, 4]. Besides the use of torsional vibration absorbers, isolators in the form of dual mass flywheels, torque converters, and clutch dampers, are also widely deployed to attenuate torsional vibrations in automotive drivetrains [5]. Yet another body of research in the vibration absorber space is the tuned mass damper inerter (TMDI) [6-8]. Inerters were developed in 2002 by Smith [8], and are a mechanical equivalent to a capacitor. While the pTVA was not designed in the context of an inerter, the planetary gear set lends itself useful in potential TMDI applications [6, 8, 9]. The pTVA was patented in 2019 [10], and an article detailing the design and test of the pTVA published in 2020 [11]. This article constitutes chapter 2 of this dissertation.

1.3.2 Torque Converter Clutch Damper

Torque converter clutch dampers have been widely modelled in vehicle powertrain models to solve a variety of vibrations problems [12-19]. Experimental data of the torque converter clutch (TCC) separate from other drivetrain components validates TCC models, and TCCs have been characterized separate from other drivetrain dynamics in other unique test setups. For example, a pluck test rig and a torsional pulse generator using an ICE were deployed to characterize torque converter dynamics [20-22]. In other research, a spinning torque converter test setup was used to measure torque transmissibility of TCC dampers[23-25]. The test results in these articles were limited in the frequency range of excitation (not all of the dampers tested had the resonance experimentally characterized), and in the number of tested operating speeds. No efforts to estimate physical damper parameters from the test data were made. Chapter 3 details experimental torque transmissibility measurements made at sever operating speeds, and the subsequent parameter estimation.

1.3.3 Hydrodynamic Torque Converter

A physics based torque converter model was developed by Ishihara and Tobler, where Ishihara introduced fundamental equations of motion for limited torque converter

operation [26], and Tobler expanded said equations to include all normal torque converter operating conditions [27]. Ishihara, who initiated the development of dynamic torque converter models, simulated the frequency response function using the derived equations of motion [26]. Physics based torque converter models have been assumed to be accurate, and used to solve a variety of engineering problems, including TCC slip controls and hybrid vehicle controls [28-32]. Pohl, using Tobler's equations, simulated FRFs of the torque converter in a vehicle drivetrain [33]. Steady state performance of the model correlated well with steady state performance in vehicle, but no experimental FRF data was acquired. Experimental FRFs of torque converters were acquired on a transmission test setup, but the test results were dominated by a low frequency mode of the test rig [34]. It was recommended that a dedicated torque converter test setup be deployed to characterize the open TC. Chapter 5 describes experimental TTFRFs of torque converters in a special test setup, and compares the test data to results obtained using Tobler's equations.

1.3.4 Centrifugal Pendulum Vibration Absorber

CPAs were first introduced in 1937 by Sarazin [35]. The fundamental benefit of CPAs is their tuning to order rather than frequency, and the automotive sector began utilizing them in the early 2000s [36]. A CPA in a torque converter lockup clutch damper and in a dual mass fly wheel have been shown to reduce torsional vibrations effectively [2, 36]. Research on CPAs encompasses pendulum path design, understanding instabilities and nonlinearities [37], and limited in situ experimental characterization.

For larger angular displacement in circular path CPAs, tuning frequency decreases. This is a fundamental nonlinearity in circular path pendulums. To address this, Madden patented a cycloidal path CPA in 1980 [38], and Denman developed path equations for a tautochronic CPA so that CPA tuning remained constant for all excitation amplitudes. Tautochronic CPA paths are subject to research [39, 40], and include cycloids and epicycloids [41]. In addition to the path of the pendulum, pendulum suspension has also been investigated. Several pendulum types are covered in [42], of which parallel and trapezoidal bifilar pendulums are commonly used in automotive applications.

The literature does not contain much record of experimental FRFs of CPAs. A unique test setup to measure CPA FRFs (absorber angle / torque input) was developed [43], and a ring down test to characterize friction and damping of the CPA also carried out in [44]. This experimental work was not carried out on automotive CPA hardware. This test setup does have capability to spin at constant speed, while superimposing a torsional excitation to the rotor. Another experimental work characterized friction in a production CPA with the rotor fixed, while an individual pendulum was disturbed [45]. A torque converter test setup was deployed by Song to measure the TTFRF of a CPA in a TCC damper [46]. While similar conceptually to the experiments in this dissertation, data was not acquired at several operating speeds, test results were not correlated with a model of the hardware, and physical parameters not estimated from the data. Chapter 5 presents an experimental characterization of equivalent viscous damping of a CPA, submerged in ATF, in a TCC

damper, at several operating speeds. Customized torque converter hardware made it possible to accurately characterize CPA damping.

1.4 Research Objectives

Improved drivetrain vibration attenuation in the face of increasing engine vibration amplitudes at lower frequencies motivates this research. Improving the accuracy of dynamic drivetrain component models and introducing a novel vibration absorber contribute to improved vibration isolation in future ICE drivetrains. Accurate component models can predict the vibration isolation performance and drivetrain dynamics, and save on development costs. The lessons learned from characterizing and modeling existing hardware will feed into improving predictions of future hardware. Not only is the accuracy of dynamic models of the individual components important to understand, but also how the respective model parameters (friction, damping, stiffness, & inertia) influence full drivetrain NVH (noise vibration and harshness). In the simulated TTFRFs of a torque converter in a full drivetrain, torque converter model parameters heavily influence other drivetrain modes (Figure 1.3). Parameter set 1 has less friction in the damper mechanism than parameter set 2.

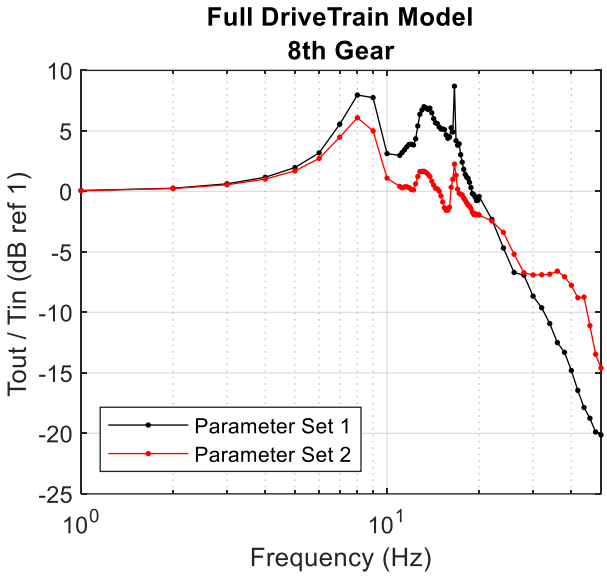

Figure 1.3. TTFRF of locked torque converter in a full driveline model. The two different parameter sets yield different results, demonstrating the importance of accurately models of the torque converter.

In Chapter 2, the design and test of two pTVA configurations proves the utility of a planetary gear set in targeting low frequency torsional modes of vibration. The planetary gear set allows for packaging space savings by taking advantage of reflected inertia across a fixed gear ratio. Compared to a traditional TVA of equivalent performance, the pTVA used up to 3 times less volume. An alternate configuration of the pTVA was

recommended, allowing for a stiffer spring element while still taking advantage of reflected inertia properties.

Chapter 3 discusses a more complete set of TTFRF data on TCC dampers than previously acquired, and estimation of physical model parameters. TTFRFs were measured at several operating speeds to characterize speed dependent friction effects. Beyond providing experimental characterization of speed dependencies, an additional source for damping during locked clutch operation was hypothesized. TTFRF data discussed in Chapter 4 was instrumental in friction characterization, and demonstrating the need for additional damping.

The TTFRFs of several torque converters were measured at several operating speed ratios, and lumped parameter TC models simulated (Chapter 4). This data provides experimental validation of a physics based, hydrodynamic torque converter model, and highlights deficiencies in said model. It was hypothesized that at low speed ratios, when toroidal flow is high, the working fluid flow reflects additional inertia to the mechanical TC elements (further investigation needed). This research also points out a resonance unique to turbine damper TC architectures, and demonstrates that K-factor influences the cutoff frequency of the TTFRF.

TTFRF measurements on a series of custom TCs contributed to characterizing the equivalent viscous damping of a CPA, submerged in ATF, in a TCC damper (Chapter 5). The TCC damper had two spring stages in series (arc springs and straight springs), and a CPA. The custom hardware included an unmodified TC, pinned CPA, pinned damper springs, and pinned straight spring. The pinned damper tests characterized the viscous damping of the CPA, without the effects of damper friction present in the system.

2 Design and Test of a Torsional Vibration Absorber in Series with a Planetary Gear Set

Luke Jurmu[a], Darrell Robinette[a] Jason Blough[a], Mark Gehringer[b]

[a]Department of Mechanical Engineering
Michigan Technological University
1400 Townsend Dr, Houghton, MI 49931, USA
lukejurmu@hotmail.com
dlrobine@mtu.edu
jrblough@mtu.edu

[b]General Motors Company
P.O. BOX 33170
Detroit, MI 48232-5170, USA
mark.a.gehringer@gm.com

Corresponding author: Luke Jurmu

Keywords: planetary; torsional; vibration; absorber; drivetrain vibrations; passive vibration control

2.1 Background

This chapter is the original submission of a journal article published in the Journal of Vibration and Control [11]. The idea for the pTVA originated with Darrell Robinette and Mark Gehringer, and takes advantage of reflected inertia across a fixed gear ratio. The pTVA lends itself very useful in tuning to very low frequency modes of vibration (below 30 Hz), and while engine operation rarely excites low frequency torsion modes, other drivetrain inputs—tip-in tip-out, shift events, clutch apply, road inputs—can excite these low frequency torsion modes. The pTVA attenuates the system response about its tuning frequency, and could find applications in rear wheel drive drivetrain architectures.

2.2 Abstract

Traditional vibration absorbers have not often been a practical solution for attenuating low frequency drivetrain modes of vibration due to combination of the large mass and inertia and/or low stiffness, required to tune to the desired frequency. With the goal of reducing the inertia and size of a torsional vibration absorber, a unique vibration absorber was developed. Using a planetary gear set, the effective inertia of the absorber was increased without changing its physical mass, and a torsional mode below 30 Hz was successfully attenuated with physically realizable inertia and stiffness parameters. By reducing the tuned mass, the total volume claimed by the vibration absorber and planetary gear set was up to 3 times less than an equivalent traditional vibration absorber. A lumped parameter torsional model was developed to determine the optimal

configuration of the planetary gearset input, output and absorber inertia as well as a method to predict the optimal tuning frequency of the planetary torsional vibration absorber. A drivetrain dynamometer setup which emulates a two degree of freedom torsional system was utilized to experimentally test and validate the performance of two planetary torsional vibration absorber prototypes built based upon the results of the lumped parameter model. The dynamometer setup was designed to have a first torsional mode around 20 Hz which the planetary torsional vibration absorber was designed to attenuate. Based upon the experimental results of the planetary torsional vibration absorber, a reduction of over 20 dB was achieved.

2.3 Introduction

Internal combustion engine fuel saving strategies like engine cylinder deactivation, engine downsizing, and low-speed torque converter clutch lockup increase the amplitude of dynamic torque imposed upon drivetrain of the vehicle. These increased torsional amplitudes propagate to downstream drivetrain components and drivetrain mounting points, increasing the amplitude of drivetrain and vehicle body structure responses. As the torsional vibration amplitudes increase, more vibration attenuation is required to maintain acceptable levels of noise and vibration. In vehicle drivetrains, there are several spring elements (shafts, damper springs, tires) in series that contribute to drivetrain vibration phenomena. These drivetrain elements are subject to torsional vibrations from the engine, and each of these elements has a natural frequency, some of which lie in the engine's operating range. There are several low frequency modes of vibration typically found in vehicle drivetrains [47], which are difficult to attenuate given mass and packaging constraints; these modes are generally avoided by changing powertrain operating state (Figure 2.1).

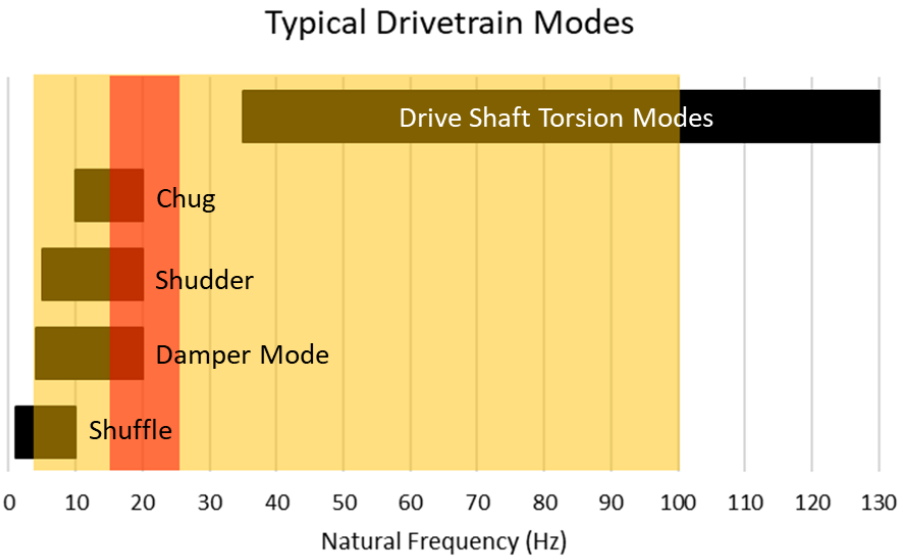

Figure 2.1. Drivetrain mode map. Red region (15-25 Hz) indicates the frequency range targeted when designing the pTVA. Yellow region (5-100 Hz) indicates potential application range for a pTVA in general.

Passive vibration control devices commonly used in vehicle drivetrains include torque converters, dual-mass flywheels (DMF), centrifugal pendulum absorbers (CPA), and torsional vibration absorbers (TVA) [2, 5]. DMF and torque converters coupled with CPAs have been shown to be highly effective isolating the drivetrain at frequencies higher than their own respective damper mode, and when the CPA [35, 43, 48, 49] is adequately tuned to the internal combustion engine's firing orders. These devices are not as effective at mitigating frequencies at or below their own natural frequency. Thus, low frequency torsional vibrations are transmitted to the vehicle drivetrain, exciting low frequency drivetrain modes. The TVA is useful where there is a specific mode of vibration that is difficult to attenuate with other methods. TVAs have been widely studied [4, 50], and much work has been done with unique vibration absorber configurations [51-56].

A limitation of the TVA, for drivetrain applications, is that inertia and mass are added to the system. For TVAs tuned to high frequency vibrations, the amount of added mass is negligible, but for low frequencies, the additional mass is substantial. Mechanical advantage can be used to increase the effective inertia of the TVA, thus reducing the added mass. Increasing of the effective inertia can be achieved via a simple gear ratio, or with an inerter. The inerter is a two-terminal device where the force applied is proportional to the relative acceleration across its terminals [8]. One benefit of using the inerter in a tuned mass damper (TMD), is a reduction its mass. Several configurations of TMDs that incorporate an inerter have been investigated [7, 8, 57-60]. Typically, the inerter is realized as a ball screw device that spins a flywheel. The two terminals of the

inerter move in the linear domain, but the same device can be realized in the torsional domain with a planetary gear set [9].

The patented vibration absorber described in this paper, a planetary torsional vibration absorber (pTVA), is not configured with the gear set behaving as an inerter [10]. Rather, the planetary gear set is configured as a fixed gear ratio, and achieves an increased effective inertia through mechanical advantage. Increasing the effective inertia of the device is the kernel of the pTVA concept, and it demonstrates that low frequency drivetrain modes of vibration can be targeted with less added mass to the drivetrain. For this investigation, the pTVA will target a torsional mode occurring somewhere in the 15-25 Hz range, typical of drivetrain system responses. This frequency range was targeted due to difficulty, from a mass and space claim perspective, in packaging a traditional TVA for light duty automotive applications. The mode map in Figure 2.1 also illustrates other potential applications of a pTVA, where the pTVA could be used to attenuate a prop shaft or damper mode for example.

2.4 pTVA Development

2.4.1 pTVA Design

To experimentally verify the performance of the pTVA concept, a 2DOF resonant system is designed with a low frequency torsional mode of vibration. Then, a pTVA is designed to attenuate this torsional mode of vibration. A drivetrain dynamometer setup was selected as a good candidate for both the analytical and physical realization of a 2DOF system. The dynamometer setup also featured the necessary safety and fixture hardware for the pTVA in addition to driving and absorbing electric motors that represented the degrees of freedom of the system. This setup was modeled as a semidefinite 2DOF system and the system stiffness, a shaft coupling the two motors, was designed to achieve a 15-25 Hz mode of vibration (Figure 2.2). Once the 2DOF system was parameterized from the physical dynamometer setup, the design and integration of a pTVA to cancel the 1st torsion mode was undertaken. The pTVA model was developed using a simple planetary gear set, including only tooth counts and lumped inertia onto the sun, carrier and ring gears. A lumped spring-damper was used to represent the elastomer coupling the gear set to the absorber inertia. The stiffness and damping of this element was used to predict an optimal range of properties to target when building the prototype.

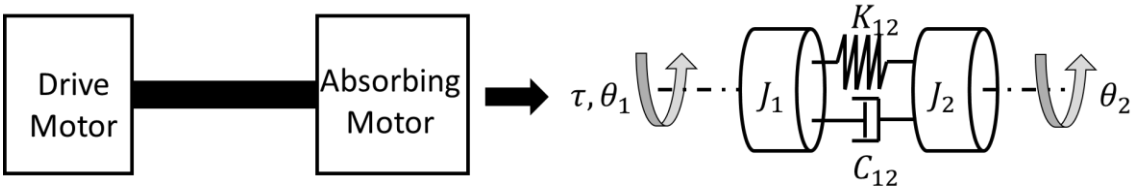

Figure 2.2. Sketch of drivetrain dynamometer test set up (left), and the corresponding semidefinite 2DOF model (right).

To start off the process, the design of the shaft coupling the two electric motors was required to get a torsional mode in the range of 15-25 Hz. The inertia of the drive and absorbing motors and associated shafting were known along with the required length of the shaft to connect the dynamometers through a test fixture housing. To determine the required torsional stiffness and diameter dimensions, the natural frequency equation of the semidefinite 2DOF system is rearranged to solve for torsional stiffness, and related to the torsional stiffness of a circular shaft section (Eq. 1).

$$K_{shaft} = \frac{\pi G}{32L}(OD^4 - ID^4) = \frac{w_n^2 J_1 J_2}{J_1 + J_2} \qquad (1)$$

The inertias in (Eq. 1) are the drive motor (J_1) and the absorbing motor (J_2)—summarized in Table 2.1. A coupling shaft stiffness of 1195 N m/rad or 20.86 N m/deg is required when targeting a 20 Hz torsional natural frequency. A shaft of 0.457 m (18 in) in length with a minimum outer diameter of 0.0138 m (0.545 in) was fabricated and installed on the dynamometer setup. A series of torsional test from 0-50 Hz was performed and found that the fabricated shaft to have an equivalent stiffness of 1295.7 Nm/rad and an equivalent damping of 0.18 Nm-s/rad at a torsional natural frequency of approximately 22 Hz for the 2DOF dynamometer setup. The test procedure and data processing to obtain these results will be detailed later in the paper.

Table 2.1: Physical parameter values used in the 2DOF system design (Figure 2.2), and experimental parameter estimates of the same system.

	Variable	Design Parameter	Experimental Estimate
Shaft Stiffness (Nm/rad)	K_{12}	1195	1295.7
Input Dyno Inertia (kg m2)	J_1	0.067	0.07
Output Dyno Inertia (kg m2)	J_1	1.34	1.37
Shaft Damping (Nm s/rad)	C_{12}	-	0.18

The major design criteria for the pTVA to is to integrate with the fabricated coupling shaft mentioned previously and appreciably attenuate the 22 Hz torsional natural frequency of 2DOF dynamometer setup. The starting point of the pTVA prototype design was the simple planetary gear set, consisting of a sun, ring and planet gears as well as a planet carrier assembly that supports the planet gears. For this investigation a simple planetary gear set from the hybrid election drive unit (transmission) of a second generation Chevrolet Volt was used due to its availability and compatibility with adding TVA hardware. Figure 2.3 shows the disassembled planetary gear set without any added

TVA hardware. The selection of this planetary gear set was based solely on convenience to demonstrate the pTVA concept, and not on optimizing a planetary gear set for a production pTVA design. It should be noted that the torque carrying capacity of the planetary gear set in Figure 3 far exceeds the design limits necessary for a pTVA. An optimized gear set for a pTVA would be much reduced in size, namely face width (axial length).

Figure 2.3. Disassembled planetary gear set from second generation Chevrolet Volt drive unit with 81 tooth ring gear (R) and 39 tooth sun gear (S).

For a simple planetary gear set there were six possible fixed gear states. For the purpose of increasing the perceived inertia of the pTVA at the shaft, a gear ratio less than 1 was desired. After investigating the possible gear states for ease of fabrication and for gear ratios less than one, two configurations were determined to be suitable candidates. Both configurations had the carrier and planets fixed to the rotating system of the dynamometer setup, and switched between a grounded ring gear or grounded sun gear. The two configurations were called ring pTVA and sun pTVA, depending on which gear the absorber mass was clamped to. The ring pTVA configuration had a gear ratio of 0.675, and the sun pTVA had a gear ratio of 0.325, see Eq. 2 & 3, where R and S represented the number of teeth in the ring and sun gears respectively. For both gear states, the carrier was the input, attached to the coupling shaft of the dynamometer setup, and the ring or sun gear was the output, depending on the gear state, attaching the absorber inertia.

$$G_{ring} = \frac{R}{S+R} \qquad (2)$$

$$G_{sun} = \frac{S}{S+R} \qquad (3)$$

The drivetrain dynamometer test fixture was modified to add a grounding beam that would allow either the ring or sun gear of the pTVA gears to be grounded. For the vibration absorber portion of the design, a steel shaft collar large enough to clamp elastomer rubber around the outer diameter of either the sun or ring gear assemblies was selected as the absorber inertia. A natural rubber (30A durometer) elastomer was selected to act as the absorber spring element, knowing a relatively soft element would be required. This was the lowest durometer rubber found at the desired thickness and width. Since the rubber properties were unknown, an experimental approach would be required to tune the equivalent stiffness and achieve desired attenuation of the 22 Hz torsional natural frequency. The prototypes of the completed pTVA designs, ring pTVA and sun pTVA**Error! Reference source not found.**, are shown in Figure 2.4.

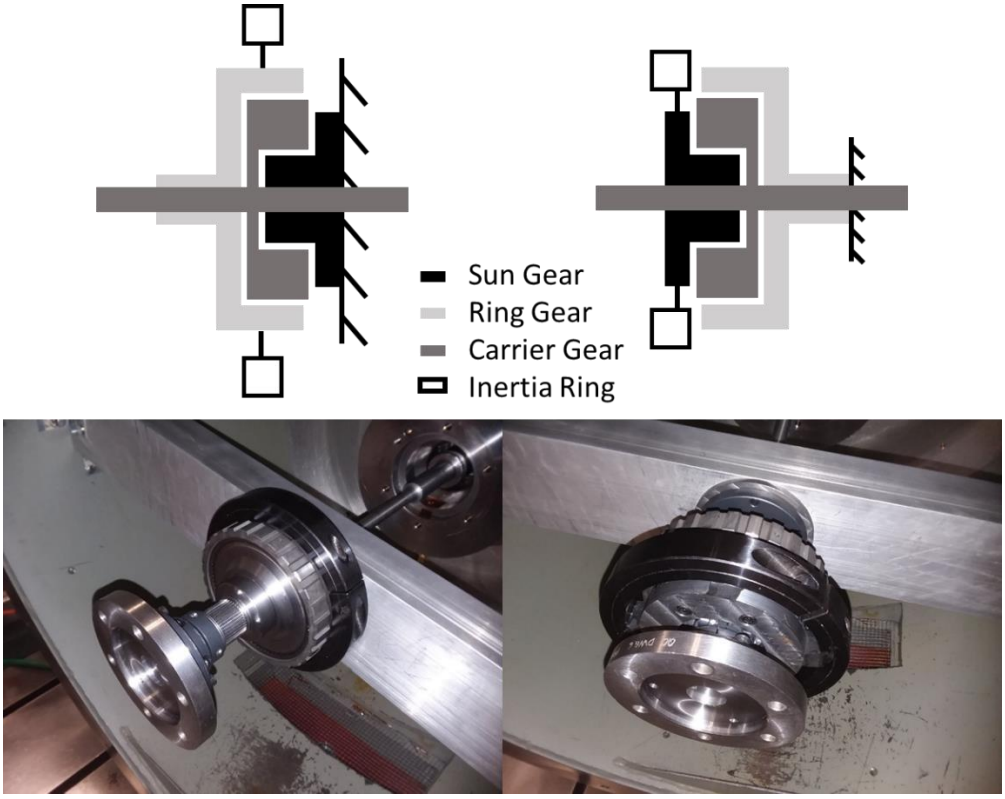

Figure 2.4. Sketches of the ring pTVA and the sun pTVA (top).Completed fabrication of ring pTVA (bottom left), and sun pTVA (bottom right). The absorber inertia in each configuration is the black shaft collar, which clamps around the rubber and the free spinning gear. The grounded gear bolts to a beam which runs across the diameter of the fixture.

2.4.2 pTVA Model

After the pTVA was designed and prototyped, a model of the pTVA was developed to predict optimum absorber tuning (Figure 2.5**Error! Reference source not found.**). The pTVA was physically attached to the drive motor (J_1) side of the custom shaft because that was where the larger amplitude vibrations were expected. The inertia of the carrier and planets were lumped into the input inertia, and the output gear—ring or sun depending on the configuration—modeled as J_3. The steel shaft collar was modeled as J_4 with the spring/damper of the rubber, K_{34} and C_{34}, clamped between J_3 and J_4.

Table 2.2: pTVA model parameters.

	Variable	Sun pTVA	Ring pTVA
Sun gear inertia (kg m2)	J_3	0.002073	
Ring gear inertia (kg m2)	J_3	0.004735	
Carrier and planet inertia (kg m2)	~	0.003191	
TVA inertia (kg m2)	J_4	0.008476	
Grounded element	~	Ring	Sun
Gear ratio	G	0.325	0.675
Shaft Damping (Nm s/rad)	C_{12}	0.480	1.58
pTVA Stiffness (Nm/rad)	K_{34}	47.39	99
pTVA damping (Nm s/rad)	C_{34}	0.2	0.3

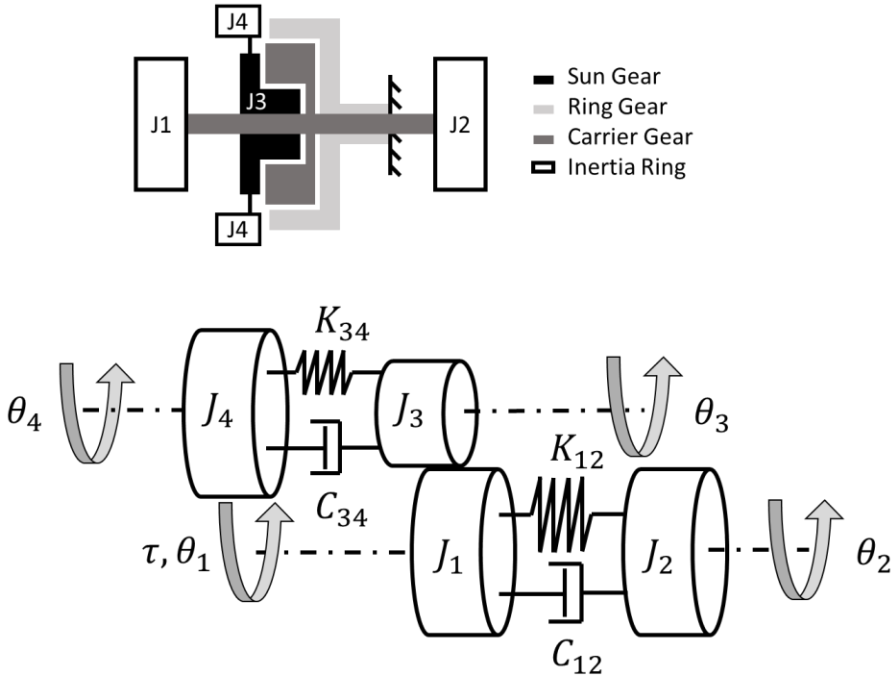

Figure 2.5. Sketch of drivetrain dynamometer test set up with the sun pTVA prototype installed (top). The corresponding pTVA model schematic (bottom). Note: carrier gear inertia is lumped into J1.

The equations of motion (EOM) were derived for the pTVA model in Eq. (4-8). The pTVA model parameter values are listed in Table 2.2**Error! Reference source not found.**:

$$\left(J_1 + \frac{J_3}{G^2}\right)\ddot{\theta}_1 + C_{12}\left(\dot{\theta}_1 - \dot{\theta}_2\right) + K_{12}(\theta_1 - \theta_2) + \frac{K_{34}}{G}(\theta_3 - \theta_4) + \frac{C_{34}}{G}\left(\dot{\theta}_3 - \dot{\theta}_4\right) = \tau \tag{4}$$

$$J_2\ddot{\theta}_2 - C_{12}\left(\dot{\theta}_1 - \dot{\theta}_2\right) - K_{12}(\theta_1 - \theta_2) = 0 \tag{5}$$

$$\left(J_3 + J_1G^2\right)\ddot{\theta}_3 + C_{34}\left(\dot{\theta}_3 - \dot{\theta}_4\right) + K_{34}(\theta_3 - \theta_4) + GC_{12}\left(\dot{\theta}_1 - \dot{\theta}_2\right) + GK_{12}(\theta_1 - \theta_2) = G\tau \tag{6}$$

$$J_4\ddot{\theta}_4 - C_{34}\left(\dot{\theta}_3 - \dot{\theta}_4\right) - K_{34}(\theta_3 - \theta_4) = 0 \tag{7}$$

$$G = \frac{\theta_1}{\theta_3} = \frac{\tau_3}{\tau_4} \tag{8}$$

This system of equations was used to simulate the torque transmissibility of the pTVA. Two iterations of testing were executed to tune model parameters, and have greater confidence in predicting optimal tuning. First, the torque transmissibility of the steel shaft was measured to verify that the natural frequency of the 2DOF system was in the desired range, and to tune the shaft stiffness in the pTVA model. Second, the planetary gear set was added to the system (no vibration absorber), and torque transmissibility measured, so that the added inertia to the system could be accurately modeled. With the pTVA model tuned with test data, the optimum natural frequency of the shaft collar and rubber was estimated.

2.5 Experimental Methods

2.5.1 Torque Transmissibility Measurement

The vibration isolation performance of the pTVA was quantified by the ratio of the dynamic torque measured downstream of the pTVA versus dynamic torque measured upstream of the pTVA; this was called the torque transmissibility. This metric of vibration isolation was used to evaluate the effectiveness of the pTVA.

The pTVA device was designed for installation in the drivetrain dynamometer. When measuring the torque transmissibility of the device, the input motor, input to the pTVA system, was commanded a mean and dynamic torque, and the absorbing motor commanded a mean speed. This loading case eliminated any lash effects in the system while at the same time constraining the system from accelerating uncontrollably. This loading case—input torque, output speed—also represented the boundary conditions in a vehicle's drivetrain; the engine outputs a torque as the input to the drivetrain, and the vehicle's speed controls the speed of the drive train output (wheels). The drivetrain

dynamometer (Figure 2.6) was used to measure the torque transmissibility of the pTVA, using a sine dwell method. The frequency of the dynamic torque was varied from 0-50 Hz (1 Hz resolution), while the amplitudes of the mean and dynamic components were held constant.

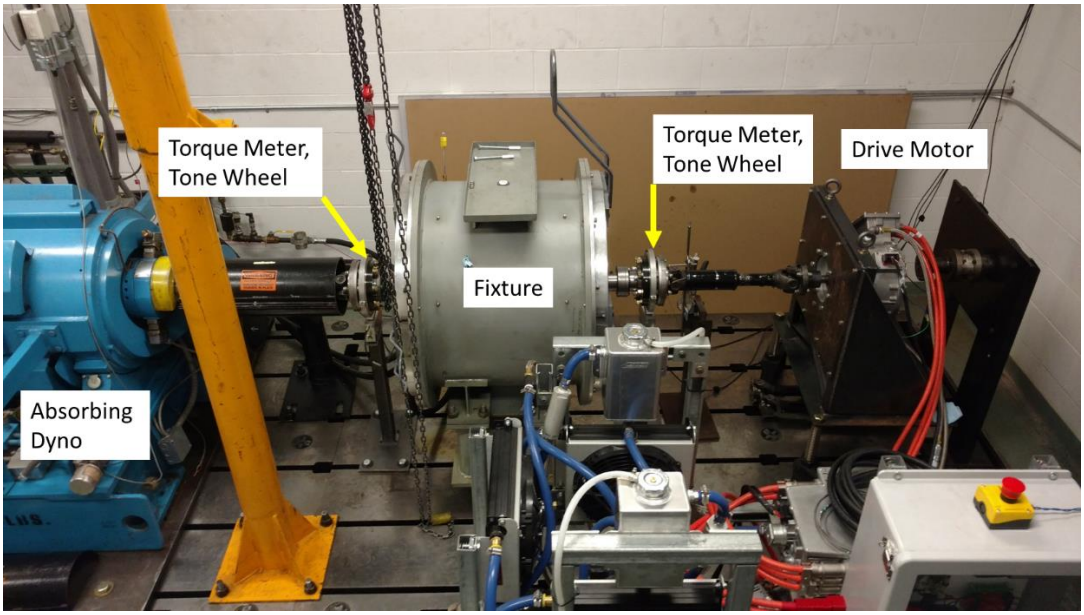

Figure 2.6. Test setup used for measuring torque transmissibility.

Inline torque meters (pn: 5308C-01A) were used to acquire time domain torque measurements on both sides of the pTVA. From the acquired time domain signals, autopower spectra were computed, which in turn were used to calculate the value of the torque transmissibility (Figure 2.7). For each frequency of excitation, time domain signals were post processed into a torque transmissibility value.

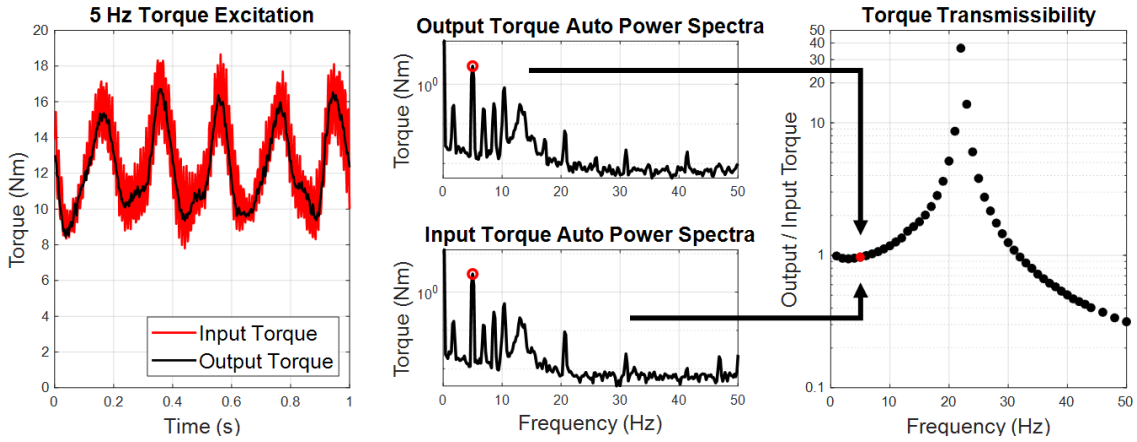

Figure 2.7.Time domain signals are converted to the frequency domain via FFT, and then the torque transmissibility is computed.

2.5.2 pTVA Tuning

Natural rubber was selected as the spring/damping material of the pTVA. Since the properties of the rubber were not known, an experimental tuning approach was used rather than trying to predict the proper amount of rubber using assumed material properties. To experimentally tune the pTVA, the gear was clamped in a vice, and the rubber and inertia clamped to the gear. A tri-axial accelerometer was used to measure the acceleration at the inertia ring in response to a pluck excitation. The pluck was applied tangentially to the ring (Figure 2.8)

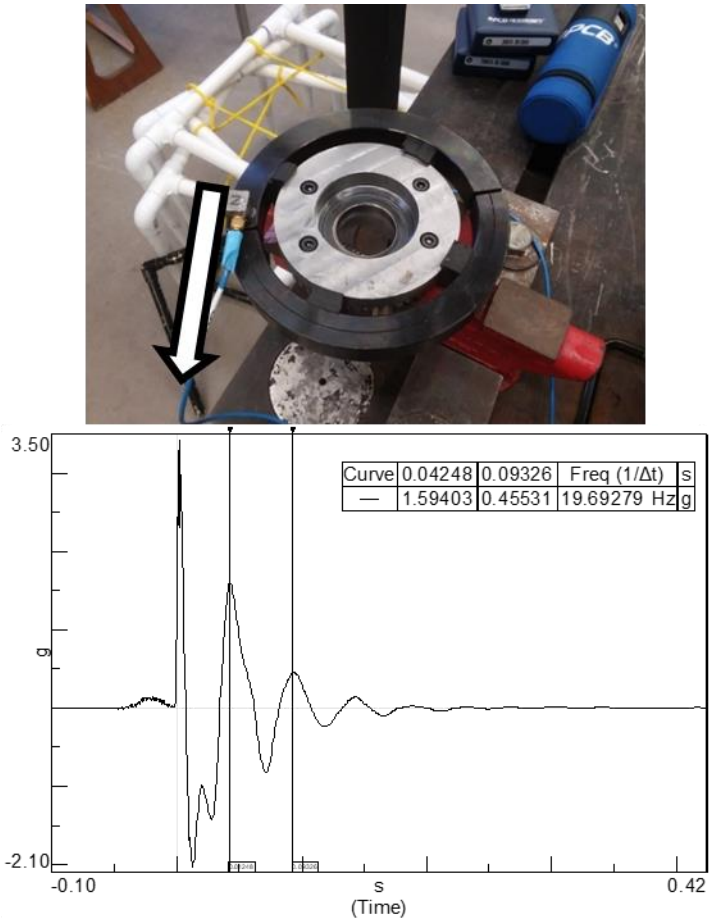

Figure 2.8. Test setup to measure the natural frequency of the rubber, inertia ring, system (top). Response of the inertia ring to a pluck excitation (bottom). This measurement is used to calculate the natural frequency of the rubber-inertia ring system.

From the measured acceleration time history, the natural frequency of the TVA configuration was calculated from the natural period of oscillation. The pluck test was used to tune the natural frequency to the desired frequency—determined from the pTVA model.

2.6 Experimental and Analytical Results

Prior to testing the pTVA, the shaft design was validated by measuring the torque transmissibility of the motor-shaft-dyno system. The 2DOF unconstrained system model was then calibrated to match the experimental results. Next, the planetary gear set was installed into the motor-shaft-dyno system, and the torque transmissibility measured again. This was useful to quantify the added inertia and damping of the planetary gear set. The pTVA model was then used to estimate the optimal natural frequency of the rubber-shaft collar system. Finally, the torque transmissibility of the completed pTVA prototypes was measured.

The 2DOF system was designed to have a natural frequency of 21.78 Hz, but when tested, the natural frequency was between 22 and 23 Hz (Figure 2.9). This difference was acceptable because, the shear modulus of the steel shaft was assumed to be 80 GPa, which likely isn't the case, and the shaft mode was still in the desired frequency range (15-25 Hz). After updating motor and dyno inertias to include shafting and couplings, the shaft stiffness of the 2DOF model was updated to 1295.7 N m/rad or 22.6 N m/deg, to match the natural frequency of the experimental torque transmissibility. Also shown in Figure 2.9, is the torque transmissibility of the motor-shaft-dyno system with the planetary gear set installed. As expected, the shaft resonance shifted down in frequency due to the added inertia, and down in amplitude due to gear mesh damping. These calibrated stiffness, damping, and inertia values were in turn used in the pTVA models (refer back to Table 2.1).

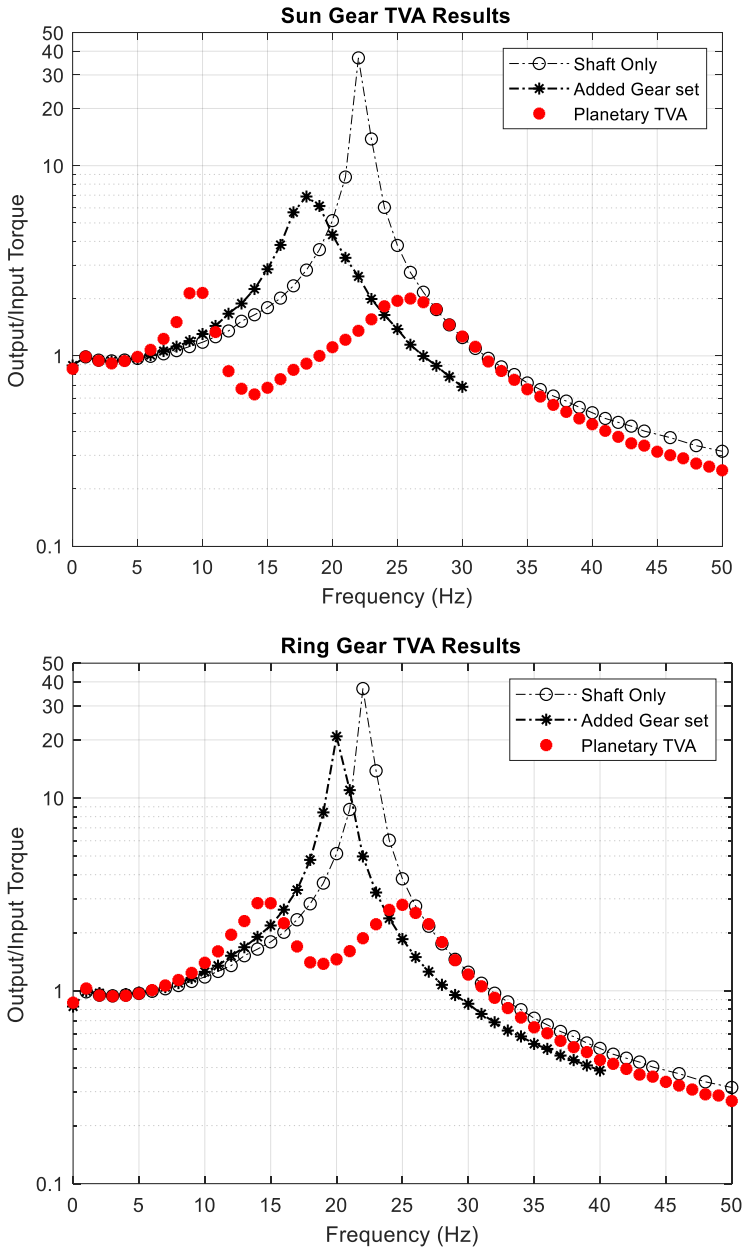

Figure 2.9. Top: Experimental torque transmissibility of the motor-shaft-dyno system by itself, with the added planetary gear set, and with the complete Ring pTVA.
Bottom: Experimental torque transmissibility of the motor-shaft-dyno system by itself, with the added planetary gear set, and with the complete Sun pTVA.

Then, the pTVA models were used to predict the optimal natural frequency of the rubber-shaft collar system. This was done by simulating the pTVA model at several natural frequency values until two similar amplitude peaks were observed in the torque transmissibility plot. (The damping of the rubber was estimated from mistuned pTVA torque transmissibility measurements.) The sun pTVA model predicted that optimal TVA

tuning was 11.9 Hz, and the Ring pTVA model predicted 17.2 Hz (Figure 2.10**Error! Reference source not found.**). With these natural frequency targets, the rubber-shaft collar system was experimentally tuned for each pTVA configuration with the pluck test method, and both configurations showed optimally tuned behavior when tested (Figure 2.9).

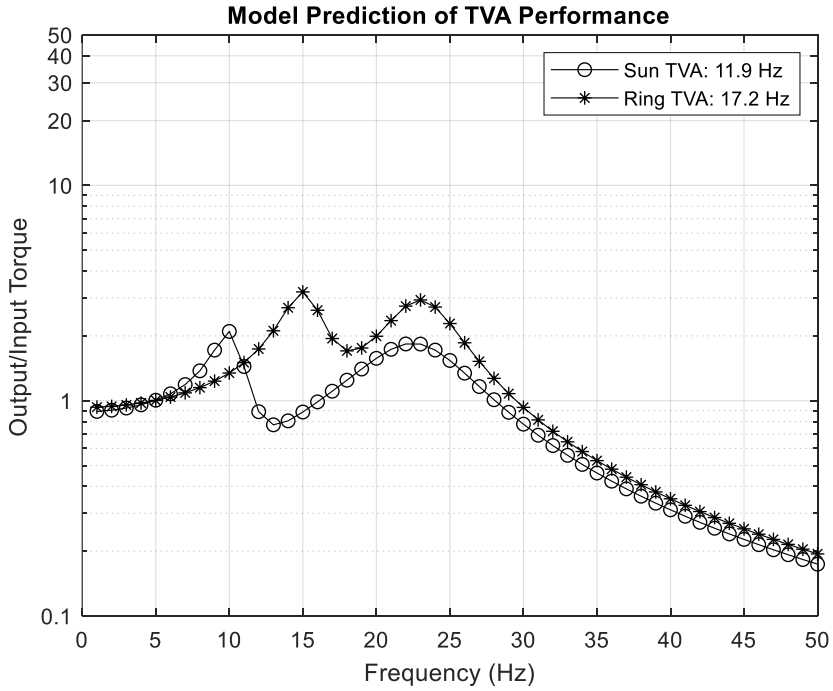

Figure 2.10. Sun and Ring pTVA model predictions. Optimal TVA tuning frequencies: 11.9 Hz (Sun pTVA) and 17.2 Hz (Ring pTVA).

In terms of the performance of the two pTVA configurations, the sun pTVA attenuated the shaft mode amplitude from 37 down to around 2 (25 dB reduction), and the ring pTVA brought the amplitude down to around 3 (22 dB reduction). It was expected that the sun pTVA would outperform the ring pTVA because the gear ratio of the sun pTVA configuration was lower than that of the ring pTVA. A lower gear ratio makes the reflected inertia of the sun pTVA larger, and thus able to absorb more vibration energy.

2.7 Discussion

To assess whether or not the pTVA reduced the inertia and size of the absorber, a traditional TVA model is created (see Appendix), and its parameters tuned to match the pTVA performance. The stiffness, inertia, and mass of the absorber component of the pTVA are compared to the traditional TVA's stiffness, inertia and mass parameters (Table 2.3). To visualize the differences, CAD models are built to compare the physical size of the traditional TVA with the pTVA (Figure 2.11 & Figure 2.12).

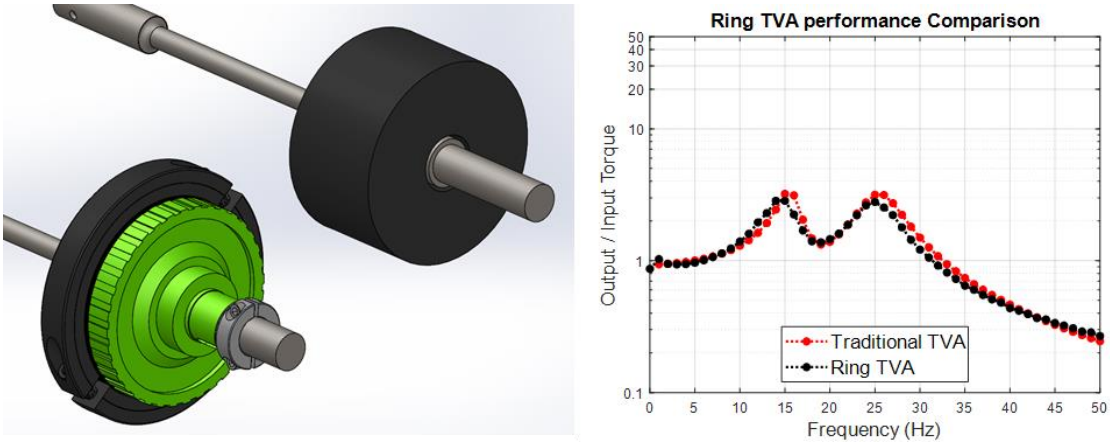

Figure 2.11. Comparing a traditional TVA of similar torque transmissibility to the Ring pTVA.

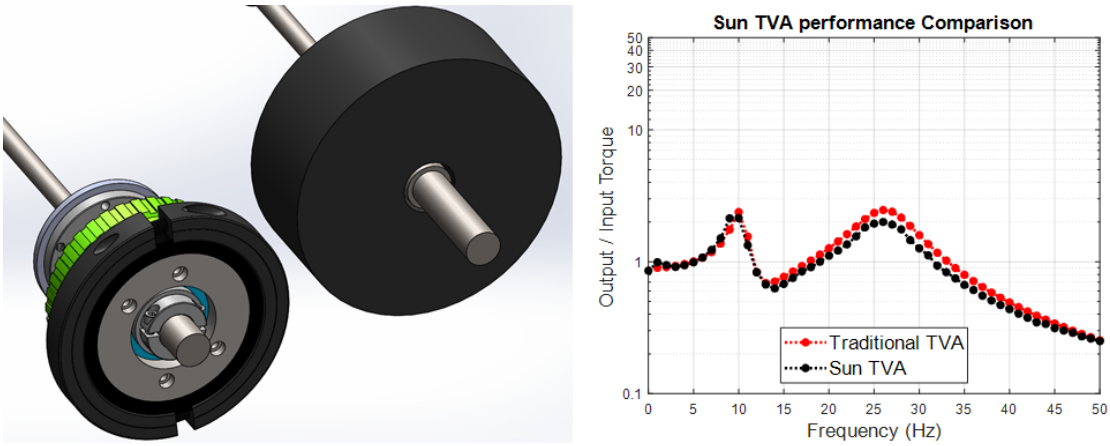

Figure 2.12. Comparing a traditional TVA of similar torque transmissibility to the sun pTVA.

In both pTVA configurations, the size of the absorber mass is much larger in the traditional TVA as opposed to the pTVA. From a mass perspective, the sun pTVA reduces the additional mass by a factor of 10.4 (Table 2.3), and the ring pTVA reduces the absorber mass by a factor of 4.8. When the overall packaging is compared, the traditional TVA doesn't have as much of a difference when compared to the pTVA. Although there doesn't appear to but much for packaging gains with the pTVA prototype, it is important to note that the planetary gear set is not optimized for this application. The planetary gear set is out of the Chevy Volt drive unit, and is designed for the high torque loading of the drive unit. For a vibration absorber application, a smaller planetary gearset can be used, and the packaging benefits would be more apparent.

Table 2.3: Equivalent TVA parameters used to match sun and ring pTVA torque transmissibility.

Parameter	Equivalent TVA	Ring pTVA	Ratio (Equivalent /Ring)	Equivalent TVA	Sun pTVA	Ratio (Equivalent /Sun)
TVA inertia (kg m^2)	0.0186	0.00848	2.19	0.0802	0.00848	9.47
TVA stiffness (N m/rad)	238	99.0	2.40	456	47.4	9.63
TVA damping (N m s/rad)	0.7	0.3	2.33	2	0.2	10.0
TVA mass (kg)	7.78	1.62	4.80	16.9	1.62	10.4
Device Volume (m^3)	0.000972	0.000725	1.34	0.002106	0.000725	2.91

Another interesting aspect of comparing the traditional TVA to the pTVA is how other physical properties compare. To match the sun pTVA performance, the TVA inertia needs to be ~ 0.08 kg m^2. This is a factor of 9.47 greater than the absorber inertia of the sun pTVA. Likewise, the traditional TVA inertia needs to be 2.19 times greater than the ring pTVA inertia. In the same way, the stiffness and damping properties of the traditional TVA is greater by a similar factor than the pTVA properties. Sun pTVA stiffness is 9.63 times smaller than the traditional, and the sun pTVA damping is smaller by a factor of 10. All of the sun pTVA parameters are smaller than the traditional TVA by close to the same factor. Similarly, the ring pTVA properties are also smaller by a factor of ~2. This is no coincident. The idea behind the prototype was that the effective inertia upstream of the gear ratio would be multiplied by a factor of $1/G^2$. For the sun pTVA this factor is 9.467, and for the ring pTVA the factor is 2.195.

The equations of motion of the pTVA also support this parameter ratioing. Looking at Eq. (3), the motion of J_1, is influenced by the shaft stiffness and damping ($K_{12}$and C_{12}), as well as the TVA stiffness and damping ($K_{34}$and C_{34}) via the gear set. One can notice how the torques from $K_{34}$and C_{34} applied on J_1, are divided by the gear ratio (G).

$$\left(J_1 + \frac{J_3}{G^2}\right)\ddot{\theta}_1 + C_{12}\left(\dot{\theta}_1 - \dot{\theta}_2\right) + K_{12}(\theta_1 - \theta_2) + \frac{K_{34}}{G}(\theta_3 - \theta_4) + \frac{C_{34}}{G}\left(\dot{\theta}_3 - \dot{\theta}_4\right) = \tau$$

When, using Eq. (8), θ_3 is replaced by $\frac{\theta_1}{G}$, and the effect of the gear ratio on the TVA parameters manifests itself in Eq. (9):

$$\left(J_1 + \frac{J_3}{G^2}\right)\ddot{\theta}_1 + \left(C_{12} + \frac{C_{34}}{G^2}\right)\dot{\theta}_1 + \left(K_{12} + \frac{K_{34}}{G^2}\right)\theta_1 =$$

$$\tau + C_{12}\dot{\theta}_2 + K_{12}\theta_2 + \frac{C_{34}}{G}\dot{\theta}_4 + \frac{K_{34}}{G}\theta_4 \qquad (9)$$

All of the TVA parameters (J_3, C_{34}, K_{34}) are divided by the gear ratio squared as viewed at the input inertia (J_1). What this also means is that the natural frequency of the TVA component is not affected by the gear ratio as observed from J_1 (Eq. 10).

$$w_n = \sqrt{\frac{K_{34}/G^2}{J_4/G^2}} = \sqrt{\frac{K_{34}}{J_4}} \qquad (10)$$

Ideally, the gear ratio would only act on the inertia, and not the spring, but, in order to achieve this, the spring component would have to be located between the carrier gear and the input inertia. There would be some packaging challenges to achieve this, hence this configuration wasn't pursued in this work.

Finally, what is the optimal tuning equation for the pTVA? The fixed point theory for vibration absorbers discussed in [3, 61], predict that the optimal frequency ratio of a TVA is:

$$F_{opt} = \frac{f_{tva}}{f_{mode}} = \frac{1}{1+\mu} \qquad (11)$$

Where μ is the mass ratio or rather the inertia ratio of the absorber inertia over the inertia subject to the TVA. Because of the gear ratio, μ can be updated with the gear ratio:

$$F_{opt} = \frac{f_{tva}}{f_{mode}} = \frac{1}{1 + \frac{J_{tva}/G^2}{J_1}} \qquad (12)$$

This equation would predict that the optimal frequency ratio of the TVA to be 0.790 for the ring pTVA and 0.466 for the sun pTVA. From the experimental tuning, the actual frequency ratios are 0.546 (sun pTVA) and 0.790 (ring pTVA). While not exact, the equation predicts the optimal frequency ratio of the pTVA quite well.

To improve the performance of the pTVA prototype, it would be necessary to minimize the inertia of the planetary gear set. However, more gains could most likely be achieved

by mounting the planetary gear set downstream of the TVA spring damper. Doing so would harvest the benefits of increasing the effective inertia and avoid the drawback of increasing the effective stiffness. This would also mean that the natural frequency of the TVA component of the pTVA would be affected by the gear ratio by a factor of G, yielding an effective natural frequency, ω_{eff} (Eq. 13).

$$\omega_{eff} = \sqrt{\frac{K_{tva}}{J_{tva}/G^2}} = \sqrt{\frac{K_{tva}G^2}{J_{tva}}} = G\omega_{tva} \qquad (13)$$

The pTVA would have applications in any rotating machinery where room for added mass and volume are limited, especially when targeting low frequency modes of vibration. It could be used as in the prototype—mounted directly to a shaft at the node of interest—or even packaged into a torque converter or a differential.

2.8 Conclusions

After designing a 2DOF system with a ~20 Hz torsional mode, the pTVA concept was designed, fabricated, and tested. The pTVA device was tuned experimentally using a pluck test method after predicting the optimal tuning frequency with a pTVA model. The pTVA model successfully predicted the optimal tuning frequency, and the pTVA decreased the torque transmissibility by 25 dB for the sun pTVA and 22 dB for the ring pTVA. It was shown that while the pTVA concept greatly reduced the mass of the absorber, the overall package size wasn't greatly reduced. This is due to the planetary gear set not being optimized for the pTVA application, and a leaner gear set could be designed for the pTVA application. A pTVA with an optimized planetary gearset has potential use in automotive drivetrains where space and mass are constraints are tight.

A different configuration of the pTVA could be implemented that would further reduce packaging space claim and inertia. By positioning the planetary gear set between the absorber inertia and the rubber stiffness, the effective inertia of the TVA would be larger without changing the effective spring stiffness or damping. Placing the rubber between the shaft and the carrier gear and the drive shaft would achieve this configuration. Then, the sun or ring gear would become the absorber inertia.

2.9 Appendix

2.9.1 Traditional TVA EOMs:

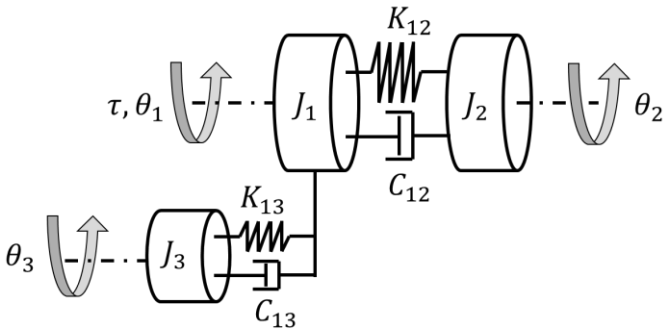

Figure A.1: Traditional TVA model.

EOM of the traditional TVA model:

$$J_1\ddot{\theta}_1 + C_{12}(\dot{\theta}_1 - \dot{\theta}_2) + C_{13}(\dot{\theta}_1 - \dot{\theta}_3) + K_{12}(\theta_1 - \theta_2) + K_{13}(\theta_1 - \theta_3) = \tau \quad \text{(A.1)}$$

$$J_2\ddot{\theta}_2 - C_{12}(\dot{\theta}_1 - \dot{\theta}_2) - K_{12}(\theta_1 - \theta_2) = 0 \quad \text{(A.2)}$$

$$J_3\ddot{\theta}_3 - C_{13}(\dot{\theta}_1 - \dot{\theta}_3) - K_{13}(\theta_1 - \theta_3) = 0 \quad \text{(A.3)}$$

The equations of motion are then converted to a state space representation of the system:

Choose 6 states, derive xdot in terms of x:

Table A.1: State Space formulation of traditional TVA

x_1	θ_1	$\dot{x_1}$	$\dot{\theta}_1$	x_4
x_2	θ_2	$\dot{x_2}$	$\dot{\theta}_2$	x_5
x_3	θ_3	$\dot{x_3}$	$\dot{\theta}_3$	x_6
x_4	$\dot{\theta}_1$	$\dot{x_4}$	$\ddot{\theta}_1$	$\frac{\tau}{J_1} - \frac{C_{12}}{J_1}(x_4 - x_5) - \frac{C_{13}}{J_1}(x_4 - x_6) - \frac{K_{12}}{J_1}(x_1 - x_2) - \frac{K_{13}}{J_1}(x_1 - x_3)$

x_5	$\dot{\theta}_2$	$\dot{x_5}$	$\ddot{\theta}_2$	$\frac{C_{12}}{J_2}(x_4 - x_5) + \frac{K_{12}}{J_2}(x_1 - x_2)$
x_6	$\dot{\theta}_3$	$\dot{x_6}$	$\ddot{\theta}_3$	$\frac{C_{13}}{J_3}(x_4 - x_6) + \frac{K_{13}}{J_3}(x_1 - x_3)$

State space matrices:

$\{\dot{x}\} = [A]\{x\} + [B]\{u\}$

$\{y\} = [C]\{x\} + [D]\{u\}$

Where:

$\{u\} = \tau$

$$A = \begin{bmatrix} 0 & 0 & 0 & 1 & 0 & 0 \\ 0 & 0 & 0 & 0 & 1 & 0 \\ 0 & 0 & 0 & 0 & 0 & 1 \\ \frac{-K_{12} - K_{13}}{J_1} & \frac{K_{12}}{J_1} & \frac{K_{13}}{J_1} & \frac{-C_{12} - C_{13}}{J_1} & \frac{C_{12}}{J_1} & \frac{C_{13}}{J_1} \\ \frac{K_{12}}{J_2} & \frac{-K_{12}}{J_2} & 0 & \frac{C_{12}}{J_2} & \frac{-C_{12}}{J_2} & 0 \\ \frac{K_{13}}{J_3} & 0 & \frac{-K_{13}}{J_3} & \frac{C_{13}}{J_3} & 0 & \frac{-C_{13}}{J_3} \end{bmatrix}$$

$$B = \begin{bmatrix} 0 \\ 0 \\ 0 \\ \frac{1}{J_1} \\ 0 \\ 0 \end{bmatrix} \qquad C = \begin{bmatrix} K_{12} & -K_{12} & 0 & C_{12} & -C_{12} & 0 \end{bmatrix} \qquad D = [0]$$

2.9.2 pTVA State Space Formulation:

From the EOMs, Eq. (11-15), eight states were chosen, and a state space formulation created:

Table A.2: pTVA State Space Formulation.

x_1	θ_1	$\dot{x_1}$	$\dot{\theta_1}$	x_5

x_2	θ_2	$\dot{x}_2$	$\dot{\theta}_2$	x_6
x_3	θ_3	$\dot{x}_3$	$\dot{\theta}_3$	x_7
x_4	θ_4	$\dot{x}_4$	$\dot{\theta}_4$	x_8
x_5	$\dot{\theta}_1$	$\dot{x}_5$	$\ddot{\theta}_1$	$\frac{\tau}{J_{1eq}} - \frac{C_{12}}{J_{1eq}}(x_5 - x_6) - \frac{K_{12}}{J_{1eq}}(x_1 - x_2) - \frac{C_{34}}{J_{1eq}G}(x_7 - x_8) - \frac{K_{34}}{J_{1eq}G}(x_3 - x_4)$
x_6	$\dot{\theta}_2$	$\dot{x}_6$	$\ddot{\theta}_2$	$\frac{C_{12}}{J_2}(x_5 - x_6) + \frac{K_{12}}{J_2}(x_1 - x_2)$
x_7	$\dot{\theta}_3$	$\dot{x}_7$	$\ddot{\theta}_3$	$\frac{G\tau}{J_{3eq}} - \frac{GC_{12}}{J_{3eq}}(x_5 - x_6) - \frac{GK_{12}}{J_{3eq}}(x_1 - x_2) - \frac{C_{34}}{J_{3eq}}(x_7 - x_8) - \frac{K_{34}}{J_{3eq}}(x_3 - x_4)$
x_8	$\dot{\theta}_4$	$\dot{x}_8$	$\ddot{\theta}_4$	$\frac{C_{34}}{J_4}(x_7 - x_8) + \frac{K_{34}}{J_4}(x_3 - x_4)$

State space formulation of pTVA:

$\{\dot{x}\} = [A]\{x\} + [B]\{u\}$

$\{y\} = [C]\{x\} + [D]\{u\}$

Where:

$\{u\} = \tau$

$$A = \begin{bmatrix} 0 & 0 & 0 & 0 & 1 & 0 & 0 & 0 \\ 0 & 0 & 0 & 0 & 0 & 1 & 0 & 0 \\ 0 & 0 & 0 & 0 & 0 & 0 & 1 & 0 \\ 0 & 0 & 0 & 0 & 0 & 0 & 0 & 1 \\ \frac{-K_{12}}{J_{1eq}} & \frac{K_{12}}{J_{1eq}} & \frac{-K_{34}}{GJ_{1eq}} & \frac{K_{34}}{GJ_{1eq}} & \frac{-C_{12}}{J_{1eq}} & \frac{C_{12}}{J_{1eq}} & \frac{-C_{34}}{GJ_{1eq}} & \frac{C_{34}}{GJ_{1eq}} \\ \frac{K_{12}}{J_2} & \frac{-K_{12}}{J_2} & 0 & 0 & \frac{C_{12}}{J_2} & \frac{-C_{12}}{J_2} & 0 & 0 \\ \frac{-K_{12}G}{J_{3eq}} & \frac{K_{12}G}{J_{3eq}} & \frac{-K_{34}}{J_{3eq}} & \frac{K_{34}}{J_{3eq}} & \frac{-C_{12}G}{J_{3eq}} & \frac{C_{12}G}{J_{3eq}} & \frac{-C_{34}}{J_{3eq}} & \frac{C_{34}}{J_{3eq}} \\ 0 & 0 & \frac{K_{34}}{J_4} & \frac{-K_{34}}{J_4} & 0 & 0 & \frac{C_{34}}{J_4} & \frac{-C_{34}}{J_4} \end{bmatrix}$$

$$B = \begin{bmatrix} 0 \\ 0 \\ 0 \\ 0 \\ \frac{1}{J_{1eq}} \\ 0 \\ \frac{G}{J_{3eq}} \\ 0 \end{bmatrix} \qquad C = \begin{bmatrix} K_{12} & -K_{12} & 0 & 0 & C_{12} & -C_{12} & 0 & 0 \end{bmatrix} \qquad D = [0]$$

Where:

$$J_{1eq} = J_1 + \frac{J_3}{G^2}$$

$$J_{3eq} = J_3 + J_1 G^2$$

3 Torque Converter Clutch Damper Resonance Characterization Using Torque Transmissibility Frequency Response Functions and Parameter Estimation

Luke Jurmu[a], Darrell Robinette[a] Jason Blough[a], Craig Reynolds[b]

[a]Department of Mechanical Engineering
Michigan Technological University
1400 Townsend Dr, Houghton, MI 49931, USA
lukejurmu@hotmail.com
dlrobine@mtu.edu
jrblough@mtu.edu

[b]General Motors Company
P.O. BOX 33170
Detroit, MI 48232-5170, USA
Craig.Reynolds@gm.com

Corresponding author: Luke Jurmu

3.1 Background

Torque converter research, funded by General Motors, has been going on at Michigan Tech for the last ~20 years. A torsional shaker was developed and integrated into the existing torque converter test cell to measure frequency response functions of the torque converter [62]. The frequency response data, when correlated with simulation data, improves the accuracy of torque converter damper models, which in turn improves full drivetrain models.

3.2 Abstract

A unique torque converter test setup was used to measure the torque transmissibility frequency response function of four torque converter clutch dampers using a stepped, multi-sine-tone, excitation technique. The four torque converter clutch dampers were modelled using a lumped parameter technique, and the damper parameters of stiffness, damping, and friction were estimated using a manual, iterative parameter estimation process. The final damper parameters were selected such that the natural frequency and damping ratio of the simulated torque transmissibility frequency response functions were within 10% and 20% error, respectively, of the experimental modal parameters. This target was achieved for all but one of the tested dampers. The damper models include stiffness nonlinearities, and a speed dependent friction torque due to centrifugal loading of the damper springs. Recommendations include further testing to separate the coulomb friction mechanism from the viscous damping mechanism, testing with the torque converter operating in open mode, and tests on a series of customized dampers with centrifugal pendulum absorber hardware.

3.3 Introduction

While the automotive industry accelerates toward fully electric vehicles, a significant percentage of existing and new vehicle sales are still conventional, internal combustion engine powertrains, and it has been projected to remain so for the near future [63]. For this reason, further development has been taking place on conventional powertrain components to meet increasingly stringent emissions and fuel economy regulations. Automobiles are becoming more efficient, powerful, and accelerating faster year over year [1]. To achieve these gains, strategies like stop-start, fixed and variable cylinder deactivation, direct injection, turbo charging, and engine down-speeding have been implemented. Engine down-speeding is achieved with more transmission gears and an aggressive upshift schedule. For vehicles with conventional powertrains, these strategies result in increased torsional vibration amplitudes at lower frequencies in the drivetrain. Direct injection and turbo charging enable higher brake torque at lower engine speeds which increases torsional vibration amplitudes. Cylinder deactivation schemes and engine down-speeding lowers the frequency of torsional vibrations output by the engine. In general terms, a trend of increasing amplitude, decreasing frequency torsional vibrations in the drivetrain will negatively affect ride comfort and durability [14, 64-66]. This drives the need for improved torsional vibration isolation performance from torsional vibration dampers.

A widely used torsional vibration damper is the torque converter clutch (TCC) damper in conventional powertrains. Testing and modeling have become critical to understanding how the TCC influences drivetrain noise vibration and harshness (NVH) phenomena., Drivetrain NVH pertaining to the TCC has been widely studied [12-19] because accurate TCC models are necessary to have confidence in these drivetrain models. A variety of test setups have been deployed to characterize the TCC and to validate their respective models [20-25, 46]. A few studies have used a special test rig to measure the torque transmissibility frequency response function (TTFRF) of the TCC in isolation, while loaded under simulated vehicle operating conditions [23-25, 46]. This particular test rig is limited by how low in frequency the TCC can be excited, and low frequency data points were extrapolated from higher frequency data. Thus the TCC resonance is not well characterized with experimental data.

Likewise, a variety of model based studies have been carried out to investigate the influence of TCC parameters on drivetrain vibrations, or to improve TCC modelling [65, 67-72]. Published TCC models commonly include piecewise linear stiffness curves, hysteresis or friction, and preload nonlinearities, which have been shown to significantly influence drivetrain NVH. Speed dependent friction is a mechanism that hasn't been widely published, but which is analytically addressed in [67]. Essentially, the centrifugal loading on the springs causes an increase in friction acting on the damper springs.

This work sets out to estimate physical TCC damper parameters of stiffness, damping and friction by experimentally characterizing the TCC damper resonance with a torque converter dynamometer setup that has torsional excitation capability. The torque converter is tested with the clutch locked, the input (pump) driven under 150 Nm of mean

torque, and the output (turbine) controlled to a constant speed ranging from 500 to 2000 rpm. The TTFRF of four different TCC designs are measured in the torque converter test rig. The experimental TTFRF is then used to estimate TCC model parameters (stiffness, damping, friction), and the subsequent simulated TTFRF is compared to test data as model verification.

3.4 Experimental Setup and Test Methods

The following sections will provide an overview of the torque converter clutch damper hardware tested, a detailed description of the torque converter specific dynamometer setup, the torsional excitation testing, and the data processing necessary to compute a TTFRF.

3.4.1 Torque Converter Hardware

The automotive torque converter has evolved since its invention and continues to do so. Its role changes with enhancements to internal combustion engine technology, operating strategy as well as powertrain electrification. The dimensions and volume of the torus elements continue to shrink, displaced by packaging volume for various designs of spring-mass systems, and more recently centrifugal pendulum dampers [73]. The reliance on the hydrodynamic torus has diminished in favor of aggressive TCC apply and lockup at lower engine and vehicle speeds and higher engine torque. With increased utilization of the TCC damper comes increased engineering effort to design the mechanical system with enhanced torsional isolation. An example torque converter used in a modern rear wheel drive planetary automatic transmission is shown disassembled in the left of Figure 3.1.

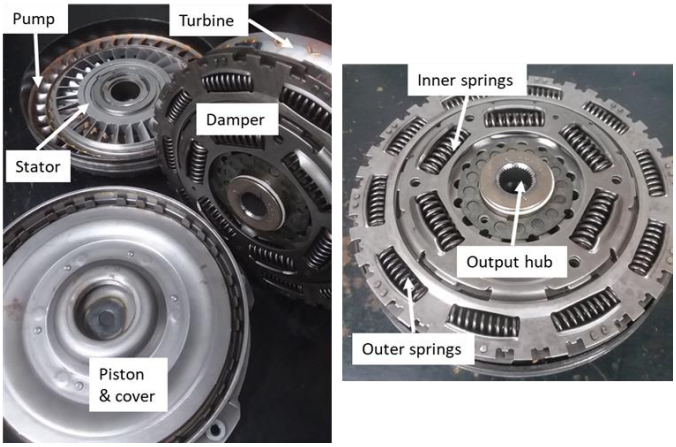

Figure 3.1. Disassembled (cut apart) torque converter showing torus, damper, clutch piston with pump cover (left), and close up view of series spring damper hardware (right).

Four torque converters with unique clutch damper configurations and parameters were tested on the torque converter dynamometer setup. Torsional excitation inputs were used to characterize the damper resonant behavior and extract properties for developing correlated, nonlinear models. The four designs were selected strategically for this

investigation to quantify the behavior and contribution of particular components or integration of components. A summary of the major existing TCC damper configuration and design features available are contained in Figure 3.2, see [73-75]. The green boxes indicate the configurations and design features included in the four TCC dampers tested, covering conventional vs. turbine damper, single, parallel and series springs stages. This includes CPAs, a Belleville washer. The spring stages are composed of linear and arc springs that have unique friction characteristics depending on how they are retained within the dampers drive plates.

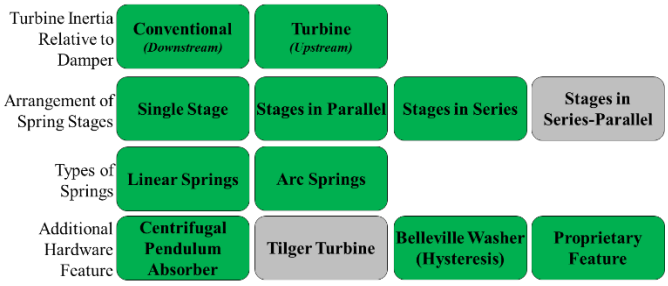

Figure 3.2. Summary of TCC damper configuration and design features to achieve performance objectives.

The TCC dampers tested include three turbine dampers (TD) TCC designs [64] and one conventional damper (CD) design. One of the TD TCC's features a centrifugal pendulum absorber (CPA), see [2, 36, 73, 74]. The other TD and CD are constructed with a single spring stage with linear springs. The remaining TD consists of two linear spring stages arranged in series with a Belleville hysteresis washer on one of the stages. The CPA TD TCC design is composed of an arc spring before the turbine, a straight spring after the turbine, and a CPA coupled to the turbine inertia.

Individual springs installed in any TCC damper have a combination of internal friction and friction between the spring and drive plate spring retaining features. Additionally, if springs are nested, the relative motion between the spring coils can also produce friction. The cumulative sum of these friction forces across all springs within a stage produce hysteretic damping. Hysteretic damping can be a function of the spring and drive plate materials, operating speed and torque, as well as ATF properties. Each spring stage of the TCC dampers tested will be represented and modeled as constant, function dependency friction, and/or equivalent viscous damping. Figure 3.3 contains high level diagrams for the distribution of inertias, spring stage stiffness, friction, and damping for each of the four TCC dampers considered in this investigation. More specifically, each spring stage of the tested dampers were modelled with a stiffness, viscous damping, and friction element in parallel.

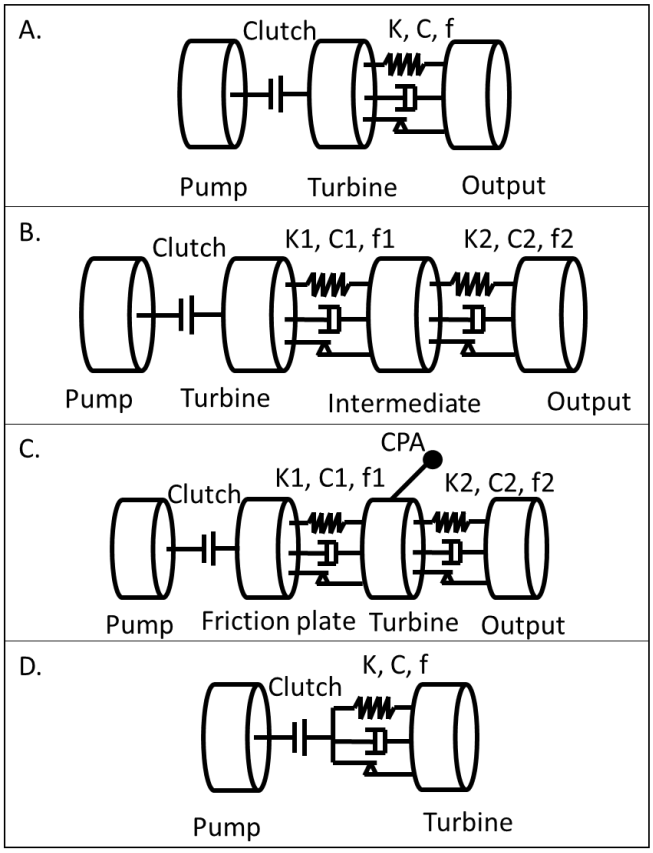

Figure 3.3. TCC hardware architectures. A) TD, single stage. B) TD, two stage. C) Two stage damper with CPA. D) CD, single stage. Schematic elements are not to scale.

For an additional perspective on TCC damper configurations, TCC damper B in Figure 3.3 is the TCC damper featured in Figure 3.1 (right). This highlights the outer, linear springs connected in series via an intermediate plate to the inner, linear springs that drives the output hub coupled to the transmission input shaft. Although not clear in Figure 3.1, the turbine of the torus is mounted directly to the clutch damper plate that contains the outer springs. The overall classification of TCC damper "B" in Figure 3.1 and 3.3 is a series spring turbine damper [64, 74].

The overall equivalent stiffness of the clutch damper when both spring stages are acting in series is given by,

$$k_{eq} = \left(\frac{1}{k_1} + \frac{1}{k_2} \right)^{-1} \qquad (1)$$

where k_1 and k_2 represent the equivalent stiffness of the outer and inner spring stages respectively. The springs within a given stage, k1 or k2, are arranged in parallel, thus the total stiffness of each spring stage is the numerical sum of individual springs.

The design of the spring stages for the TCC damper “B” is such that the outer and inner spring stages have different torque vs. displacement. During operation, once the softer spring reaches its deflection limit (bottomed out), the stiffer spring will become the remaining spring in the system. This will create a step change or “knee” in the overall torque vs displacement plot.

Thus, there are effectively two equivalent spring stiffness regions for TCC damper B. Figure 3.4 summarizes the nominal torque vs. angular displacement or composite TCC damper stiffness curves. The stiffness curves of the two single stage TCC dampers (A and D in Figure 3.3) are linear over the entire deflection range, while the two multi-stage TCC dampers (B and C in Figure 3.3) show two distinct linear stiffness regions.

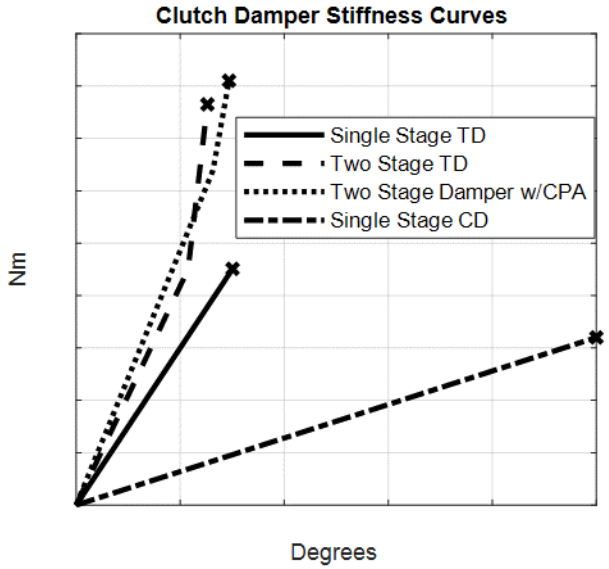

Figure 3.4. Overall torque vs. deflection Stiffness curves of the tested TCC dampers.

TCC parameters other than stiffness was measured or specified by the manufacturer of the torque converters, and the equivalent stiffness and friction of each spring stage are reported (Table 3.1 and Table 3.2). For two of the TCC dampers, a nominal value of friction dependent on speed was noted, and simulates the effects of centrifugal loading on the springs. Damping coefficients are not reported in Table 1 because damping is not a design parameter for the TCC damper system. One of the benefits of the torsional testing and TTFRF method will be the estimation of friction and damping from dynamic loading under representative conditions of TCC operation in a powertrain. The estimated friction and damping will be incorporated in the lumped parameter models described in the results section.

Table 3.1. Nominal TCC damper parameters measured or specified by the TC manufacturer or specified by the vehicle-powertrain application

TCC Hardware	K1 (Nm/deg)	K2 (Nm/deg)	f1 (Nm)	f2 (Nm)	CPA Order

One Stage TD	15		Table 2		
Two Stage TD	85	28	17	Table 2	
Damper w/CPA	43	55		5	2
One stage CD	3		TBD		

Table 3.2. Nominal speed dependent TCC damper friction specified by the TC manufacturer.

Speed	Friction
0	2
1000	2
2000	3
3000	7

3.4.2 Torque Converter Dynamometer Setup with Torsional Excitation

The dynamometer test setup in Figure 3.5 was previously developed and presented in detail in [62], and has previously been utilized to test a unique driveline torsional vibration absorber [11]. For this investigation it is setup as a torque converter and TCC damper dynamic input and absorbing dynamometer as detailed in Figure 5. The torsional actuator is an off the shelf permanent magnet electric motor operating at 700 VDC with a peak output of 160 kW and 320 Nm. Torsional excitation is described in more detail by [76] but has frequency range out to approximately 100 Hz. The absorbing dynamometer is a 343 kW AC electric machine with 820 Nm peak capability. Torque is measured with PCB TorkDisk model 5308D-01A telemetry torque meters, while speed is measured using 150 pulses per revolution tone wheels with magnetic speed pickups. This instrumentation is co-located at the input and output of the torque converter test fixture as noted in callouts c and f in Figure 3.5.

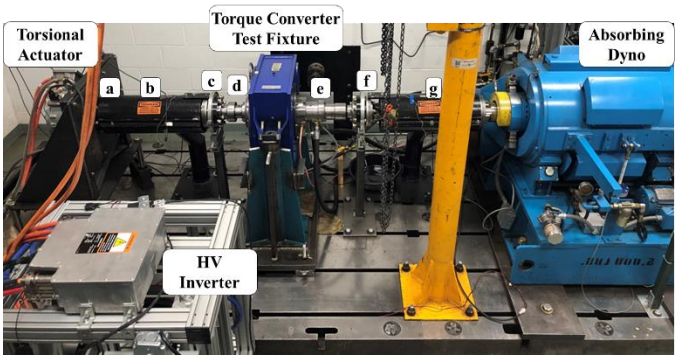

Figure 3.5. Test setup used for measuring TTFRF of the TCC dampers. The torsional exciter is on the left-hand side, device under test in the blue box (center), and the absorbing dyno on the right hand side. a: input coupling inertia, b: Input u-joint shaft stiffness, c: input spindle inertia, d: input spindle stiffness, e: output spindle stiffness, f: output spindle inertia, g: output u-joint shaft stiffness.

3.4.3 Torque Transmissibility Frequency Response Function

A hydraulic system capable of controlling the TCC state was used to lock up the torque converter, and in situ measurements of the locked TCC were made. This way, the hydrodynamics of the torque converter are effectively eliminated from the system, and the TTFRF of the clutch damper assembly could then be measured. TTFRF measurement and test methods were also detailed in previous works [11, 76], and were applied to the TCC dampers in this study. The sample measurement in Figure 3.6 demonstrates how the time domain torque measurement are processed into a TTFRF measurement. First linearly scaled autopower spectra are computed utilizing the Fast Fourier Transform (FFT), and then the TTFRF is calculated as the ratio of autopower spectra (Eq.2).

$$TTFRF = \frac{G_{T_{out}T_{out}}}{G_{T_{in}T_{in}}} \qquad (2)$$

Where $G_{T_{out}T_{out}}$ is the output torque autopower spectrum, and $G_{T_{in}T_{in}}$ is the input torque autopower spectrum.

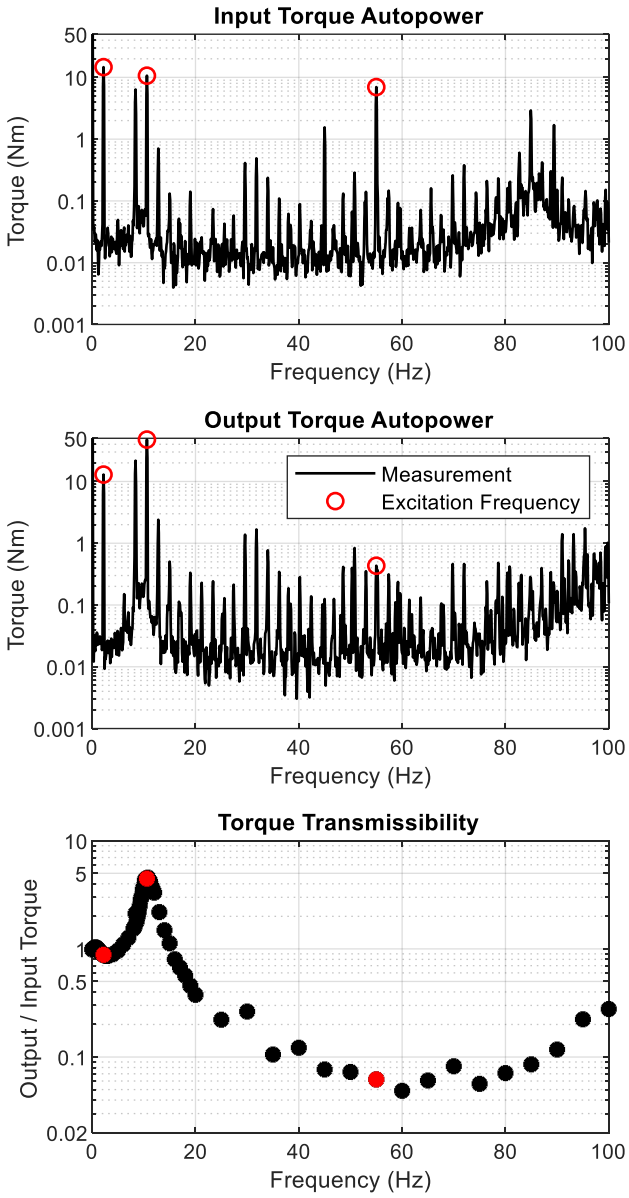

Figure 3.6. Time domain signals are converted to auto power spectra via FFT (Fast Fourier Transform), and then the TTFRF is computed.

A stepped tri-tone excitation method was applied to the input of the torque converter and clutch damper assembly. The stepped tri-tone method saved time and was shown to yield the same TTFRF results as a single sine wave input, provided the excitation frequencies were well spaced (Figure 3.7). The one stage TD was tested with both the stepped sine and the stepped tri-tone excitation while the clutch was applied to validate the stepped tri-tone method. The two measurements techniques resulted in minor difference in the TTFRF, so the stepped tri-tone technique was used to save test time.

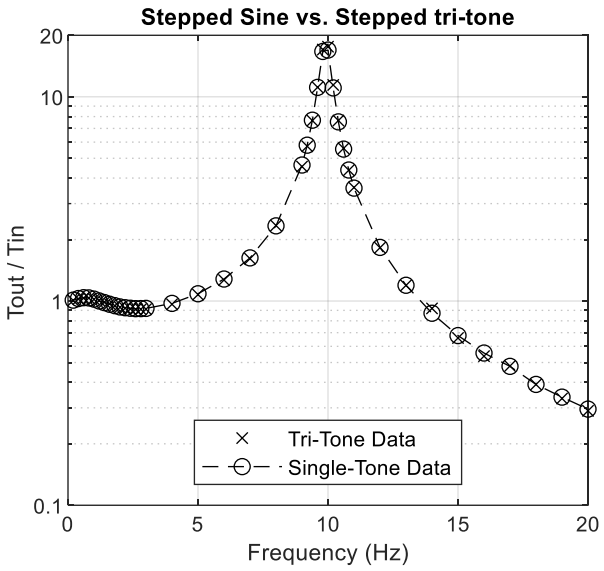

Figure 3.7. Comparison of TTFRF using the stepped sine method and the stepped tri-tone method.

3.4.4 Test Matrix of Hardware and Operating Condition

The frequency of the dynamic torque input ranged from 0-100 Hz, while the TCC was loaded on the input with 150Nm of mean torque, and on the output controlled to a constant output speed that ranged from 500-2000 rpm. Dynamic torque amplitudes varied depending on the specific TCC hardware tested (Table 3.3). These were selected such that torsional vibration amplitudes remained between 0-300 Nm to avoid exceeding motor capability and to avoid exciting lash nonlinearities in the system.

Table 3.3. Operating conditions for the torque converter hardware tested to determine TTFRF.

TCC	Speeds (rpm)	Dynamic Torque
One stage	500, 1000, 1500,	10
Two stage	500, 1000, 1500,	15
Damper	1200, 1500, 1800,	30
One stage	750, 1000, 1500,	40

3.4.5 Dynamometer Test Setup Characterization

Before detailed modeling efforts for the TCC damper variants was undertaken, a series of static, steady state and dynamic tests were conducted to determine dynamometer test setup inertias, shaft stiffness, torque spin loss and the presence of any dynamometer feedback control modes that might appear in frequency response functions. These tests were completed to ensure that the parameter estimation, system dynamics characterized by the frequency response functions, and data analysis performed was aligned with the torque converter damper system and not the test setup.

Static tests included hanging calibrated dead weights on load arms with an angle of deflection measurement to determine stiffness and modal analysis to determine typical system torsional and bending modes of vibration. Steady state testing included two separate procedures to determine the torque spin loss at the input and output sides of the dynamometer setup. The input to the system included rotating elements from the input drive electric motor through to the test fixture input spindle (Figure 3.5 a-d). The output of the system included all rotating element from the test fixture output spindle to the absorbing dynamometer (Figure 3.5 e-g). Dynamic speed sweeps of constant angular acceleration were used to determine inertias of the electric motors, shafts, couplings and other non-torque converter related rotating components. The inertias of the torque converters were provided from prior modeling and testing with sufficient detail to separate all inertia nodes of the hydrodynamic unit and the clutch damper assembly. The inertia of the hydrodynamic unit included transmission oil filling all fluid passages, cavities and blade passages.

A lumped parameter model of the test setup was made, reflecting the inertia, stiffness, and spin loss phenomena that was measured in the system (Figure 3.8). This model is analogous to Figure 3.5, with the torsional actuator electric motor on the left, the torque converter test fixture in the middle and absorbing dynamometer on the right.

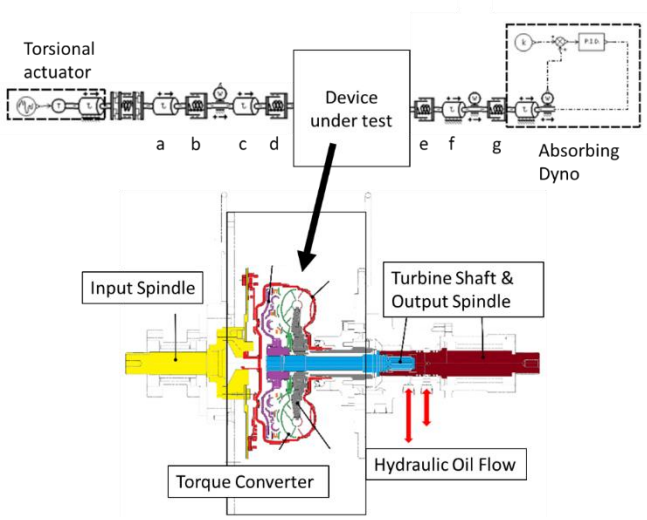

Figure 3.8. Top: Lumped parameter model of the test setup. a: input coupling inertia, b: Input u-joint shaft stiffness, c: input spindle inertia, d: input spindle stiffness, e: output spindle stiffness, f: output spindle inertia, g: output u-joint shaft stiffness. Bottom: Cross section view of the device under test in the test fixture.

The absorbing dynamometer was operated in speed control mode during all torque converter testing. This dynamometer control mode utilized a PI controller feedback. All of the measured TTFRFs showed a 1 Hz mode, and it was hypothesized that this mode was an artifact of the absorbing dyno's speed controller. Two different load cases were run while measuring the TTFRF of the two stage TD to test this hypothesis. The first load case was as previously described (input torque: 150Nm, output speed: 1200 rpm), and the

second load case had the absorbing dyno controller turned off. To measure the TTFRF in the second load case, the input motor was spun at a mean rotational velocity of 1200 rpm, while a sinusoidal rotational velocity of 50 rpm amplitude was used as the torsional excitation. The resulting TTFRFs, with the absorbing dynamometer speed controller active and inactive, showed that the 1 Hz mode was a result of the output dynamometer speed control (Figure 3.9). Also, when testing with the speed controller turned off, the TTFRF of the two stage TD looked non-linear, and had a different natural frequency than when tested with the output dyno on. This difference in TTFRF made sense, since the lash—between the turbine shaft and output spindle—in the system was excited, and the sharp drop represented a transition from double sided impacts, to single sided impacts. The important observation is the disappearance of the 1 Hz mode from the TTFRF when operating without the output dyno speed controller. A PI speed controller was added to the absorbing dyno inertia in the lumped parameter model to replicate the 1Hz mode in the simulation (refer back to Figure 3.8).

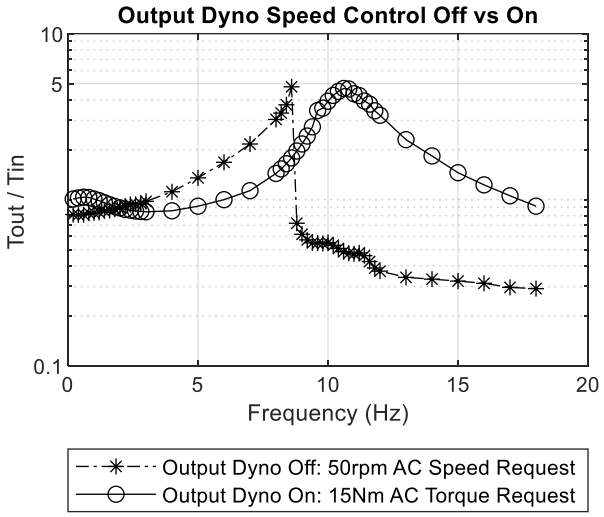

Figure 3.9. Measured TTFRF using different loading in the test cell. First using speed control on the input motor, and output dyno off, and second using the input torque/output speed control load case.

3.5 Torsional Test and Lumped Parameter Model Results

The experimental TTFRFs were plotted over the 0-20 Hz frequency range to capture the damper resonance. System dynamics beyond 20 Hz were not relevant for characterizing the damper mode. In the case of the two stage damper with CPA, a wider bandwidth was used to capture the 2nd order CPA dynamics. The simulated TTFRF was also superimposed on the experimental data, to achieve a side by side comparison of how well the simulation replicated the experimental results. In all of the plots, the prominent resonance was the damper mode, and it was apparent that with increased speed, came an

increase in peak attenuation. This behavior was expected as a result of centrifugal loading on the damper springs, and the TCC models were tuned with a speed-friction torque lookup table to replicate this behavior.

The lumped parameter model architectures of each damper were provided along with the manufacturer specified TCC parameters (including stiffness, damping, and hysteresis). These specifications were used as a starting point to parameter estimation. After measuring the TTFRF of the dampers, stiffness elements of each respective model were tuned iteratively such that the natural frequency of the model result matched the experimental results. To estimate the structural damping in each spring set Equation 3 was used, and includes scaling factors to have units of Nm/rpm.

$$c = \frac{\eta k 6}{\omega} \tag{3}$$

The loss factor (η) was assumed to be 0.02 for steel spring elements, and the frequency (w) was set to 70 Hz (439.6 rad/s), which represented the median engine firing frequency. Then, coulomb friction was tuned iteratively such that the peak amplitudes of the simulation and experiment matched. In order to model the effects of speed dependent friction, the TTFRF was measured at several speeds. Then, friction elements in parallel with the clutch spring elements were used to model friction, using a hyperbolic tangent friction model, and the speed dependency was modelled crudely with a speed to friction torque lookup table. The lookup tables were tuned to match the speed dependent amplitude change in the measured TTFRF.

3.5.1 One Stage Turbine Damper

The one stage TD was a lightly damped system, and was expected to have low levels of friction. Thus the resonance was sharp and narrow (Figure 3.10). As speed increased, so did the amount of damping. This was explained by the increased friction force between the spring and its cage as a result of centrifugal loading on the straight springs. Along with the peak attenuation, came a slight reduction in the resonant frequency. The hyperbolic tangent coulomb friction model adequately simulated the experimentally acquired TTFRF. The lumped parameter model of the one stage TD contained a hydrodynamic torque converter sub model, a lockup clutch, and damper components (Figure 3.11). The damper stiffness, and friction element lookup table were tuned to achieve the simulated TTFRF in Figure 3.10. The experimental and simulated TTFRF data was interpolated with a spline interpolation in order to improve the accuracy of the natural frequency and damping ratio estimates. The damping ratio and natural frequency of the simulated TTFRF were within 20% and 2% error respectively of the experimental TTFRF (Table 3.4), and the damper parameters used to achieve these simulation results are discussed in the next section.

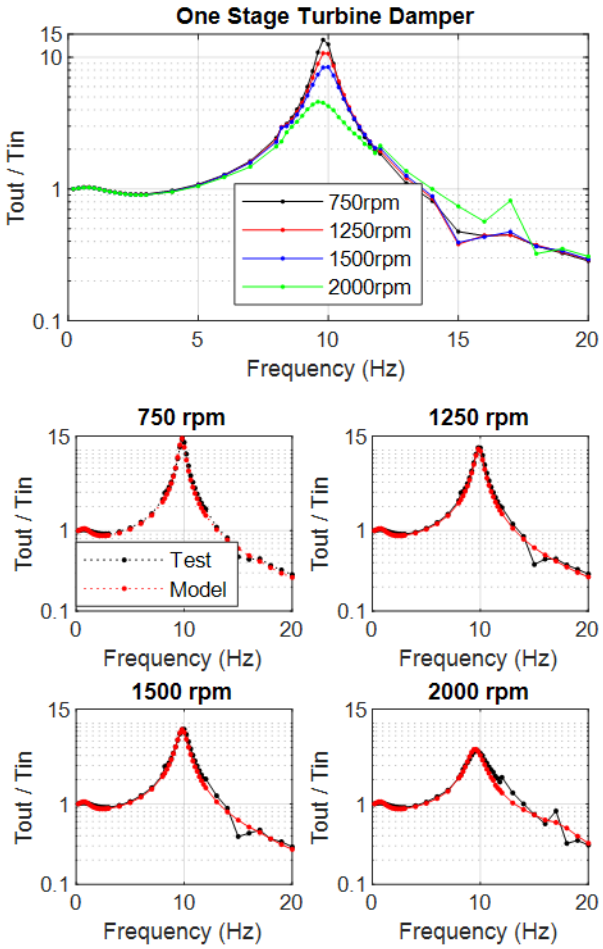

Figure 3.10. Experimental TTFRF of a single stage TD (top). Simulated TTFRF at each rotational speed (bottom four).

Table 3.4. Percent error in modal parameters (damping ratio and natural frequency) between test data and model data.

Speed (rpm)	fn (Hz) test/model	ζ test/model	% error in ζ	% error in fn
750	9.85/9.79	0.032/0.027	14	0.6
1250	9.90/9.86	0.039/0.037	6	0.4
1500	9.92/9.82	0.049/0.046	7	1
2000	9.68/9.55	0.091/0.074	18	1.4

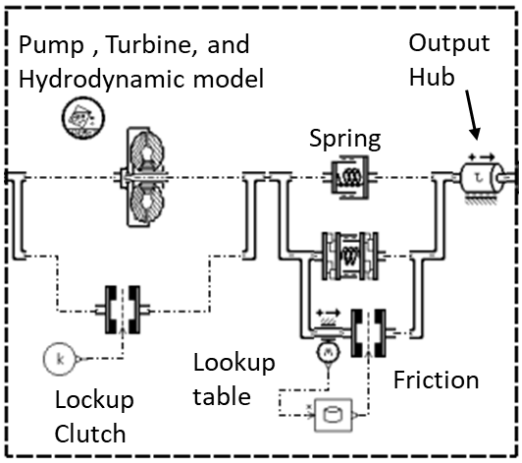

Figure 3.11. Model architecture of one stage TD.

3.5.2 Two Stage Turbine Damper

The two stage TD was a more heavily damped system than the one stage TD by design. This damper design contained a Belleville spring whose intent was to add a constant level of friction to the system. Thus the damper resonance of the two stage TD was lower in amplitude and of wider bandwidth than the single stage TD (Figure 3.12). Again, like the one stage TD, the resonant peak moved down in frequency and amplitude with increased speed. The hyperbolic tangent friction model was adequate in simulating the TTFRF of the two stage TD at several speeds. The model architecture of the two stage TD was similar to the one stage TD, and contained additional spring, and friction elements. All of the speed dependent friction in this model was lumped into one friction element (in parallel with spring 2, Figure 3.13). The damping ratio and natural frequency of the simulated TTFRF was within 20 % and 5% respectively of the experimental TTFRF (Table 3.5).

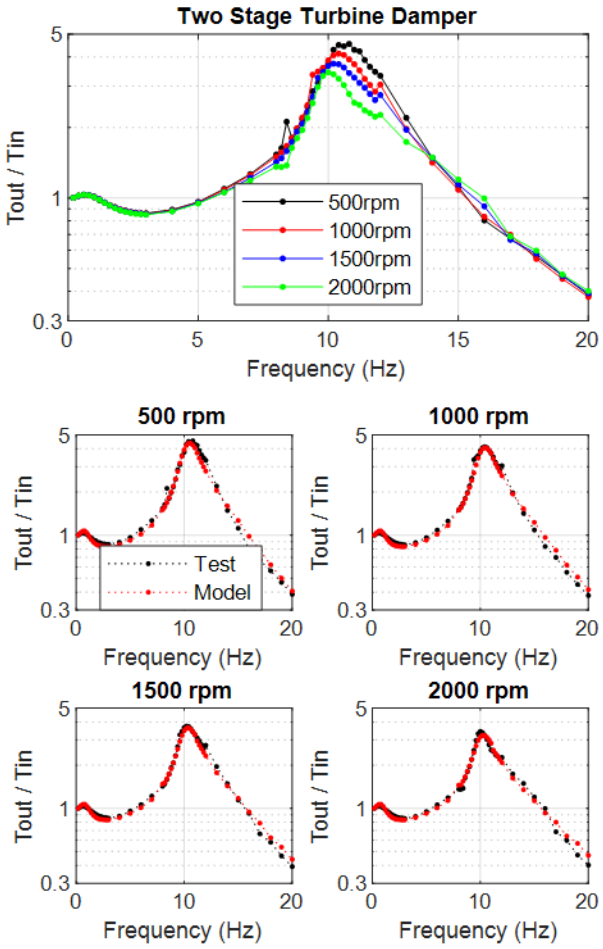

Figure 3.12. Experimental TTFRF of a two stage TD (top). Simulated TTFRF at each rotational speed (bottom four).

Table 3.5. Percent error in modal parameters of two stage TD (damping ratio and natural frequency) between test data and model data.

Speed (rpm)	f_n (Hz) test/model	ζ test/model	% error in ζ	% error in f_n
500	10.88/10.54	0.109/0.101	6.95	3.12
1000	10.74/10.49	0.130/0.104	20.4	2.37
1500	10.65/10.41	0.113/0.108	4.2	2.23
2000	10.60/10.34	0.109/0.113	3.5	2.52

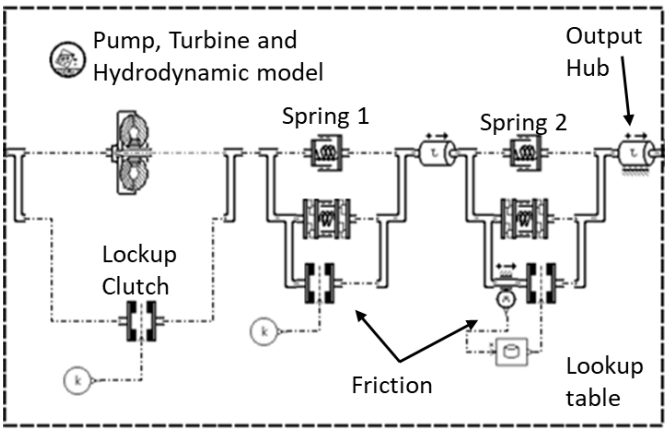

Figure 3.13. Model architecture of two stage TD.

3.5.3 Two Stage Damper with CPA

The TTFRF of the two stage damper with CPA contained more features than the previous two dampers. An anti-resonance existed about the frequencies that coincided with the tuning order of the CPA—in this case 2nd order. It was also found that the test setup contained a mode of vibration near 100 Hz (Figure 3.14). This mode appeared in all of the other TTFRF measurements as well, but was well removed from the TCC resonance, and thus not compromising to the damper characterization. The damping ratio and natural frequency of the simulated TTFRF was within 11 % and 10% respectively of the experimental results (Table 3.6).

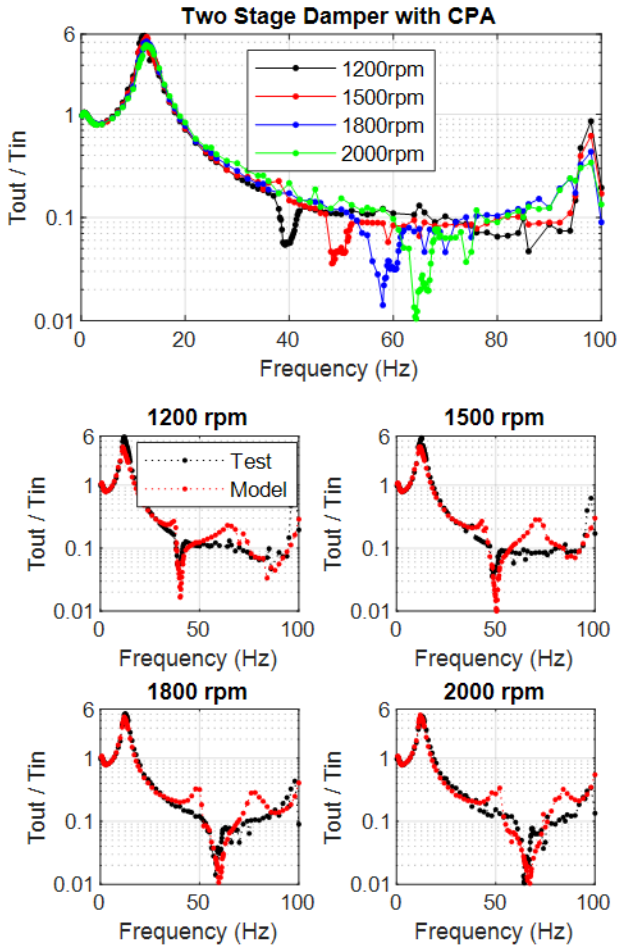

Figure 3.14. Experimental TTFRF of a two stage damper with a 2nd order CPA (top). Simulated TTFRF at each rotational speed (bottom four).

Table 3.6. Percent error in modal parameters of two stage damper with CPA (damping ratio and natural frequency) between test data and model data.

Speed (rpm)	f_n (Hz) test/model	ζ test/model	% error in ζ	% error in f_n
1200	12.28/11.31	0.102/0.099	3.54	7.97
1500	12.72/11.88	0.098/0.108	10.7	6.61
1800	12.64/12.09	0.111/0.107	3.37	4.34
2000	12.62/12.07	0.119/0.106	10.7	4.37

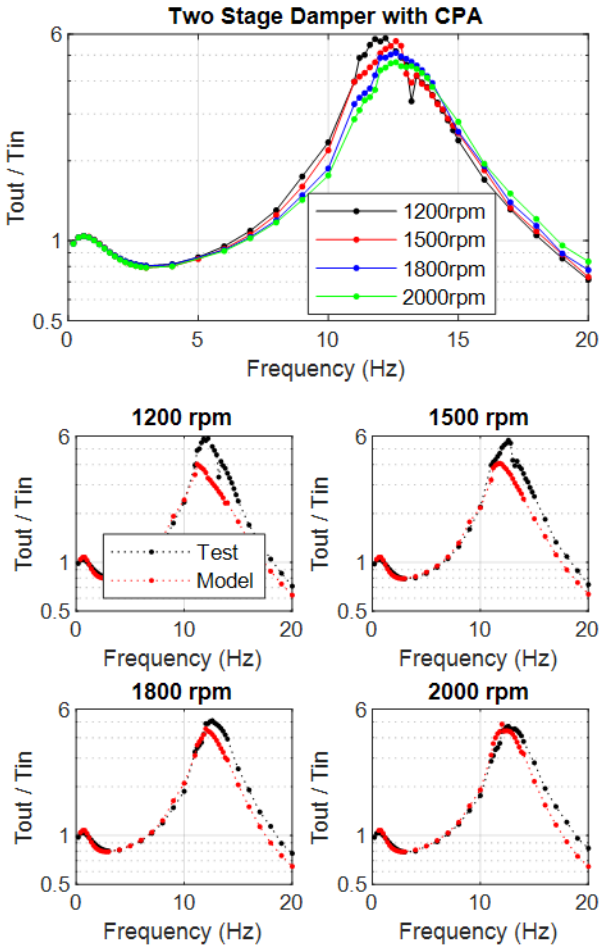

Figure 3.15. Experimental TTFRF of a two stage damper with a 2nd order CPA (left). Simulated TTFRF at each rotational speed with focus on the damper resonance (right).

This damper also displayed decreased resonance amplitude with increased rotational velocity, as with the previous two designs, but instead of the natural frequency decreasing with increased speed, an increase was observed (Figure 3.15). For this particular damper, proprietary sub models of the arc spring and CPA were used to simulate its TTFRF in the test rig. Arc springs have been known to have a stiffening effect as friction increases, and as portions of the arc spring stick, the arc spring becomes stiffer [70]. This model was not tuned further because of the complexity of these sub models, and the percent error in natural frequency and damping ratio acceptable (Table 3.6). The lumped parameter model of the two stage damper with CPA consisted of the arc spring sub model between the pump and turbine inertias, a CPA model coupled to the turbine, and a straight spring element between the turbine and output hub inertias (Figure 3.16).

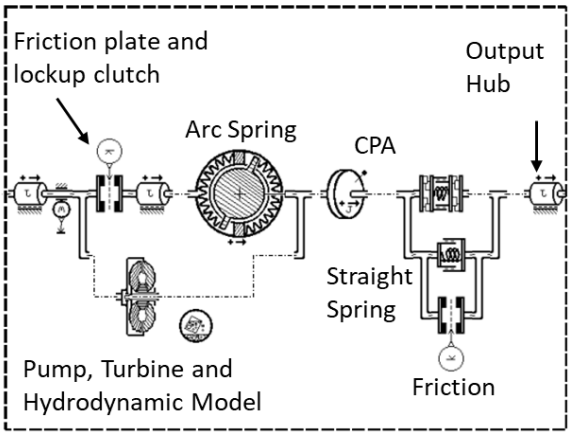

Figure 3.16. Two stage damper with CPA model architecture.

There was a difference between the test results and the simulated TTFRF at the CPA anti-resonance (Figure 3.17). The tuning frequency (minimum amplitude of anti-resonance), amplitude, and general shape differed between model and test results. Further testing, and detailed study of the CPA should be undertaken to improve model correlation about these 2nd order frequencies.

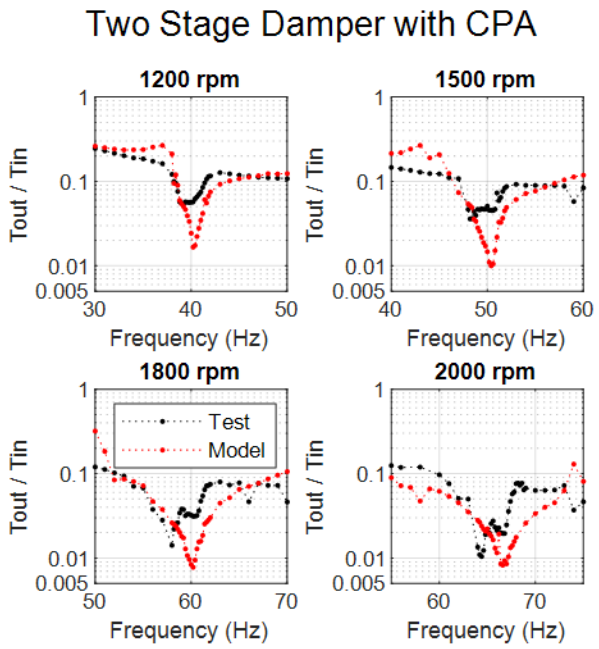

Figure 3.17. Experimental TTFRF of a two stage damper with a 2nd order CPA (left). Simulated TTFRF at each rotational speed with focus on the CPA feature (right).

After testing the damper w/CPA at various output speeds, several metrics of the CPA anti-resonance were looked at (Table 3.7). Frequency and order bandwidth (BW) were quantified as start-end point of the CPA's influence on the TTFRF plot. Order bandwidth and tuning order remained constant with change in speed as expected. Q factor and damping ratio are computed from the CPA anti-resonance, similar to computing these

values from a resonant peak using the half-power bandwidth method, where ω_2 and ω_1 are selected down 3 dB from the peak's maximum. For an anti-resonant valley, ω_2 and ω_1 are selected up 3 dB from the valley's minimum.

$$\zeta = \frac{\omega_2 - \omega_1}{\omega_n} = \frac{1}{2Q} \qquad (4)$$

Table 3.7. Performance metrics estimated from torsional test data for two stage damper with CPA.

Operating Speed (rpm)	Frequency BW (Hz)	Order BW	Tuning Order	Q-factor	ζ
1200	6	0.3	1.960	16.3	0.031
1500	6	0.24	1.928	15.1	0.033
1800	10	0.33	1.930	48.3	0.010
2000	10	0.3	1.932	107.3	0.005

When looking at the frequency based metrics of the CPA's performance (Frequency bandwidth, Q factor, and damping ratio), it appears that the CPA's performance changes with a change in speed, but when looking at the order based metrics, the CPA performance appears speed independent. Tuning order is pretty constant as is the order bandwidth.

3.5.4 One Stage Conventional Damper

The single stage CD has a highly damped, low frequency resonance (Figure 3.18). By design this particular TCC contains a low equivalent stiffness, and also has a high level of friction designed into the damper mechanism. Compared to the other damper designs, a much larger excitation amplitude was required to excite this dampers resonance (refer back to Table 3.3). As the operating speed increased, the resonance amplitude decreased, and the natural frequency also shifted higher. The hyperbolic tangent friction model does not replicate this stiffening effect, and it is hypothesized that an arc spring sub-model would be a better candidate at replicating this dampers dynamics. The architecture of this particular damper design was not known, and the simplified lumped parameter model (Figure 3.19) was inadequate for replicating the TTFRF. The damping ratio and natural frequency of the simulated TTFRF were not within the 20% and 10% error targets (Table 3.8).

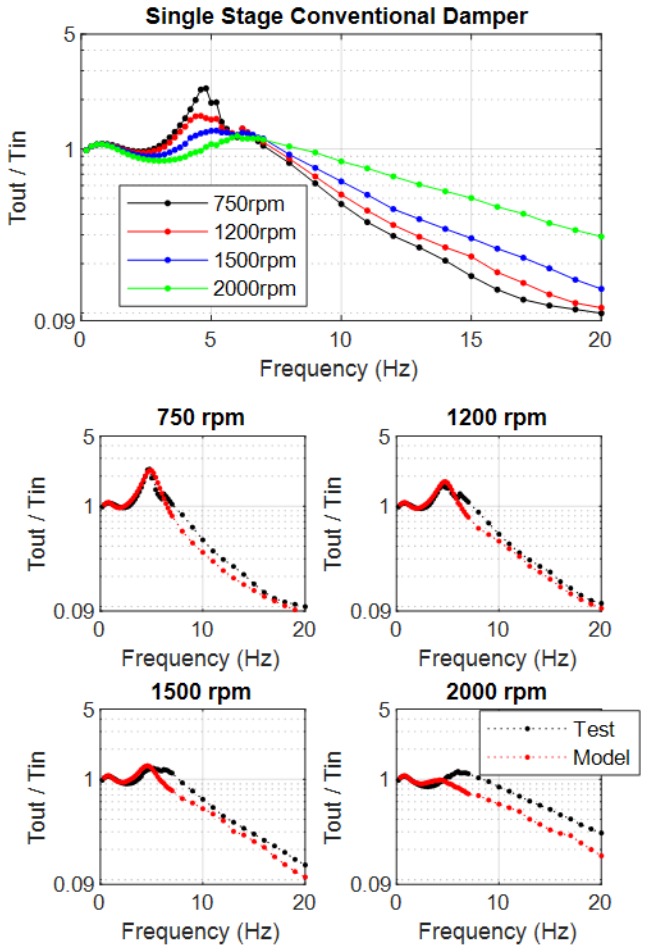

Figure 3.18. Experimental TTFRF of a single stage CD (top). Simulated TTFRF at each rotational speed (bottom four).

Table 3.8. Percent error in modal parameters of one stage CD (damping ratio and natural frequency) between test data and model data.

Speed (rpm)	f_n (Hz) test/model	ζ test/model	% error in ζ	% error in f_n
750	4.75/4.96	0.121/0.176	45.9	4.27
1200	4.88/4.86	0.375/0.240	35.9	0.269
1500	5.85/4.84	0..482/0.269	44.1	17.3
2000	7.19/4.83	0.557/0.291	47.7	32.8

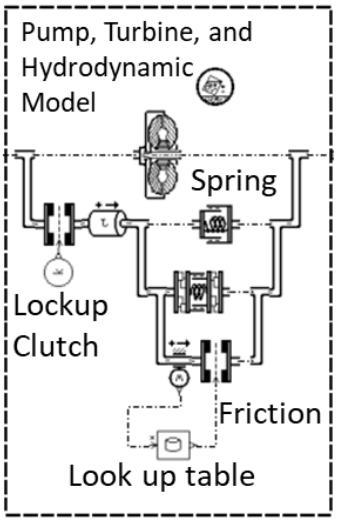

Figure 3.19. One stage CD model architecture.

3.5.5 Damper Comparison

For some perspective on the torsional vibration isolation performance of each of the tested hardware, TTFRFs at 1500rpm are plotted in Figure 3.20. In the 0-60 Hz range shown, the one stage CD had the lowest TTFRF amplitude, which translates to best isolation performance, in the 6-40 Hz range. The two TD hardware had more lightly damped designs than the one stage CD, and the isolation wasn't good when operating at these dampers' resonances. When operating far enough above the resonance however, torsional vibrations were attenuated better than with the one stage CD. So while the one stage CD outperforms the two TD in the 6-40 Hz range, the two TD have a lower amplitude TTFRF beyond 50 Hz.

With regards to the two stage damper with CPA, it performed the worst of all hardware in the 6-40 Hz range, but when looking at frequencies about 2nd order (CPA tuning order), it had the lowest amplitude TTFRF which translates to the best torsional vibration isolation performance. This 2nd order is critical to consider because 2nd order coincides with the frequency of engine torsionals when operating in V4 mode. So with respect to isolating

the engine torsional vibrations from the downstream drivetrain, the CPA outperformed all other tested hardware.

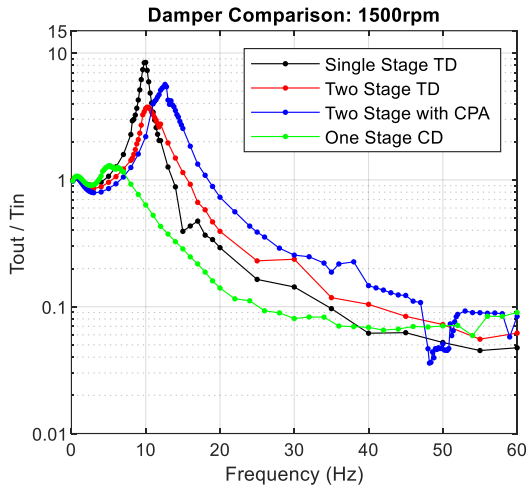

Figure 3.20. Experimental TTFRF of all torque converter dampers.

3.6 Parameter estimation

Four TCC damper designs were characterized in a unique torque converter fixture using the TTFRF, respective lumped parameter models were tuned to simulate the measured data. Using the manufacturer specified TCC model parameters as a starting point, the TCC models were tuned to meet the % error target in natural frequency and damping ratio. The tuned TCC damper model parameters used to simulate the TTFRF of each damper design are listed in Table 3.9 and Table 3.10. These parameter values achieved the target % error in frequency and damping ratio of 10% and 20% respectively.

The manufacturer has a specified tolerance band on the equivalent stiffness of the entire damper, and in the case of the multi-stage dampers, a tolerance for each stiffness region (Table 3.9). Compared to the damper specification of stiffness, these new stiffness values are relatively close, and remain within the specified tolerance. The changes to the stiffness values are therefore reasonable.

Table 3.9. Clutch damper parameters after model tuning. NA: Not Applicable.

Hardware	One stage TD	Two stage TD	Damper w/CPA	One Stage CD
Stiffness 1 (Nm/deg)	17	77	43	4.5
Damping 1 (Nm/rpm)	0.05	0.02	NA	0.2
Friction 1 (Nm)	Table 10	12	NA	Table 10

Stiffness 2 (Nm/deg)	NA	33	55	NA
Damping 2 (Nm/rpm)	NA	0.3	0.04	NA
Friction 2 (Nm)	NA	Table 10	2	NA
Stage 1 Tolerance (Nm/deg)	± 2	± 2	± 2.5	NA
Stage 2 Tolerance (Nm/deg)	NA	± 9	NA	NA

Table 3.10. Estimated speed dependent friction parameters by torque converter clutch dampers.

One Stage Turbine Damper		Two Stage Turbine Damper		One Stage Conventional Damper	
Speed (rpm)	Friction (Nm)	Speed (rpm)	Friction (Nm)	Speed (rpm)	Friction (Nm)
0	0	0	0.35	0	4
750	0	500	0.35	750	4
1250	0.5	1000	1	1200	10
1500	1	1500	2	1500	15
2000	3	2000	3	1800	15
3000	5	3000	6.5	2000	20

Per open clutch testing and modeling done in a companion work (Chapter 4), the speed-friction torque tables can be tuned to open clutch TTFRFs, where the damper resonance still shows up in the measurement for the turbine damper architectures. The friction tables are tuned to the open clutch TTFRF, and to match TTFRF amplitude, more damping is needed (in all hardware cases) when simulating the locked clutch operation. The amount of additional damping required varied with the damper hardware in question. The one stage TD only needed 0.05 Nm/rpm of added damping while the two stage TD needed 0.3 Nm/rpm of added viscous damping. This difference can be explained by the difference in K factor between these two pieces of hardware. Assuming that there exists some relative motion between the ATF and the pump and turbine blades when exciting the locked torque converter with torsional vibrations, one would expect a damping effect as a result. The one stage TD has a higher K factor than the two stage TD, and the hydrodynamic torque associated with relative motion of the ATF with the pump and turbine blades would be higher for the lower K factor torque converters. In this way, the additional damping is justified.

By measuring the TTFRF of four different damper designs, real TCC parameters were estimated by tuning model parameters to match the test data. The additional details of speed dependent coulomb friction due to centrifugal loads on the springs, and additional ATF damping achieved a better match between simulation and test results. In future locked clutch testing, excitation amplitude sweeps could be utilized to separate the effects of viscous damping from coulomb friction. Compared to similar works [14, 15, 19, 20], this data contains more data points about the damper resonance, and captures a speed dependent friction phenomenon. This test data is limited in that the speed range tested (500-2000 rpm) doesn't capture the full range (500-6000 rpm) that the hardware is exposed to in vehicle, and that the torsional actuator cannot input torques large enough to transition to higher stiffness regions of the dampers.

3.7 Conclusions

Using a torque converter test rig with unique capability, the TTFRF of four TCC dampers was measured. Using the specified damper parameters of stiffness and hysteresis as a starting point, the TCC damper model parameters were tuned to match the frequency and amplitude of the experimental TTFRF. The final tuned TCC parameters were within the manufacturer specified tolerances, and thus reasonable. It was hypothesized that the relative motion of the ATF over the pump and turbine blades under torsional excitation is an additional damping mechanism, and multiple metrics of CPA performance were reviewed.

Further testing of these same TCC dampers has been carried out in companion paper. The TTFRF was measured while operating with the torque converter clutch open. Testing with the clutch open offer potential insights into the FRF of the hydrodynamic torque converter.

Other future work involves more detailed testing of the CPA hardware. It is of particular interest to understand the contribution of damping the CPA has at the damper resonance, and conversely the contribution of clutch damping on the CPA performance. In order to isolate these sources of damping from one another, a series of custom TCC dampers with CPA will be made. This series of custom hardware includes an unmodified TCC w/CPA, modified hardware with the spring stages locked (CPA active), modified hardware with the pendula locked (spring stages active), and a modified hardware with only one spring stage locked.

3.8 Definitions/Abbreviations

ATF	Automatic transmission fluid
CD	Conventional damper, turbine inertia downstream of damper system
CPA	Centrifugal pendulum absorber

G	Autopower spectrum
NVH	Noise, vibration & harshness
Q	Quality factor
$\mathbf{T_{in}}$	Input torque
$\mathbf{T_{out}}$	Output torque
TCC	Torque converter clutch
TD	Turbine damper, turbine inertia upstream of damper system
TTFRF	Torque transmissibility frequency response function
c	Damping (Nm/rpm)
k	Stiffness (Nm/deg)
η	Equivalent viscous damping ratio
ω	Frequency (rad/s)
ω_n	Damper natural frequency (rad/s)
ζ	Damping ratio

4 Experimental Validation of a, Physics Based, Hydrodynamic Torque Converter Model Using Torque Transmissibility Frequency Response Functions

Luke Jurmu[a], Darrell Robinette[a], Jason Blough[a], Craig Reynolds[b]

[a]Department of Mechanical Engineering
Michigan Technological University
1400 Townsend Dr, Houghton, MI 49931, USA
lukejurmu@hotmail.com
dlrobine@mtu.edu
jrblough@mtu.edu

[b]General Motors Company
P.O. BOX 33170
Detroit, MI 48232-5170, USA
craig.a.reynolds@gm.com

Corresponding author: Luke Jurmu

4.1 Background

Chapter 3 detailed testing and modelling of torque converters operating in locked clutch mode. The torque converter test cell has capability to toggle the clutch state, and the frequency response of the open torque converter was measured. Several torque converter designs were tested in open mode to understand the influences of K-factor, damper architecture, and diameter on the frequency response. As with the locked clutch testing, open clutch data provided further validation of the torque converter model, and also a widely used hydrodynamic torque converter sub-model.

4.2 Abstract

The torque transmissibility frequency response functions of four torque converters were measured while operating at constant speed ratio. In previous works, frequency response function measurements of torque converters contained other test setup dynamics which dominated the measurements. Thus, a unique torque converter dynamometer was deployed to measure said frequency response functions and to quantify torsional vibration isolation performance. For the first time, the frequency response of an open torque converter was measured separate from a vehicle drivetrain. The tested hardware variations covered a range of K factor, diameter, and lockup clutch damper architectures. The experimental results demonstrated the presence of a damper mode (only present in the turbine damper architectures), which showed that the open torque converter transmits enough torsional excitation to excite downstream drivetrain modes. A lumped parameter model of the torque converter and test setup, containing a widely used hydrodynamic torque converter sub-model, was also validated with the test data. The hydrodynamic

torque converter behaved like a low pass filter in the frequency domain, and its performance was characterized with a cutoff frequency. For each torque converter tested, a unique set of hydrodynamic model parameters were used. The best model result produced a percent error less than 15% in the 0-10 Hz frequency range, thus showing that an accurate prediction of the frequency response could be obtained in the 0-10 Hz range from the hydrodynamic torque converter model. The system model's prediction for the natural frequency of the damper mode was consistently wrong, and it was hypothesized that there existed some inertial coupling between the working fluid and mechanical torque converter elements.

4.3 Introduction

4.3.1 Torque Converter Research

While the transportation industry has seen electrification gain momentum in recent years, a recent report by the EPA [1] indicates that internal combustion engine (ICE) technology still dominates the transportation sector, and will likely remain a significant portion of vehicle drivetrain technology (see also [63]). Thus, efforts to increase fuel efficiency and reduce emissions of ICE powertrains remain important. Technologies like turbocharging, engine down speeding, aggressive torque converter clutch (TCC) apply schedules, cylinder deactivation, and engine stop-start are examples of fuel saving strategies that also directly affect torsional vibrations in vehicle powertrains. These technologies simultaneously increase torsional vibration amplitudes and decrease torsional vibration frequency. However, with increasing efficiency comes a need to improve torsional vibration isolation performance [14].

Modelling tools are heavily leveraged when developing a vehicle. Accurate models of the powertrain components are vital in predicting torsional vibrations in a powertrain while in the powertrain development phase. The torque converter (TC) is the powertrains first line of defense in attenuating torsional vibrations and needs to be well characterized to have confidence in predicting powertrain loads and dynamics. Dynamic, physics based models of TCs were previously published in [26, 27] and have been used to simulate TC transient performance [33, 34]. Other dynamic TC models have been derived as well [77-79], but the physics based models have been widely used in simulating vehicle powertrains for solving a wide variety of engineering problems [28-32].

In [34], torsional frequency response functions (FRFs) of the open TC were measured on a transmission dynamometer setup. The torsional FRFs were dominated by a low frequency torsion mode of the test setup, and the FRF of the open TC was not well characterized experimentally. The author's recommended that a special torque converter dyno setup be used to measure the FRF of the torque converter separated from the influence of other system modes. Until now, there are no experimental torsional FRFs of the open torque converter (unmasked by other dynamics), and the physics based model developed by [27] was not validated with experimental FRFs.

This work uses a special torque converter dynamometer, featured in other works [11, 62, 76], to measure the torque transmissibility FRF (TTFRF) of the open TC over a range of speed ratios (0.2 – 0.96). The effects of K factor, an amalgamated property resulting from torque converter element blade geometries, and diameter on the FRF of open TC are discussed, and a previously published physical torque converter model ([27]) validated with the test results.

4.3.2 Torque Converter Introduction

A description of torque converter operation is provided in [27] and summarized here. A cross section of the torque converter is shown in Figure 4.1 for reference. The torque converter consists of a pump coupled to the crankshaft or flywheel. As it spins, it increases the angular momentum of the automatic transmission fluid (ATF) before the ATF enters the TC turbine which is coupled to the transmission input shaft. As the fluid traverses the turbine, angular momentum is extracted, producing a torque which rotates the transmission input shaft. The ATF exiting the turbine flows through the stator which redirects the fluid flow in the same direction as the pump rotation when speed ratio (equation 1) is less than one. This redirection increases the angular momentum of the ATF and reduces the angular momentum loss at the pump, netting a multiplication in torque.

$$SR = \frac{\omega_{out}}{\omega_{in}} \qquad 1)$$

When the torque converter is operating at higher speed ratios above 0.95, the ATF enters the stator blades at an angle such that the torque applied to the stator is negative. A one-way clutch in the stator assembly will allow the stator to rotate with the ATF, pump, and turbine, and the torque converter ceases to multiply torque—torque ratio (equation 2) is one. The point at which the stator begins to rotate with the pump and turbine is called coupling point.

$$TR = \frac{\tau_{out}}{\tau_{in}} \qquad 2)$$

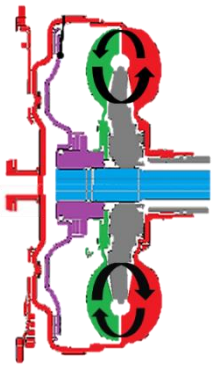

Figure 4.1: Torque converter cross section with arrows depicting toroidal flow of ATF. Red: pump. Green: turbine. Grey: stator. Purple: output hub, piston, and friction interface. Damper hardware is located in empty space between piston and turbine.

Torque converter performance is typically described with TR (equation 2) and K factor (equation 3).

$$K = \frac{\omega_{in}}{\sqrt{\tau_{in}}} \qquad 3)$$

These performance metrics are independent of the exact loading (speeds and torques) of the torque converter, and are a function of SR. The steady state performance data of the four torque converters tested is shown in Figure 4.2.

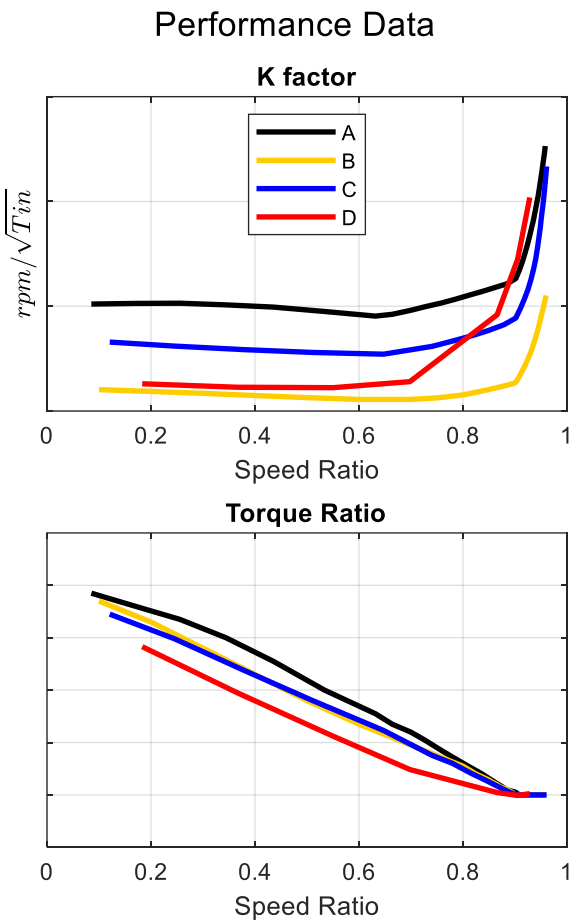

Figure 4.2: Performance data of all torque converter hardware. Coupling point when torque ratio reaches 1—typically around 0.9 speed ratio.

To assess the influence of K factor, diameter, and damper architecture on the TTFRF of the open TC, four torque converters were selected. The pump, turbine, and stator blade design parameters dictate the torque converter performance. The K factor curves show that the four selected TCs represent three different K factors. Figure 4.3 shows the relative size of the tested TCs. The specific values of K factor and diameter are withheld.

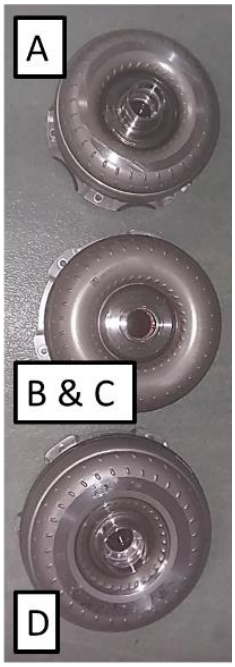

Figure 4.3: Size comparison of torque converter diameters tested. Note that torque converters B and C are identical diameters but have different internal blade geometries.

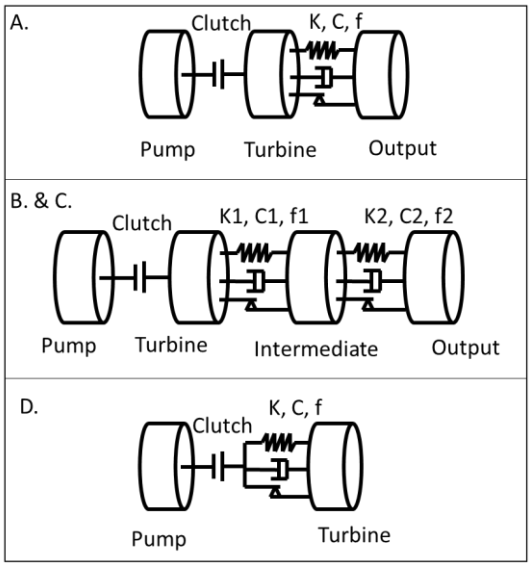

Figure 4.4: Schematics of the damper architectures of each torque converter.

Among the four torque converter hardware, three different damper designs are manifested (Figure 4.4). The damper in hardware A was a single stage turbine damper (TD), where the damper springs couple the turbine to the output hub. Hardware B and C contain an identical damper design: two spring stages in series, in a TD configuration. Lastly,

hardware D had a conventional damper (CD) architecture where the single spring stage couples the friction interface to the turbine—which is in turn splined to the transmission input shaft. For more discussion about damper architecture, refer to companion work about locked clutch operation (Chapter 3).

4.4 Experimental Methods

4.4.1 Torque Converter Dynamometer and Test Methodology

The experimental test setup used to measure TTFRFs of torque converters was previously developed and used to measure TTFRFs of torque converter lock-up clutch dampers, and a unique drivetrain vibration absorber[11, 62, 76]. The loading and signal processing techniques used in these other articles are similar to the test and measurement methods used on the open torque converter, and have been adapted to suit open clutch testing.

First, to simulate the loads on a torque converter in a vehicle, an electric motor repurposed as a torsional shaker was used to apply a torque to the torque converter pump, and a second electric motor (absorbing dyno) was used to apply a speed constraint to the torque converter's turbine (Figure 4.5).

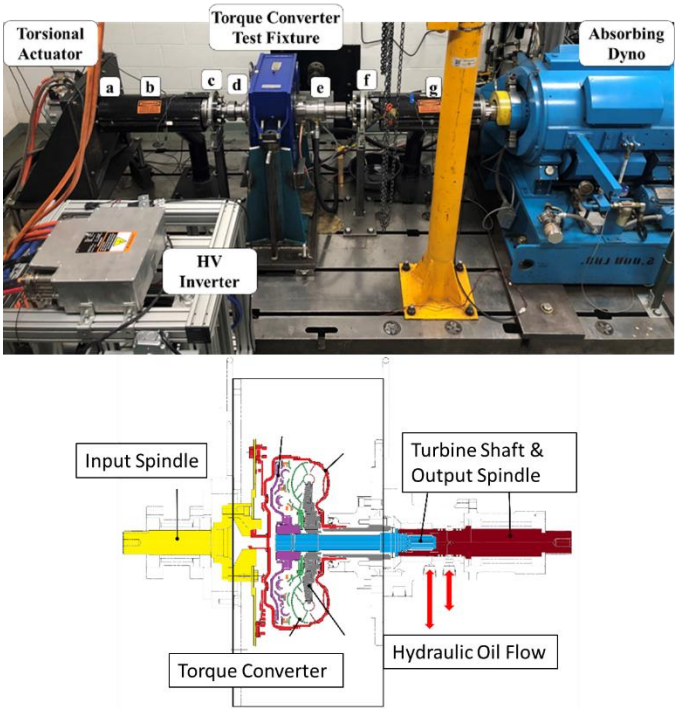

Figure 4.5: Test setup used for measuring torque transmissibility of the torque converters (Top). Cross section view of the torque converter in the fixture (bottom). a: input coupling inertia, b: Input u-joint shaft stiffness, c: input spindle inertia, d: input spindle stiffness, e: output spindle stiffness, f: output spindle inertia, g: output u-joint shaft stiffness

A dynamic torque was superimposed onto the mean torque in the form of three sine waves to excite the torque converter for the TTFRF measurements. Past work has shown that three sine tones produce an equivalent TTFRF to a single sine tone test, when the sine tones were well spaced in the frequency domain. Friction nonlinearities of the test article drove more sine tones to produce a nonlinear response. The motivation for multi-sine testing was a significant reduction in testing time.

The mean torque (75 Nm) and mean speed (200-2500rpm) applied to the torque converter were held constant while the frequencies of the torsional sine waves were swept from 0-100Hz. Measuring the TTFRF under constant speed and mean torque conditions produced a snapshot of the TC's FRF at a constant speed ratio, and TTFRFs were acquired at several speed ratios. A summary of all test conditions is given in Table 4.1.

Table 4.1: Test conditions

Hardware	Speed Ratios	Dynamic Torque (Nm)	Mean Torque (Nm)
A	0.2, 0.4, 0.6, 0.8, 0.9, 0.93, 0.95	20	75
B			
C			
D			

Torque was measured with PCB TorkDisk model 5308D-01A telemetry torque meters, while speed was measured using 150 pulses per revolution tone wheels with magnetic speed pickups. This instrumentation was co-located at the input and output of the torque converter test fixture as noted in callouts c and f in Figure 4.5.

4.4.2 Torque Transmissibility FRF Measurement

To acquire the TTFRF of the open TC over a range of speed ratios, time domain signals were acquired and processed into linear scaled autopower spectra. For a given measurement, three fundamental frequencies were present, and the peak values at these frequencies were picked off and used to compute the TTFRF at those specific frequencies (Figure 4.6).

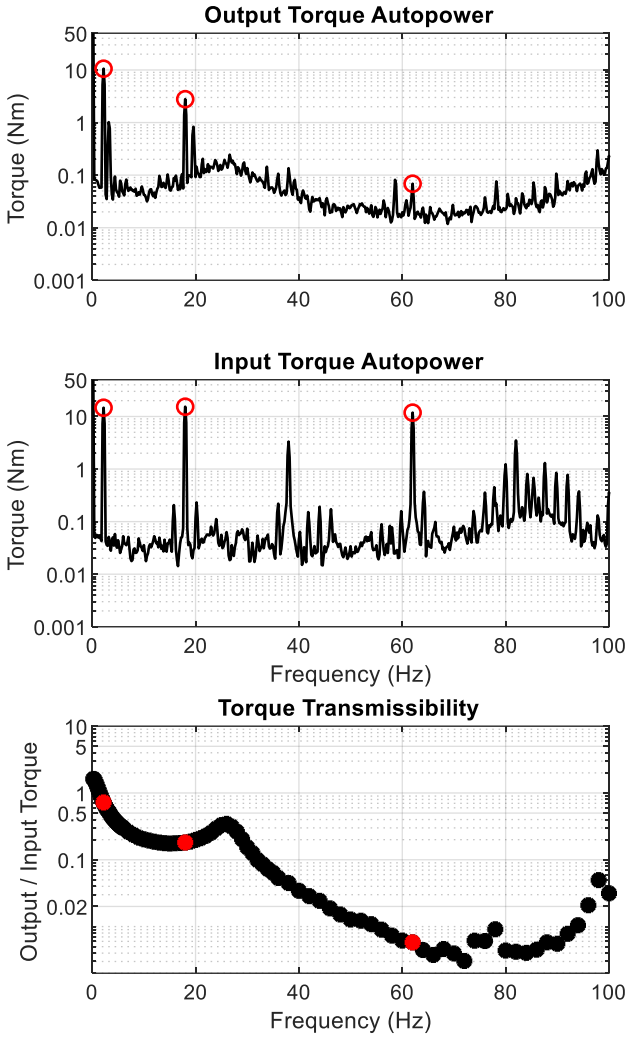

Figure 4.6:Time domain signals are converted to the frequency domain via FFT, and then the TTFRF is computed. Autopower spectra are shown to visualize the frequency content of excitation (2.2, 18, and 62 Hz).

The equation for the TTFRF is the ratio of the output torque and input torque auto powers (equation 4).

$$TTFRF = \frac{G_{yy}}{G_{xx}} \qquad 4)$$

Where G_{yy} represents the output torque autopower spectrum, and G_{xx} represents the input torque autopower spectrum.

The measurements contain frequency content besides the excitation frequencies. The input and output shafting have rotating imbalance which appears in the data. In Figure 4.6, first order corresponds to 17.9 Hz in the input torque (1074.6 rpm input shaft speed), and 3.3 Hz in the output torque data (200 rpm output shaft speed). In the input torque data, there is also evidence of lash being excited about 80 Hz; the input motor is coupled to the input shafting via a spline interface. It appears that all excitation signals get reflected about 50 Hz. The closer the signal is to 50 Hz, the more obvious this reflection. For example, the 62 Hz signal is reflected down to 38 Hz, and the 18 Hz signal reflected up to 82 Hz. While mysterious, this behavior did not impact the test results greatly, but would merit a separate investigation.

4.4.3 Simulated TTFRF of TC in Fixture:

A lumped parameter model of the torque converter dynamometer was previously developed, and its characterization described in Chapter 3 (Figure 4.7). The torque converter dynamometer (test setup) model includes the inertia of the torsional actuator, coupling inertias, absorbing dyno inertia, and shaft stiffness elements. Additionally, the absorbing dynamometer closed loop PID control on desired speed was included (far right in Figure 4.7) to account for a sub 1 Hz mode found previously during locked TCC testing (see Chapter 3).

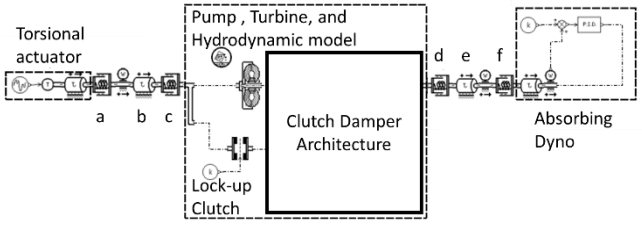

Figure 4.7: Model of test setup in Figure 3 (Top). Cross section view of a torque converter installed in the test fixture (bottom). a: Input u-joint shaft stiffness, b: input spindle inertia, c: input spindle stiffness, d: output spindle stiffness, e: output spindle inertia, f: output u-joint shaft stiffness

Lumped parameter models of the hydrodynamic torque converter were placed into the test setup model, and the TTFRF simulated. The torque converter models included clutch damper parameters of stiffness, damping and friction, pump, turbine and stator inertias, and a dynamic, physics based, torque converter sub-model. This sub-model contained the equations of motion of an open torque converter developed in [27]. This system of equations used the physical geometry of the torque converter to simulate the flow of ATF, and the transfer of torque from pump, to fluid, to turbine.

To demonstrate the expected contribution to the TTFRF of the torque converter sub-model, the TTFRF of the hydrodynamic torque converter model (Hardware B) was simulated without damper elements in the system, and greatly increased dynamometer coupling shaft stiffness values such that the dynamometer system dynamics were not

meaningfully present (Figure 4.8). As expected from previous works [26, 34], the open TC FRF looked like a low pass filter (LPF) in which the cutoff frequency and gain changed with SR.

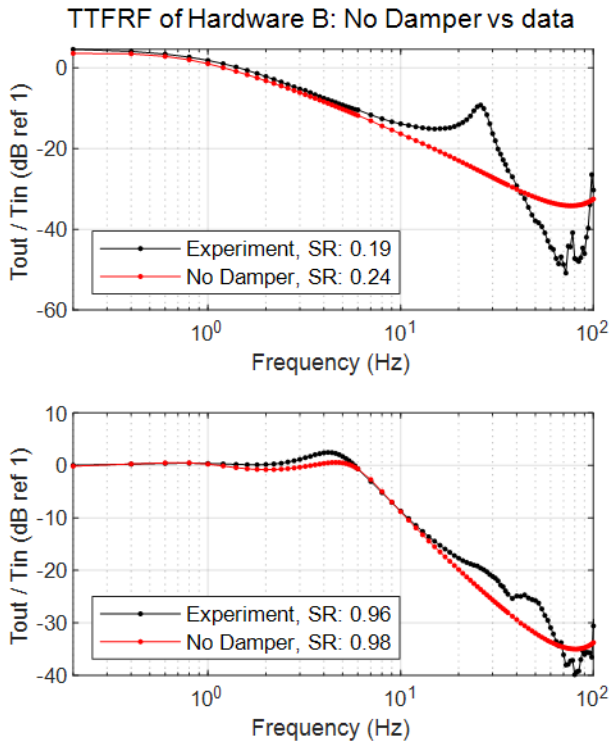

Figure 4.8: Simulated TTFRF of Hardware B without damper elements modelled, and stiffened dyno setup.

Using OEM provided values to populate the torque converter sub-model, a model of the entire torque converter architecture was built. A companion work focused on characterizing the clutch damper's stiffness and friction was instrumental in determining damper parameters. Figures 4.9-4.11 show the model architectures of the simulated hardware. In this work, hardware D was not simulated because specific design parameters of its turbine, stator, and pump blades were not available.

The damper models consist of spring, friction and end-stop elements. Together in parallel, these components are used to simulate the effective stiffness, friction, and range of motion of each set of springs within the damper mechanism. Each spring set in a clutch damper contains several springs in parallel in between consecutive plates. The spring sets come in many design configurations, and these specifics not important to the

scope of this study. The damper designs for hardware A and D contained one spring set, while hardware B and C contain two sets of springs in series.

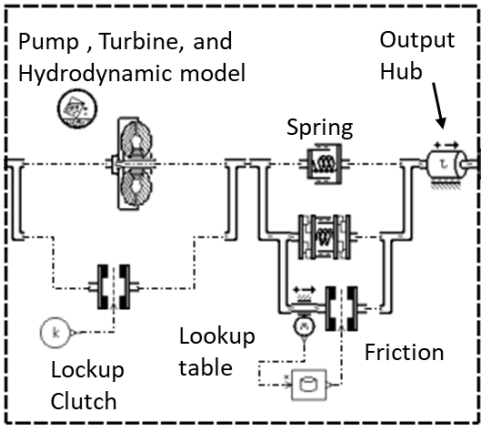

Figure 4.9: Hardware A torque converter model.

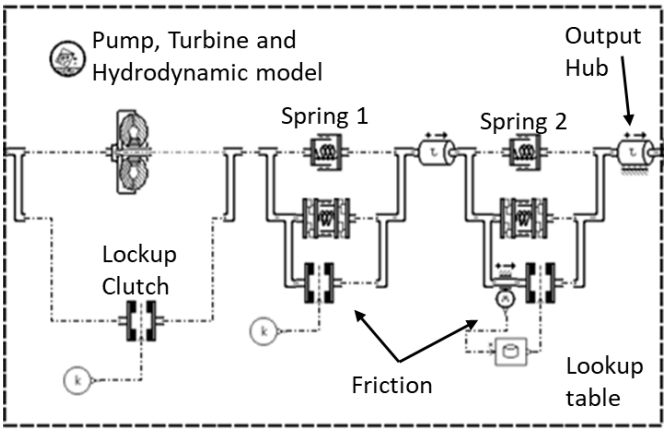

Figure 4.10: Hardware B and C torque converter model.

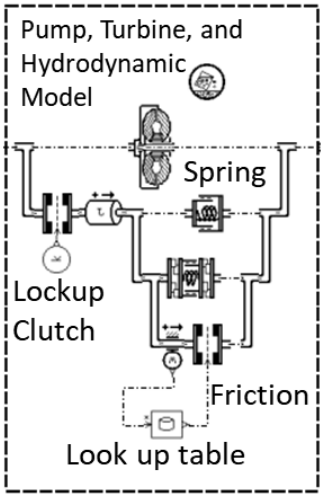

Figure 4.11: Hardware D torque converter model.

To simulate the TTFRF, the same multi-sine tone input torque was generated, and the simulated time domain signals are processed using the same method as with the experimental TTFRF. Input and output torque signals are ‘measured’ at inertias c and f in the test cell model (Figure 4.7) which corresponds to the torque sensor locations.

4.4.4 Understanding System Modes

The test setup has two measurement degrees of freedom (input torque/speed and output torque/speed), so at most, the first torsion mode of the test setup could be experimentally characterized. When measuring and simulating the TTFRF over the 0-100 Hz range, other resonances were present besides the first torsion mode of the TC (Figure 4.12). More measurement DOFs would be needed to measure the other system mode shapes that contributed to the system’s response. Torque sensors and tone wheels located at the input and output motor couplings would achieve improved spatial resolution, but more instrumentation was not readily available. Instead, a model of the test setup predicted motion at unmeasured DOFs, and more complicated modes shapes were estimated.

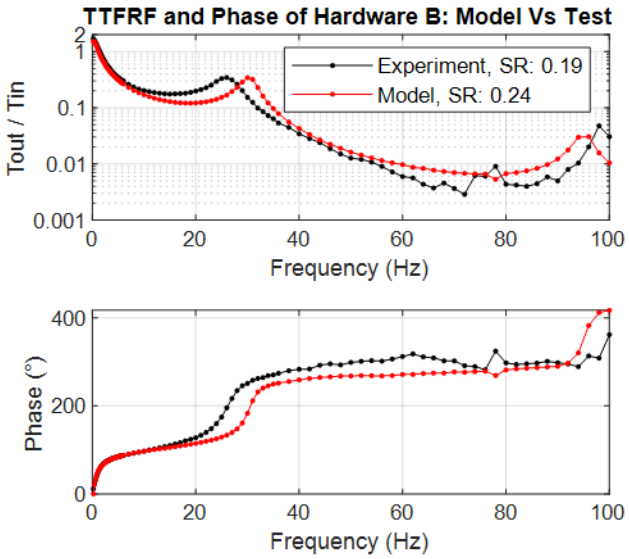

Figure 4.12. TTFRF from test and model. Both test and model results contain the same resonances, so the model derived mode shapes are valid.

The model predicted three mode shapes in the 0-100Hz range for hardware B (Figure 4.13). In the TTFRFs in **Error! Reference source not found.**, two modes were present (30 Hz and 95 Hz), but not the third system mode (at 89 Hz). The mode shape for the 89 Hz mode, an input shaft torsion mode, did not contain any obvious TC hardware or output shaft motion and was not expected to influence the TTFRF. The other modes (featured in the TTFRF) were a damper mode at 30 Hz and an output shaft torsion mode. It was assumed that the same system modes were present for the other TC hardware, only at slightly different frequencies due to torque converter inertia and stiffness changes.

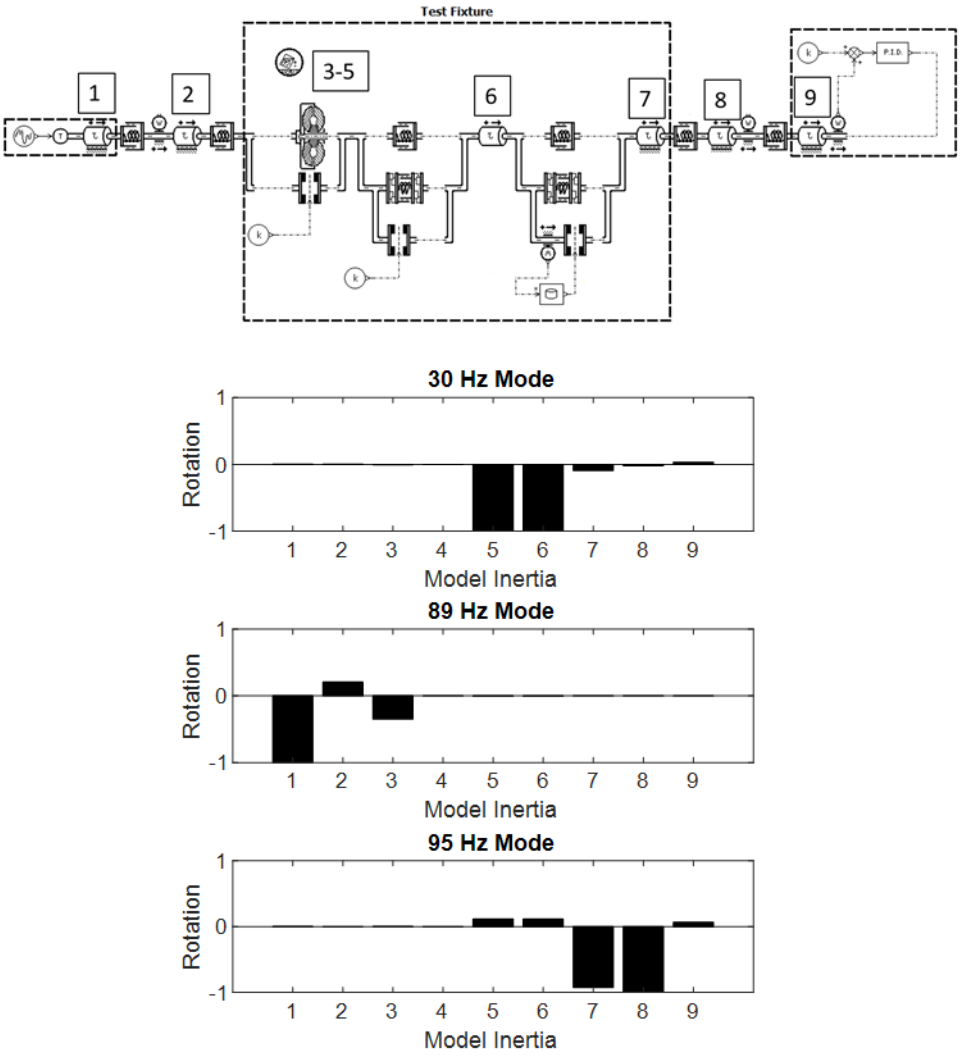

Figure 4.13: Mode shapes generated from the model of the test setup with hardware B. 1) torsional actuator; 2) input spindle; 3) pump; 4) stator; 5) turbine; 6) intermediate plate; 7) output hub; 8) output spindle; 9) absorbing dyno

4.5 Initial Test and Model Results

4.5.1 Summary

The measured TTFRFs showed torque converter and test setup dynamics, but the torque converter specific dynamics were well separated from the other system resonances. The open TC behaved like a LFP, passing low frequency torsional inputs and attenuating them beyond the cutoff frequency. Resonances exist beyond the cutoff frequency because significant torsional excitation existed to excite a damper mode—only in the TD

architectures—and an output shaft torsion mode. The features that pertain to the torque converter are the damper mode (which typically shows up around 25 Hz) and the LPF performance. The LPF performance was described with its cutoff frequency.

A spike corresponding to first order with respect to the output shaft speed was evident in some of the TTFRFs. This is a result of first order vibration acting as an uncorrelated input in the TTFRF measurement. The spike was more prominent when the input motor introduced a torsional coinciding with first order and when the measured response was small relative to first order. The TTFRF amplitude was over estimated when these conditions were present because the autopower spectrum combines both the torsional excitation and the first order imbalance. This error was accepted because the first order imbalance was not easily separated from the measurement.

4.5.2 Torque converter hardware: A

Hardware A contained a single stage TD and had the highest K factor of all other tested hardware. When operating at low speed ratios (0.2-0.8), the torque converter multiplied torque in the 0.2 – 1 Hz range, and the cutoff frequency (corresponding to -3dB) of the LPF was at 1.6 Hz. As the speed ratio transitioned from 0.8 to 0.93, the torque multiplication went to 0 dB and the cutoff frequency of the LPF began to increase—see 1750rpm TTFRF in Figure 4.14. The cutoff frequency of the TC stabilized at 4.6 Hz once operating beyond coupling point. The speed at which Hardware A transitioned across coupling point was higher than the other TCs hardware because of its high K factor. For a given pump torque, a higher K factor TC rotates at a higher pump speed (see equation 3).

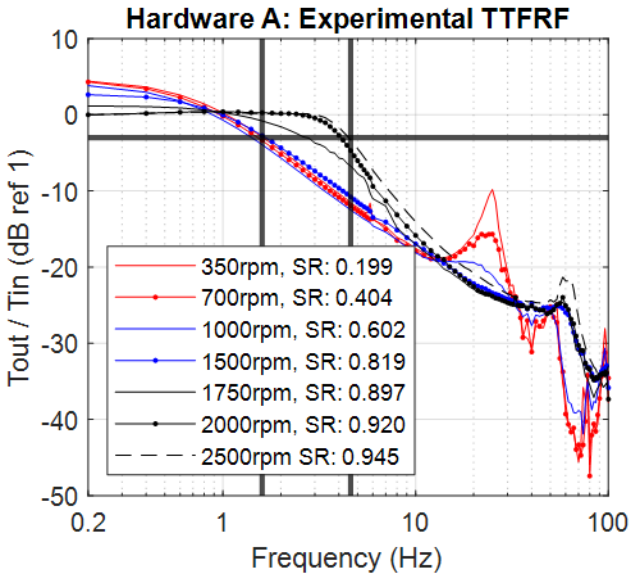

Figure 4.14. TTFRF of Hardware A over a range of speed ratios. Cursors located at cutoff frequency of open torque converter at extreme high and low speed ratios (1.6 and 4.6 Hz respectively).

The damper mode at ~25 Hz was present at low speed ratios, and the TTFRFs showed that enough torsional vibration amplitude was transmitted across the open TC to excite this mode of vibration. As the mean turbine speed increased, the damper mode amplitude decreased, and eventually disappeared from the TTFRF (at SR: 0.819 and beyond). As discussed in a companion work about locked clutch dynamics (Chapter 3), the friction torque in the damper increases as a function of rotational speed—due to centrifugal loading on the springs in their cages. So, as the mean turbine speed increased, the friction torque became large enough to eliminate the damper mode from the TTFRF. The speed dependent friction lookup tables in the damper model (Figure 4.9) were tuned to achieve the same amplitude TTFRF at the damper resonance.

Next, the TTFRF of hardware A was simulated and compared to the experimental TTFRFs to validate the torque converter model (Figure 4.15). The model results at extreme high and low speed ratio are shown for brevity. At the lowest turbine speed (350rpm), the model predicted the same speed ratio as the experiment. The simulated TTFRF correlated well with the experimental TTFRF in the 0-10 Hz range, and the natural frequency of the damper mode was 2 Hz higher in the simulated TTFRF (25 and 27 Hz for test and model respectively). This frequency error was investigated further in the next section. The low speed ratio test data also showed a second mode at 54 Hz and a third mode at 96 Hz. The model reproduced the 96 Hz mode, a torsion mode of the output spindle and output u-joint shaft, but not the 54 Hz mode.

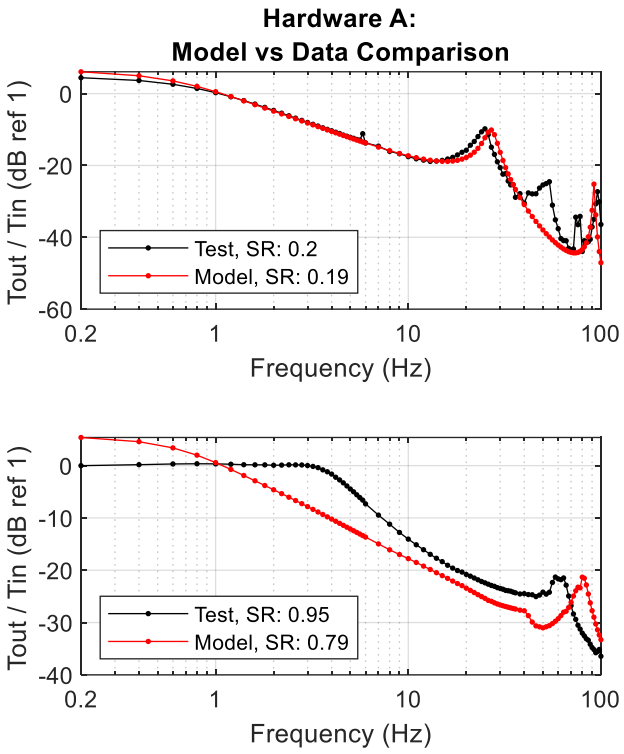

Figure 4.15: Simulated TTFRF and experimental TTFRF. Low speed ratio (top), and high speed ratio (bottom). Note: spike at 5.8 Hz (top) due to rotating imbalance on output shaft.

At the highest turbine speed (2500 rpm), the model did not predict the same speed ratio as the test. Thus, the simulated TTFRF had much more amplification near 0 Hz than the experiment, the cutoff frequency was much lower (like the low speed ratio results), and there was a large frequency mismatch in the output shaft torsion mode. Further investigation into these features was warranted, and are discussed further in the next section.

4.5.3 Hardware B

Hardware B contained a two stage TD, and had the lowest K factor—along with hardware D. When operating at low speed ratios (0.2-0.8), hardware B amplified torque in the 0.2 – 1 Hz range, and had a cutoff frequency at 2.2 Hz. As the speed ratio transitioned from 0.8 to 0.95, the TTFRF became flat in the 0.2-3 Hz range and the cutoff frequency of the LPF began to increase—see 1000rpm TTFRF in Figure 4.16. Hardware B transitioned across coupling point at lower turbine speed than hardware A because of its lower K factor. A new feature not obvious in the hardware A TTFRFs, was a low frequency a peak just before the cutoff frequency, when operating at high speed ratios. This low frequency peak may be an artifact of the hydrodynamics of the torque converter, and may be more pronounced in lower K factor TCs. The amplification of the peak is low

(between 1 and 2), and the torque converter otherwise appears to behave as a LPF. Beyond coupling point, the LPF of the torque converter stabilized at a new cutoff frequency of 7 Hz.

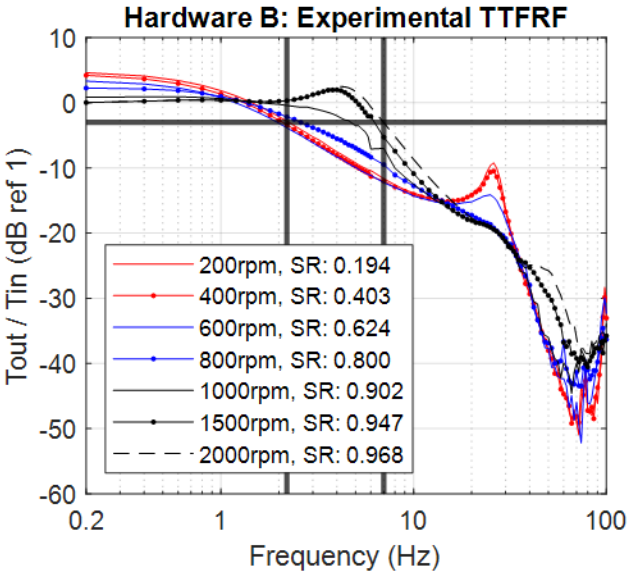

Figure 4.16: TTFRF of Hardware B over a range of speed ratios. Cursors located at cutoff frequency of open torque converter at extreme high and low speed ratios (2.2 and 7 Hz respectively).

The damper mode showed up at 27 Hz, and as the mean turbine speed increased, the amplitude of this mode decreased, and eventually disappeared from the TTFRF (at SR: 0.8 and beyond). As discussed with hardware A, the friction torque in the damper increased with rotational speed, and eventually eliminated the damper mode from the TTFRF. These low speed ratio TTFRFs were used to characterize the speed dependent friction lookup table in the damper model (Figure 4.10).

Next, the TTFRF of hardware B was simulated and compared to the experimental TTFRFs to validate the torque converter model (Figure 4.17). The model accurately predicted the speed ratio for the applied loads at both the high and low speed ratio operating condition, and the damper mode was also well represented. As with hardware A, the natural frequency of the damper mode was higher in the simulation than the experiment—26 Hz in the experiment and 30 Hz in the simulation. This frequency error was investigated further in the next section. The test data also showed a second mode at 96 Hz, which was reproduced by the simulation. As with hardware A, this 96 Hz mode was a torsion mode of the output spindle and output u-joint shaft.

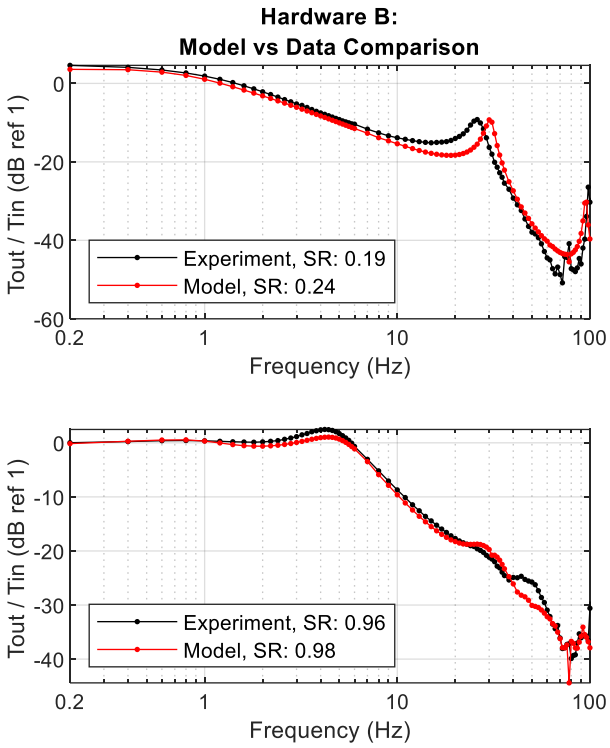

Figure 4.17: Simulated TTFRF and experimental TTFRF. Low speed ratio (top), and high speed ratio (bottom).

4.5.4 Hardware C

Hardware C contained the same damper hardware and diameter as Hardware B and only differed in K factor (difference of 50). The difference in K-factor is achieved through blade geometry changes within the pump, turbine and stator elements. The TTFRF was measured at several speed ratios to understand how the torque converter system changed with speed ratio (Figure 4.18). When operating at low speed ratios (0.2-0.9), the torque converter multiplied torque in the 0.2 – 1 Hz range, and had a cutoff frequency at 1.6 Hz. As the speed ratio transitioned from 0.9 to 0.94, the TTFRF flattened and the cutoff frequency changed to 4.6 Hz.

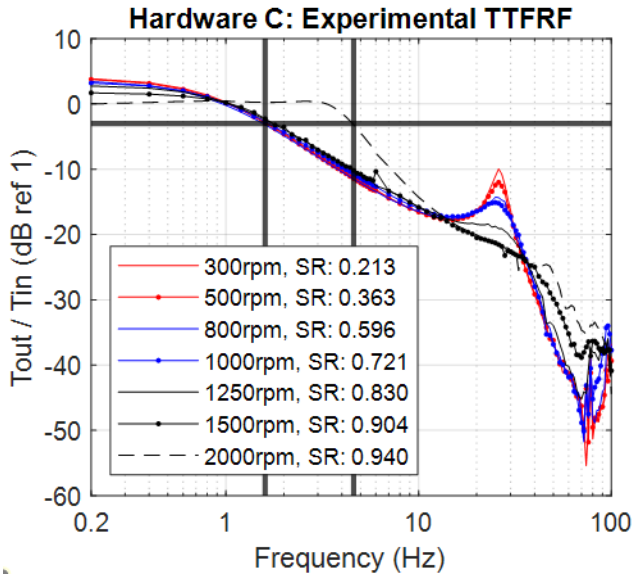

Figure 4.18: TTFRF of Hardware C over a range of speed ratios. Cursors located at cutoff frequency of open torque converter at extreme high and low speed ratios (1.6 and 4.6 Hz respectively).

Like hardware A and B, the damper mode (at 26 Hz) appeared at low speed ratios. This mode was at the same frequency as hardware B because of the identical damper design. Again, the TTFRFs from 0.2-0.8 SR were used to tune the speed dependent friction lookup table in the damper model (Figure 4.10).

To validate the TC model of hardware C, the simulated TTFRFs were compared to experimental TTFRFs (Figure 4.19). The model predicted the operating speed ratio accurately at both high and low turbine speeds, but over predicted the damper mode natural frequency (30 Hz in model and 26 Hz in test). At low speed ratio, the model accurately predicted the TTFRF—except for the damper mode error. For the high speed ratio comparison, the simulated TTFRF did not have the same flatness or cutoff frequency as the experiment. The damper mode error and high speed ratio TTFRF difference was discussed further in the next section.

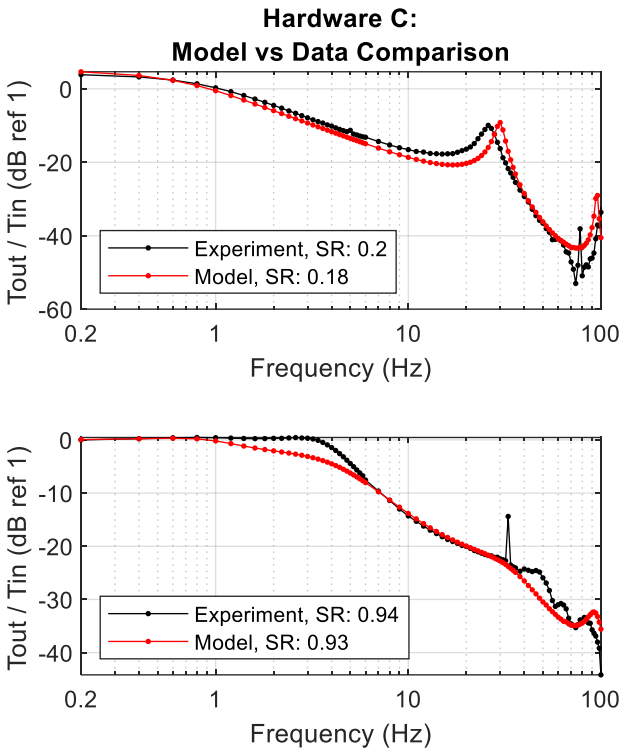

Figure 4.19: Simulated TTFRF and experimental TTFRF. Low speed ratio (top), and high speed ratio (bottom). Note: spike at 33 Hz (bottom) due to rotating imbalance on the output shaft (2000 rpm).

4.5.5 Hardware D

Hardware D had a conventional damper architecture, and a similar K factor to Hardware B. The TTFRFs at several speed ratios were measured (Figure 4.20). At speed ratios ranging from 0.2-0.7, the TTFRF displays torque multiplication from 0.2-1 Hz, and decays like a LPF beyond a cutoff frequency at 1.6 Hz. As the TTFRF transitioned to higher speed ratios, the cutoff frequency increased to 3.8 Hz. Beyond the respective cutoff frequencies, the TTFRF decays over the rest of the tested frequency band. The damper mechanism in the CD architecture was positioned in parallel with the pump and turbine, and when operating with the clutch open, all of the applied torque flowed through the transmission fluid. Thus, the damper mode was not expected to be excited, and the experimental TTFRFs confirmed this hypothesis. The TTFRF of hardware D was not simulated since the blade design parameters required by the TC model were not available. The test data acquired on hardware D confirmed that the damper mode was unique to the turbine damper architecture.

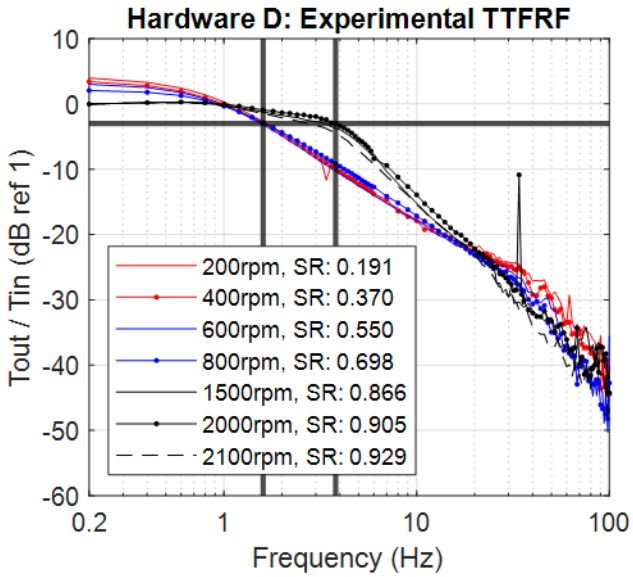

Figure 4.20: TTFRF of Hardware D over a range of speed ratios. Cursors located at cutoff frequency of open torque converter at extreme high and low speed ratios (1.6 and 3.8 Hz respectively). Note: spike at 33 Hz due to rotating imbalance of the output shaft.

4.6 Discussion

4.6.1 Hardware Comparison

The TTFRFs, at 0.2 and 0.92 speed ratio, of all torque converter hardware are overlaid (Figure 4.21) to discuss the influence K factor and damper architecture have on the TTFRF. Recall that the K factor of the tested hardware in ascending order is: Kb, Kd, Kc, and Ka (Refer back to Figure 4.2). Now, looking at both TTFRF plots in Figure 4.21, as K factor increases, both the cutoff frequency and amplification decrease. Regarding the influence of damper architecture on the TTFRF, it is clear at low speed ratios that the turbine damper architectures display a damper resonance in the TTFRF. As expected, this resonance is not present in the TTFRF of the conventional damper architecture (Hardware D). In the TD architecture, the applied torque always passes through the damper springs, but in the CD architecture, the applied torque only passes through the damper springs when the lockup clutch is engaged. At 0.92 speed ratio, the TTFRFs of the TD torque converters are flat and as K factor increases, display a peak before decaying. Conversely, the TTFRF of the CD torque converter (hardware D) begins to decay earlier than all of the TD hardware. Interestingly, the K factor curve of hardware D also starts increasing at an earlier speed ratio than the other three hardware. This characteristic could explain the difference in cutoff frequency between hardware B and D, who have the same K factor at low speed ratios, but different K factors at high speed ratios (refer back to Figure 4.2). There is no clear influence of torque converter diameter on the TTFRFs.

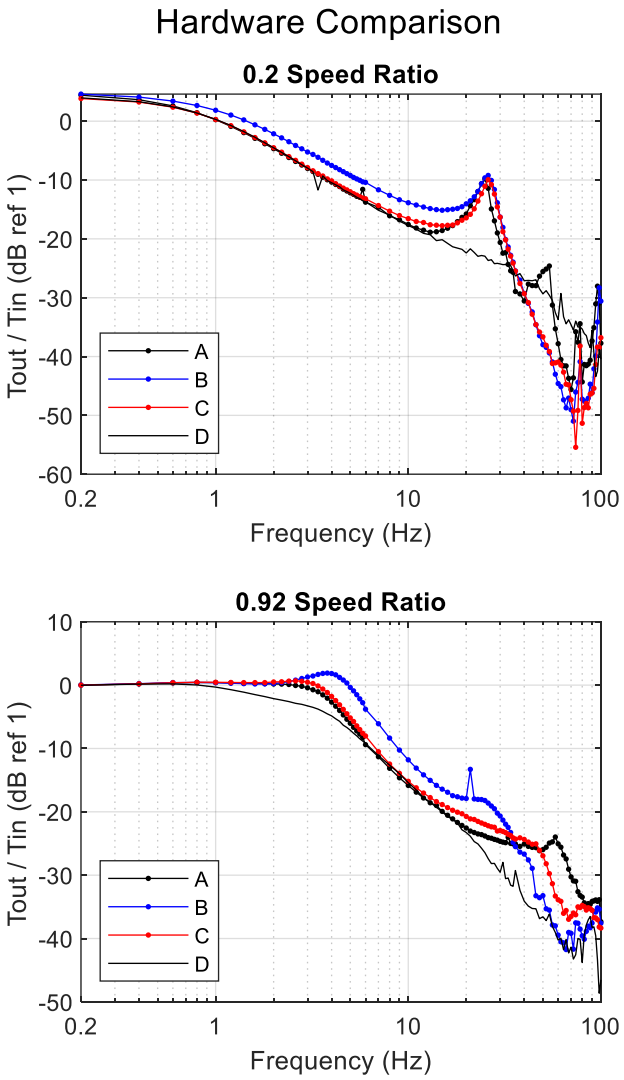

Figure 4.21: Overlaid TTFRFs of all torque converter hardware at 0.2 speed ratio (top) and 0.92 speed ratio (bottom).

4.6.2 Dynamic Torque Converter Sub-Model Discussion

The open TC dynamics dominate the TTFRFs in the 0-10 Hz range, and the downstream system dynamics dominate beyond 10 Hz. For hardware B, the TC dynamic model accurately predicted the speed ratio for a given input torque and output speed load condition. For models hardware A & C, the low speed ratios correlated well, but with increased turbine speed, the predicted speed ratio had more error than with hardware B. Inaccuracy in the TC sub-model parameters would cause error in the predicted speed ratio, and the experimental TTFRFs could be used to reverse engineer the TC blade parameters. Since the blade parameters used to simulate hardware B achieved less than

15% error between test and model (in the 0-10 Hz range), it is concluded that the TC sub-model is valid in the low frequency range. The right set of TC blade parameters used in the TC sub-model, can achieve low percent error between experimental and simulated TTFRFs. The blade parameters used in the models of hardware A and C need further investigation to improve correlation and reduce speed ratio error at the higher turbine speeds.

4.6.3 Damper Mode Discussion

In the TTFRFs of all TD hardware (A-C), the natural frequency of the damper resonance obtained from the simulations is consistently higher than in the experimental TTFRF. This brings to question the accuracy of the damper stiffness, and TC inertias. In prior research, the damper model parameters were verified with experimental TTFRFs that were acquired with the lock-up clutch engaged. Thus, the equivalent stiffness of the damper and the TC inertias are well known, and not the source of the natural frequency error. Given that the TC sub-model parameters dictate the low frequency performance, and the damper parameters control the damper mode's natural frequency, it seems that there is some inertial coupling between the ATF and turbine when operating in open mode. This could explain the natural frequency error between the model and the experimental data.

When switching torque converter operation from locked to open, the system changes fundamentally. In locked mode, all torque is transmitted through the clutch springs, and the ATF inside of the TC rotates with the pump, turbine, and stator as one. In locked clutch simulations, the inertia of the ATF is lumped into the turbine and pump. When in open mode, torque is transmitted from the pump, to the ATF, and finally to the turbine. Below coupling point, the stator remains fixed to facilitate torque multiplication. In open mode, the ATF no longer rotates with the turbine or pump elements, and experiences toroidal flow. The mass flow rate of ATF across the pump-turbine interface changes with speed ratio (Figure 4.22). As speed ratio increases, the toroidal flow drops off significantly.

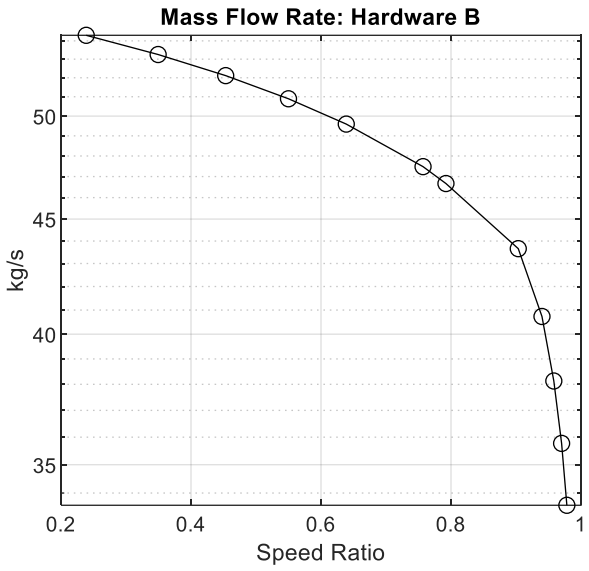

Figure 4.22: Mass flow rate of ATF in toroidal flow predicted from the physics based TC sub-model of Hardware B.

The values for the lumped pump and turbine inertias already contain the inertia of the ATF contained within each respective volume. But, since the ATF moves relative to the pump, turbine and stator, it is then suggested that the apparent ATF inertia in the turbine appears larger. While the equations of motion of the TC model account for the ATF, turbine, stator, and pump inertias, it appears that the reflected inertia effect was ignored.

Assuming the hypothesis about reflected inertia was correct, a constant amount of inertia is added to the turbine such that the natural frequency of the simulated TTFRF matched the experimental TTFRF (Figure 4.23). By adding 0.015 kg*m^2 to the turbine inertia, the natural frequency of the damper mode matched the experiment at speed ratios below 0.9. This crudely simulates the reflected inertia when operating at low speed ratios, and the value of 0.015 kg*m^2 arrived at via a guess and check method. The additional inertia (0.015 kg*m^2) is on the same order of magnitude as the turbine inertia itself, so more proof is needed to justify this change. A new derivation of the system of equations is needed to confirm the hypothesis about reflected ATF inertia.

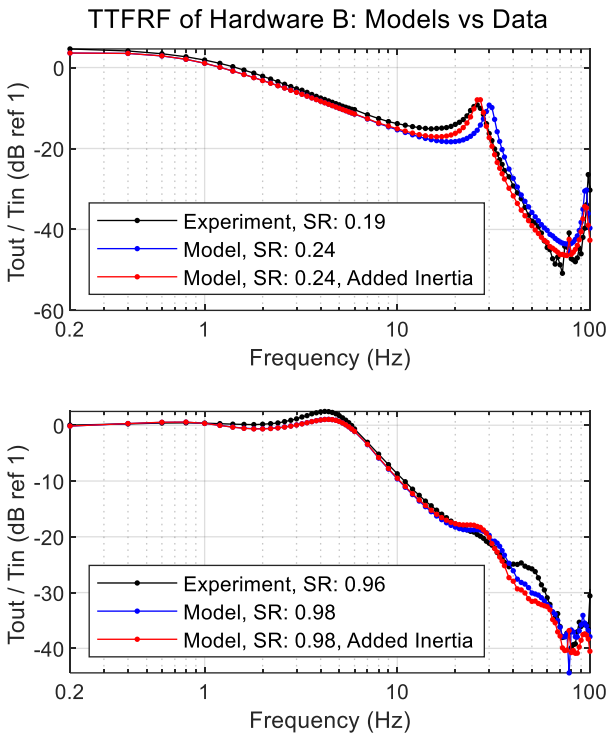

Figure 4.23: TTFRF of TC model with additional stiffness and added inertias.

4.7 Conclusions

Torque transmissibility frequency response functions of four different torque converter designs—isolated from other powertrain components—were measured and simulated over a range of speed ratios. The experimental results showed that with increasing K factor came a decrease in cutoff frequency and a reduction in amplification at frequencies below cutoff. While there was no clear influence of torque converter diameter on the measurements in this study, a clear difference between torque converter damper architecture was shown. At low speed ratios, the damper resonance appeared for turbine damper architectures, and not appear for the conventional damper hardware. This indicates that a torque converter operating in open mode transmits enough torsional vibration to excite downstream modes.

In the model space, less than 15% error between model and test TTFRFs was achieved with hardware B (in the 0-10 Hz range). This demonstrates that the hydrodynamic torque converter model contains the proper dynamics to replicate test data in the low frequency range. However, error in the damper mode's natural frequency (25-30 Hz range) was manifested, and it was speculated that the inertia of the working fluid, in toroidal flow, appears larger at the turbomachine elements. To resolve the natural frequency error, analytical proof of the reflected inertia hypothesis is needed.

5 In Situ Torque Transmissibility Frequency Response Function Measurements of a Centrifugal Pendulum Vibration Absorber in a Torque Converter Clutch Damper

Luke Jurmu[a], Darrell Robinette[a], Jason Blough[a], Craig Reynolds[b]

[a]Department of Mechanical Engineering
Michigan Technological University
1400 Townsend Dr, Houghton, MI 49931, USA
lukejurmu@hotmail.com
dlrobine@mtu.edu
jrblough@mtu.edu

[b]General Motors Company
P.O. BOX 33170
Detroit, MI 48232-5170, USA
craig.a.reynolds@gm.com

Corresponding author: Luke Jurmu

5.1 Background

In Chapter 3, one of the torque converter dampers characterized contained a CPA. This initial round of test results triggered further questions about CPA losses. Since damper friction was expected to influence CPA performance, and damper springs heavily attenuated torsional inputs prior to the CPA, characterization of the CPA without damper effects was desired. Custom torque converter hardware was acquired such that the damper springs were pinned and the CPA remained active. In this way, in situ characterization of a CPA was carried out while operating in a torque converter without influence of damper springs.

5.2 Abstract

In previous research involving the characterization of a torque converter clutch damper with a centrifugal pendulum absorber, it was suggested to characterize customized hardware to isolate the damper dynamics from the CPA dynamics. Correlating complicated models to experimental data involves many model parameters resulting in little confidence in the model's accuracy. Four iterations of the same torque converter design were characterized in a unique torque converter dynamometer in order to gain confidence in the estimated parameters, and this also led to simplification of the parameter estimation process. Both a manual tuning and a half-power bandwidth method were used in estimating the equivalent viscous damping of the CPA mechanism. The estimated damping values were validated with the test data acquired from all hardware iterations. This improved the correlation between the unmodified torque converter and

test data, providing confidence in the new CPA damping values. Simulation of the torque transmissibility frequency response function of the CPA demonstrated that the tuning order did not match the excitation order of maximum pendulum displacement. However, relative phase between input and output signals for both speed and torque were good predictors of maximum displacement.

5.3 Introduction

Sarazin invented the Centrifugal Pendulum Absorber (CPA) in 1937 [35] to attenuate torsional vibrations in reciprocating engines and have become a staple in modern automobile drivetrains. The CPA is a vibration absorber device that operates on the principle of a simple pendulum, in which the restoring force is due to gravity. A pendulum's restoring force becomes the centrifugal force when mounted on a rotating disc. As a result, the natural frequency of the CPA depends on the rotating velocity of the disc. Thus, the CPA can be tuned to have a natural frequency matching the firing frequency of an internal combustion engine (ICE). The CPA has been shown to be very robust at attenuating torsional vibrations coming from the engine [2, 36]. CPA research covers pendulum path design, CPA instabilities, and a limited number of experimental characterization.

CPA design has increased in complexity in recent years with particular interest placed in the path design of the pendulum masses [38-40, 42]. Tautochronic CPA paths ([39, 40]) have the useful property of maintaining constant tuning order independent of pendulum deflection amplitude, and include cycloids and epicycloids [41]. Besides pendulum path design, methods of pendulum suspension are covered in [42]. Automotive applications typically use parallel and trapezoidal bifilar pendulums. Automotive CPAs feature multiple absorbers on a given disc, and managing instabilities associated with multiple absorbers has also been researched [37].

Significant efforts in modelling CPAs to include friction and damping effects [44, 45] has been completed along with important experimental investigations. Some experimental works consist of isolated CPAs in special test rig [43], while other research measured the torque transmissibility frequency response function (TTFRF) of a CPA in a torque converter using a special torque converter test setup [46].

Currently, not many studies featuring the frequency response function (FRF) of a CPA have been published. A unique test rig for measuring the CPA FRF (pendulum angle / input torque) was developed [43], and a ring down test of the CPA executed while spinning. The ring down test results characterized both friction and viscous damping of the CPA mechanism [44]. While these studies featured a special CPA unique to the test rig, other research investigates automotive specific CPA hardware. One study characterized friction of an automotive CPA with the rotor fixed and pendulum motion measured [45]. Most similar to this research, a spinning torque converter test setup was used to measure the torque transmissibility frequency response function (TTFRF) of a CPA in a torque converter clutch (TCC) damper [46]. This research didn't measure

TTFRFs at several operating speeds, or estimate CPA friction or damping. In this article, equivalent viscous damping of an automotive CPA, submerged in ATF, in a TCC damper is quantified at several operating speeds. Custom torque converter hardware, with the damper mechanism pinned from motion, made it feasible to accurately quantify damping. Friction effects of the damper mechanism were effectively eliminated from the system.

Along with the unmodified CPA hardware, torque converters with the straight spring set pinned, damper pinned, and CPA pinned were tested over a range of speeds and dynamic torque input amplitudes (Figure 5.1). Figure 5.2 shows the physical location of key torque converter and clutch damper components, and depicts which damper components are fixed in each custom hardware configuration.

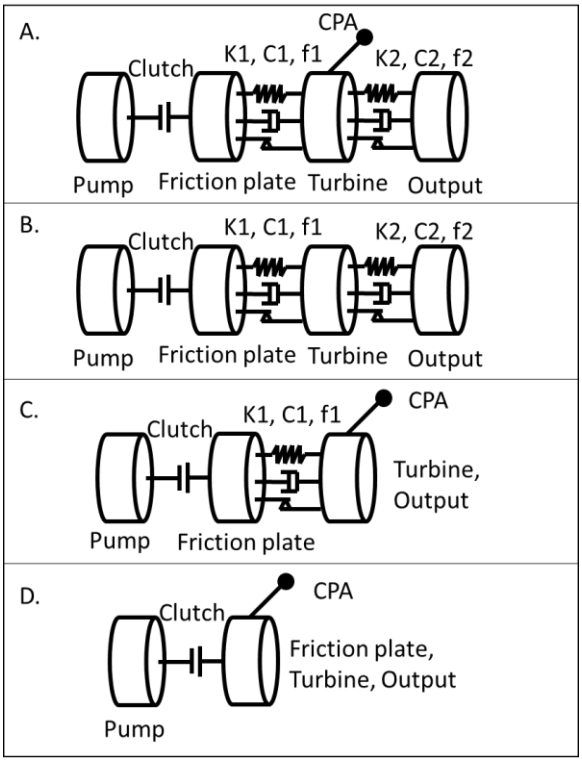

Figure 5.1: Schematics of the four hardware iterations that were tested. A) Unmodified hardware. B) Pinned CPA. C) Pinned straight spring. D) Pinned damper.

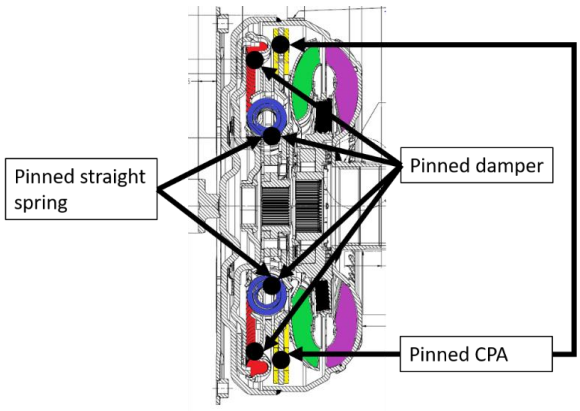

Figure 5.2: Cross section view of the torque converter under investigation. Arrows indicate which components were fixed from relative motion in each hardware iteration. Key components are colored. Red; arc spring, Blue; straight spring, Yellow; CPA, Green; turbine, Purple; pump, Black; stator.

Two methods were used to estimate the equivalent viscous damping coefficients from the measured TTFRFs of the pinned damper hardware. The first method uses the damping ratio of the CPA anti-resonance at the tuning order. The second method manually tuned damping to get the simulated TTFRF to match the test result. The TTFRFs from the other custom torque converters validate the newly estimated damping coefficients and in estimating the friction parameters of the damper itself.

5.4 Methods

5.4.1 CPA Test Setup and Methods

The test cell (Figure 5.3), measurement method, and signal processing utilized for characterization of the array of CPA hardware were previously described in other works [11, 62, 76]. Those methods were modified slightly to suit the specific hardware being tested, but the concept remained the same. The torsional actuator applied a torque with sinusoidal inputs as described by equation 1.

$$T_{tot} = T_m + T_a \sin(2\pi f_1 t + \phi_1) + T_a \sin(2\pi f_2 t + \phi_2) \ldots \qquad 1)$$

Where Tm and Ta refer to the mean and dynamic torque respectively. The absorbing dyno applied a reaction torque such that its rotational velocity remained constant. The sine tones were constant for the duration of each measurement, and several measurements were made to acquire the entire frequency range. Equation 1 demonstrates that any number of sine tones could be added to the input torque signal. This study used both tri-tone and single-tone excitations to capture the TTFRF. The tri-tone excitation was deployed to acquire a TTFRF over the 0-100 Hz frequency range and effectively measures all system dynamics. The single-tone excitation was deployed to acquire the TTFRF about narrow bands of interest. In this case the 2nd order firing frequency was the main concern as it was the CPA tuning order.

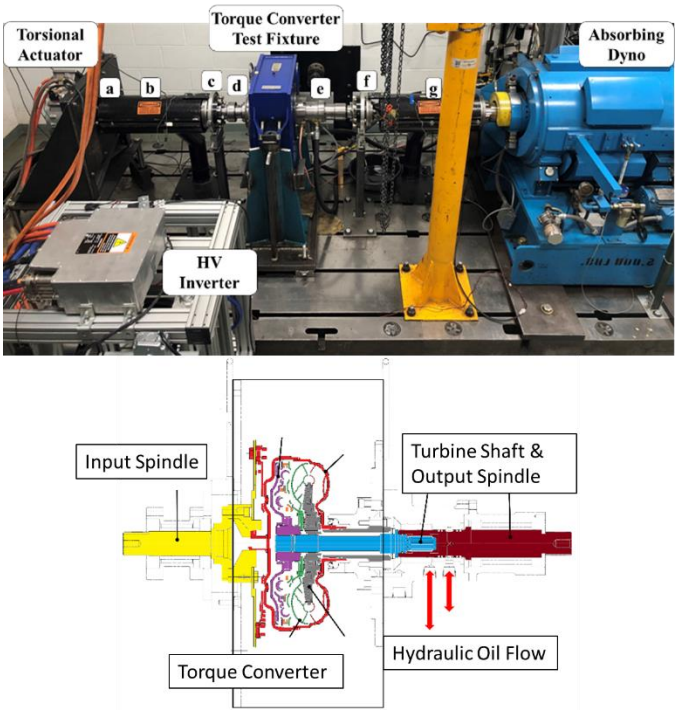

Figure 5.3: Test setup used for measuring torque transmissibility of the custom CPA hardware (Top). Cross section view of the torque converter in the fixture (bottom). a: input coupling inertia, b: Input u-joint shaft stiffness, c: input spindle inertia, d: input spindle stiffness, e: output spindle stiffness, f: output spindle inertia, g: output u-joint shaft stiffness

Testing the array of CPA torque converters covered a broad range of operating conditions (Table 5.1). A range of dynamic torque amplitudes and speeds were tested to achieve varying displacement levels of the pendulum and to characterize speed dependencies, respectively.

Table 5.1: Test conditions

Hardware Designation	Speeds (rpm)	Dynamic Torque (Nm)	Mean Torque (Nm)
A: Unmodified	600, 900, 1200, 1500, 1800, 2100	5, 10, 15, 20, 30, 40, 50, 75, 100, 120	150
B: Pinned CPA			
C: Pinned straight spring			
D: Pinned damper			

The input and output torques were measured using PCB TorkDisk model 5308D-01A telemetry torque meters, and speed was measured with magnetic pickups in conjunction

with 150 tooth tone wheels. The torque meters and tone wheels were co-located at the input and output of the test fixture (c and f in Figure 5.3).

5.4.2 Torque Transmissibility FRF

The TTFRF was acquired with a sine dwell method—using individual sine tones and three sine tones. Time domain signals were acquired and processed into autopower spectra. Depending on the excitation scheme (single tone or tri tone), one or three frequencies corresponding to excitation frequency were present. The respective measured amplitudes at these frequencies were used to compile a TTFRF (Figure 5.4). The equation for the TTFRF is the ratio of the output torque and input torque auto powers (equation 1).

$$TTFRF = \frac{G_{yy}}{G_{xx}} \qquad 1)$$

Where G_{yy} represents the output torque autopower spectrum, and G_{xx} represents the input torque autopower spectrum.

As shown in the autopower spectra in Figure 5.4 other frequency content was present in the measurements: a peak at 30 Hz and a peak at 40 Hz. The peak at 30 Hz coincides with first order, while the 40 Hz peak appears to be a reflection of the 60 Hz excitation about 50 Hz. This phenomenon was observed in all other measurements, and the cause is unknown. This behavior did not impact the TTFRF results and was ignored for the purpose of this investigation. The TTFRF results were plotted with respect to the order rather than frequency so the tuning order could be readily observed. The TTFRFs were plotted vs frequency in the measurements concerning the overall system dynamics.

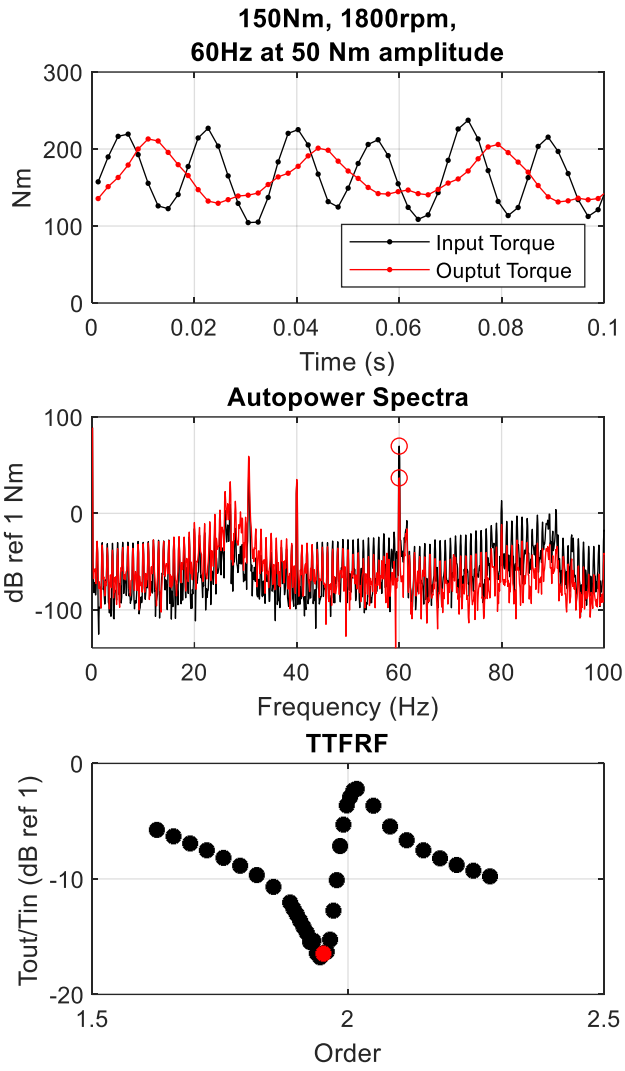

Figure 5.4:Time domain signals (top) are converted to the frequency domain via FFT, and then the TTFRF (bottom) is computed as the ratio of autopower spectra. Autopower spectra (middle) are shown to visualize the frequency content of excitation (60 Hz).

5.4.3 Estimating CPA damping:

The equivalent viscous damping coefficient was estimated from the measured TTFRFs of the pinned damper hardware using the half power bandwidth method. Typically, the half power bandwidth method is applied to a resonant peak of an FRF, but the pendulum resonance was not directly measured in the CPA. Assuming that the shape of the CPA anti-resonance in the TTFRF would be representative of the pendulum resonance, f_0 was selected as the minimum value of the TTFRF at the anti-resonance for computing

damping ratio (Figure 5.5). Equation 2 shows the equation for computing damping ratio of a resonance.

$$\zeta = \frac{1}{2Q} = \frac{f_2 - f_1}{2f_0} \qquad 2)$$

Then, f2 and f1 were selected 3 dB up in amplitude from the minimum at f0.

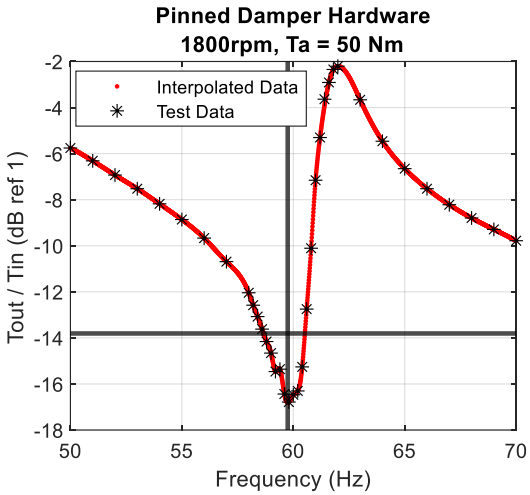

Figure 5.5: Half power bandwidth method applied to the TTFRF of the pinned damper hardware.

The dynamics of the CPA must be understood to estimate a viscous damping coefficient from the damping ratio. A simple approximation of the physical CPA hardware was used to equate damping ratio with equivalent damping. The simple CPA model is shown in Figure 5.6.

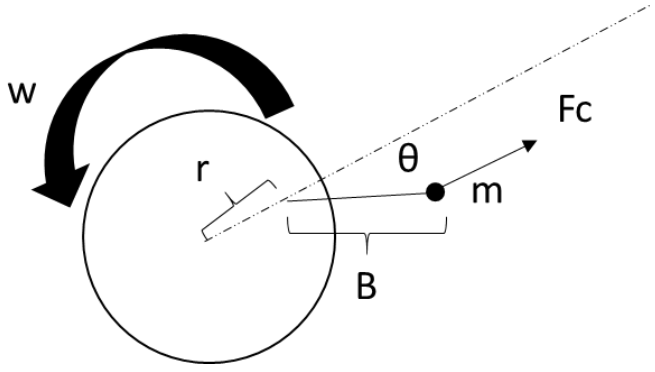

Figure 5.6: Diagram of a simple pendulum attached to a rotating disc at radius, r. The pendulum has an arm of length B, and the pendulum mass swings on a circular arc. The pendulum displacement is theta measured with respect to the rotating disc.

The linearized characteristic equation for the simple, circular path, CPA is:

$$\ddot{\theta} + w^2 \frac{r}{B}\theta + \frac{C}{mB^2}\dot{\theta} = 0 \qquad 3)$$

Where w is the rotational velocity of the shaft, theta is the displacement angle of the pendulum, C is the viscous damping coefficient, m the pendulum mass, and r and b are the radius of the mounting location and pendulum arm respectively. By equating the equation coefficients to a generalized 2nd order characteristic equation (equation 4), a relationship of C in terms of zeta was derived (equation 5).

$$\ddot{\theta} + 2\zeta w_n \dot{\theta} + w_n^2 \theta = 0 \qquad 4)$$

$$2\zeta w m B^2 \sqrt{\frac{r}{B}} = C \qquad 5)$$

Where the tuning order of the simple CPA is:

$$N = \sqrt{\frac{r}{B}} \qquad 6)$$

In actuality the CPA mechanism is more complicated than a simple, circular path pendulum resulting in an inaccurate prediction of the tuning order using equation 6. To compensate for this error, the experimental tuning order (Nexp) was substituted into equation 5. Viscous damping coefficients estimated were estimated using equation 7.

$$C = 2\zeta w m B^2 N_{exp} \qquad 7)$$

While not an exact solution for the damping coefficients of the physical CPA design, the approximation was adequate when the CPA dynamics were well separated from other system dynamics.

5.4.4 Simulated TTFRF of CPA in Fixture:

The TTFRF of lumped parameter models for all hardware in the test setup were simulated to validate the calculated CPA damping estimates. The damping coefficients were also tuned in the model to provide a second estimate for the appropriate viscous damping coefficients. A model of the test setup was previously developed (Figure 5.7) as detailed in previous works.

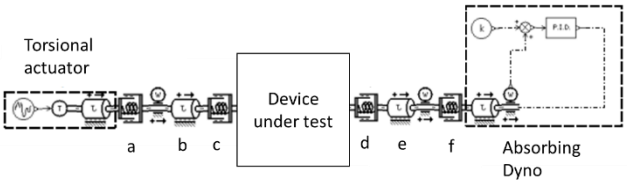

Figure 5.7: Lumped parameter model of the test setup used to measure the TTFRF of the torque converter with CPA hardware. a: input u-joint shaft; b: input spindle inertia; c: input spindle stiffness; d: output spindle stiffness; e: output spindle inertia; f: output u-joint shaft.

The lumped parameter model of the unmodified hardware (Figure 5.8) included torque converter inertias (pump, turbine, ATF) coupled to an arc spring and CPA sub-model. Lastly, the intermediate plate is coupled to the output hub of the torque converter via a straight coil spring stage. The CPA is mounted on the intermediate inertia which is rigidly fixed to the turbine. It was found that the torque converter hydrodynamics had very little influence on the simulated TTFRFs with the lockup clutch engaged. Thus to save simulation time, the hydrodynamic block was not included in the model.

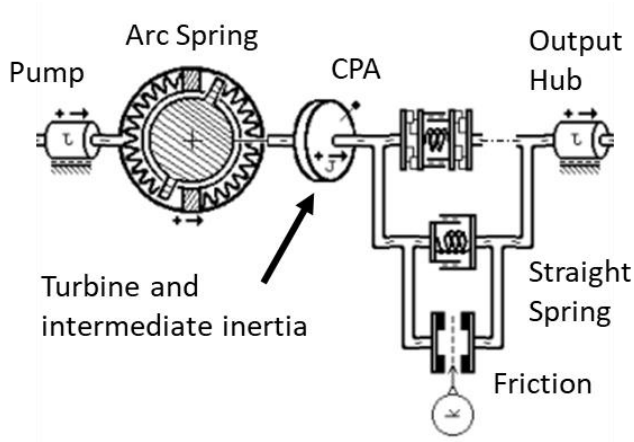

Figure 5.8: Model of the unmodified, two stage damper with CPA.

The custom hardware was similarly modelled with slight modifications to represent the physical modifications. The model of the pinned straight spring hardware replaced the coil spring set with a spring of 3500 Nm/degree stiffness (Figure 5.9). The CPA sub-model was replaced with a lumped turbine, intermediate, pendulum inertia (Figure 5.10) for the pinned CPA model,. The pinned damper model replaced both the arc spring and the straight spring stage with simple springs of 3500 Nm/degree stiffness (Figure 5.11).

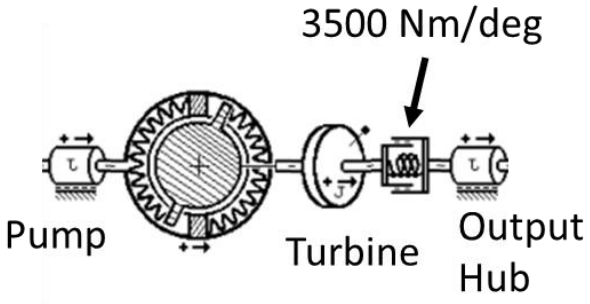

Figure 5.9: Model of the pinned straight spring hardware. CPA and arc spring remain active.

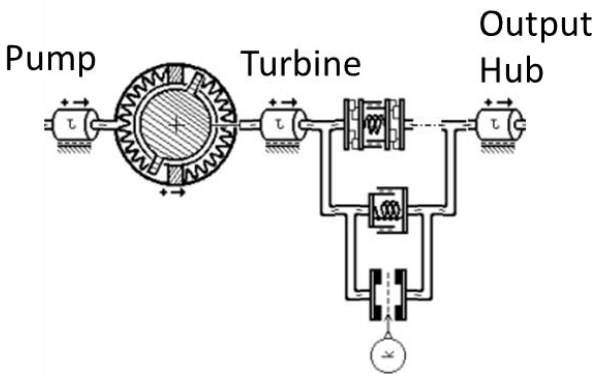

Figure 5.10: Model of the pinned CPA hardware, both damper spring stages active. Note that the turbine inertia now includes the intermediate drive plate inertia as well as the pendulum inertia.

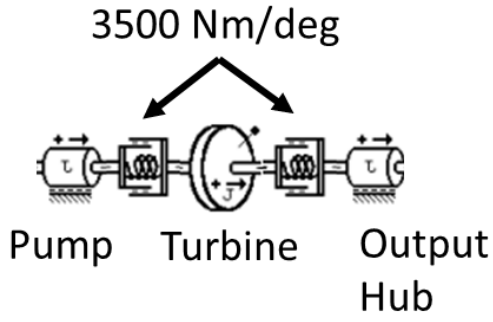

Figure 5.11: Model of the pinned damper hardware, CPA active.

The same excitation signals were generated as in the test for simulating the TTFRF in the test setup model in both frequency and amplitude. The input and output torques were measured at their respective nodes. The signal processing techniques applied to the experimental data was applied to the simulated TTFRFs.

5.5 Results

5.5.1 Preliminary Model Results

Damping effects of the CPA and damper hardware were difficult to distinguish from the TTFRFs when modeling the unmodified hardware. Figures 5.12-5.14 show the influence of damping and friction parameters on the simulated TTFRFs.

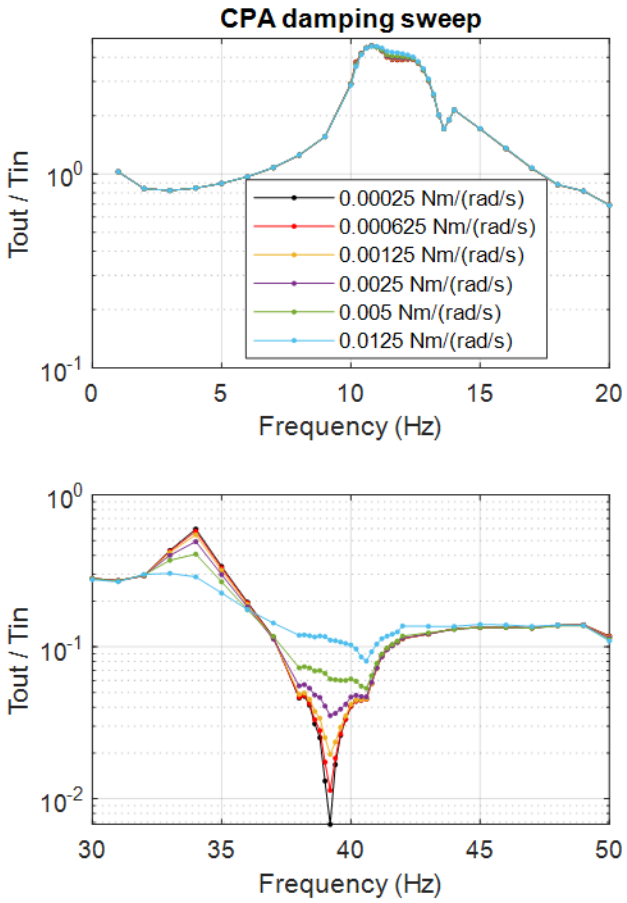

Figure 5.12: Sweeping equivalent viscous damping coefficient of the CPA mechanism in the simulation. Top: Damper resonance shows almost no change. Bottom: CPA anti-resonance shows significant change as a result of a change in viscous damping.

The viscous damping coefficient of the CPA had negligible effect on the damper resonance, while it heavily influenced the amplitude at the tuning order of the CPA. The TTFRF amplitude at the damper resonance and at the CPA's tuning order is influenced by both the arc spring friction coefficient and the friction torque across the straight spring stage.

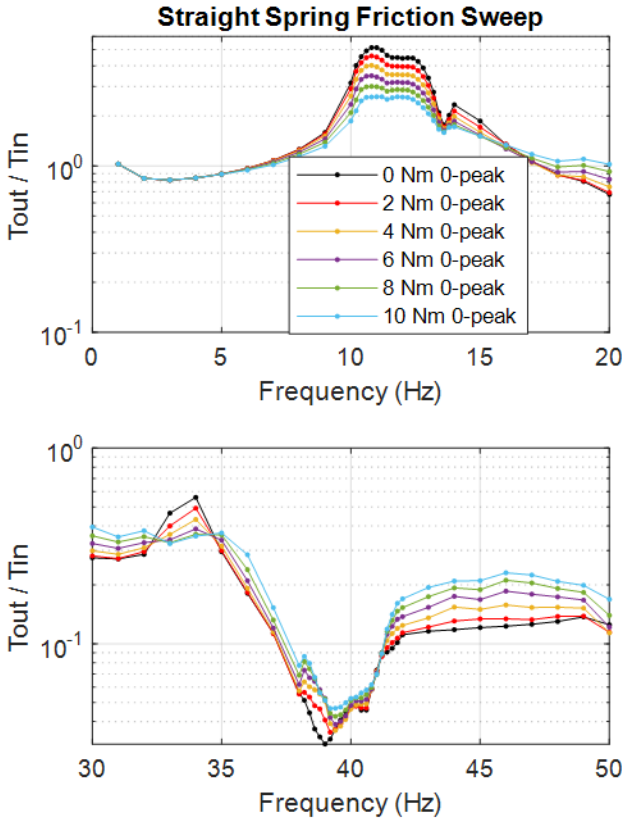

Figure 5.13: Sweeping friction torque across the 2nd spring stage in the simulation. Damper resonance and CPA anti-resonance both change significantly as a result.

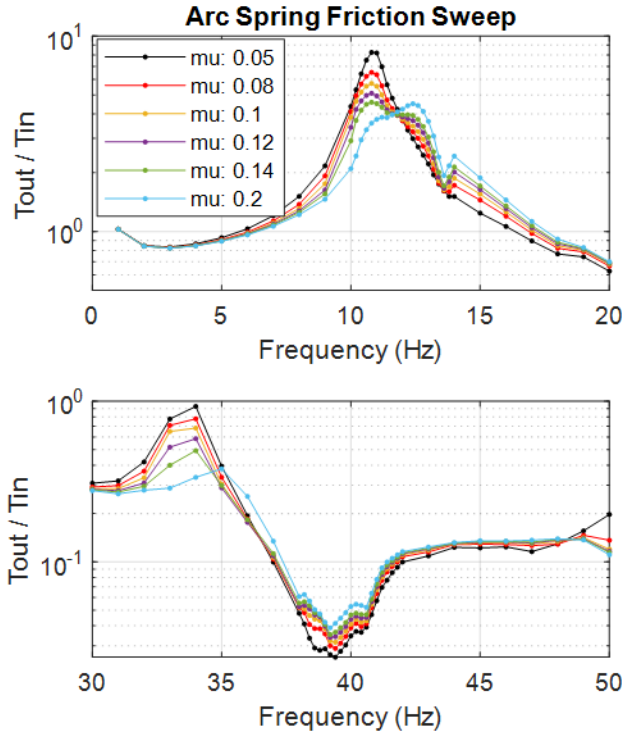

Figure 5.14: Sweeping friction coefficient of the arc spring sub model in the simulation. Both the damper resonance and the CPA anti-resonance show significant change.

The influence of the torque converter damper's friction parameters on the CPA's TTFRF deemed it necessary to test three custom torque converter iterations. The primary intent was estimating the equivalent viscous damping of the CPA mechanism while submerged in ATF in a torque converter.

5.5.2 Experimental TTFRFs

TTFRFs of all hardware iterations were measured in a special test rig. The original, unmodified torque converter hardware was initially tested in previous research (locked clutch article), and those preliminary findings triggered the interest in further testing and characterization of the CPA. The TTFRF of the unmodified hardware (Figure 5.15) displayed several features of interest. The damper resonance showed up in the 11.8 – 13.2 Hz range (depending on operating speed), and an anti-resonance associated with the CPA was located at frequency that corresponded to 2nd order. At 1800 and 2100rpm, the TTFRF appeared to have a peak within the CPA anti-resonant feature. The cause of this behavior was unknown, and it was expected that this artifact was a result of the tri-tone excitation coupled with the relatively high level of friction relative to the excitation amplitude (Ta). Also, the torsional inputs at 2nd order become attenuated much more at the higher operating speeds, thus could be more noise at these frequencies. The TTFRF of the unmodified hardware should be measured using the single tone method (at higher

dynamic torque amplitude), but for the purpose of characterizing CPA damping, was deemed unnecessary. Other artifacts of the test rig in the TTFRF include a dyno control mode at 1 Hz, an output shaft mode, and output spindle torsion mode. These modes were discussed in more detail in past works (Chapters 3 and 4).

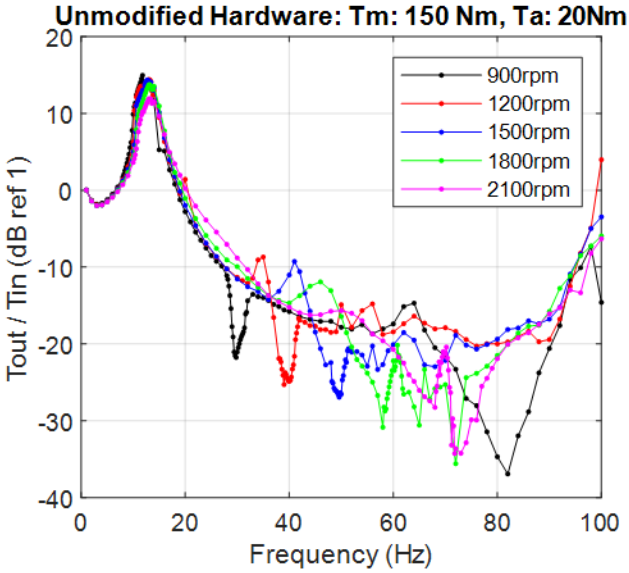

Figure 5.15: Experimental TTFRFs of the unmodified damper hardware at all operating speeds. Damper mode at 11.8-13.2 Hz range. CPA anti-resonance tracks with 2nd order (ex. 30 Hz at 900rpm).

The TTFRFs of all hardware iterations (Figure 5.16) illustrated the effect of each hardware modification on the overall system dynamics. Locking the straight spring stage of the damper highlighted the contribution of the arc spring and CPA in the TTFRF, and with the pinned damper hardware, a torsion mode of the test setup shafting was present at 30 Hz. The pinned CPA hardware had a significant difference in the damper mode frequency. This indicated a difference in the damper designs. Further investigation revealed two different damper specifications between the custom hardware iterations and the unmodified hardware. The CPA design specification was consistent across all hardware so the viscous damping coefficient could still be estimated and validated using all of the custom hardware test results.

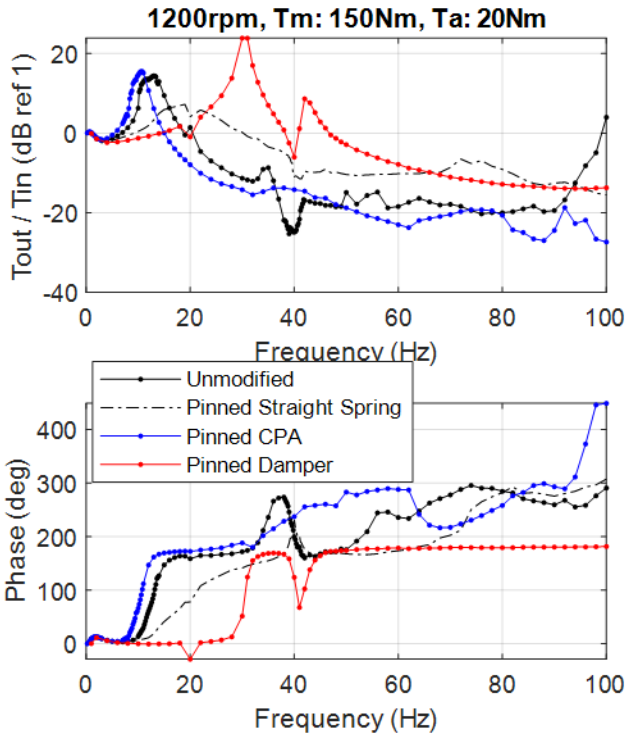

Figure 5.16: Comparing TTFRFs of all hardware (0-100 Hz range).

Single tone excitation was used to measure the TTFRF of the CPA anti-resonance about 2nd order (tuning order). This testing was only done on the pinned damper and pinned straight spring hardware, but the TTFRF about 2nd order was plotted for all hardware (Figure 5.17). The first three hardware iterations (unmodified, pinned straight spring, pinned CPA) were tested using 5 operating speeds (900, 1200, 1500, 1800, 2100 rpm). The same operating speeds could not be used for the pinned damper hardware due to the lightly damped torsion mode at 30 Hz. At 900rpm, the CPA anti-resonance would attenuate the torsion mode, but the assumption of a single degree of freedom system would breakdown in estimating viscous damping. At 1500rpm, the 1st order imbalance in the shafting was amplified by the torsion mode so much that there was no more headroom to add other frequency content to the measurement. Thus, the pinned damper hardware was tested at 600, 1200, 1800, and 2100rpm.

The pinned CPA hardware displayed no CPA anti-resonance about second order (as expected), and the other hardware displayed the anti-resonance. The anti-resonance of the unmodified hardware is not smooth due to the tri-tone excitation method and the influence of the damper's friction. The pinned straight spring hardware was tested with the single-tone method at a much higher torsional amplitude and showed much smoother results despite the effects of arc-spring friction.

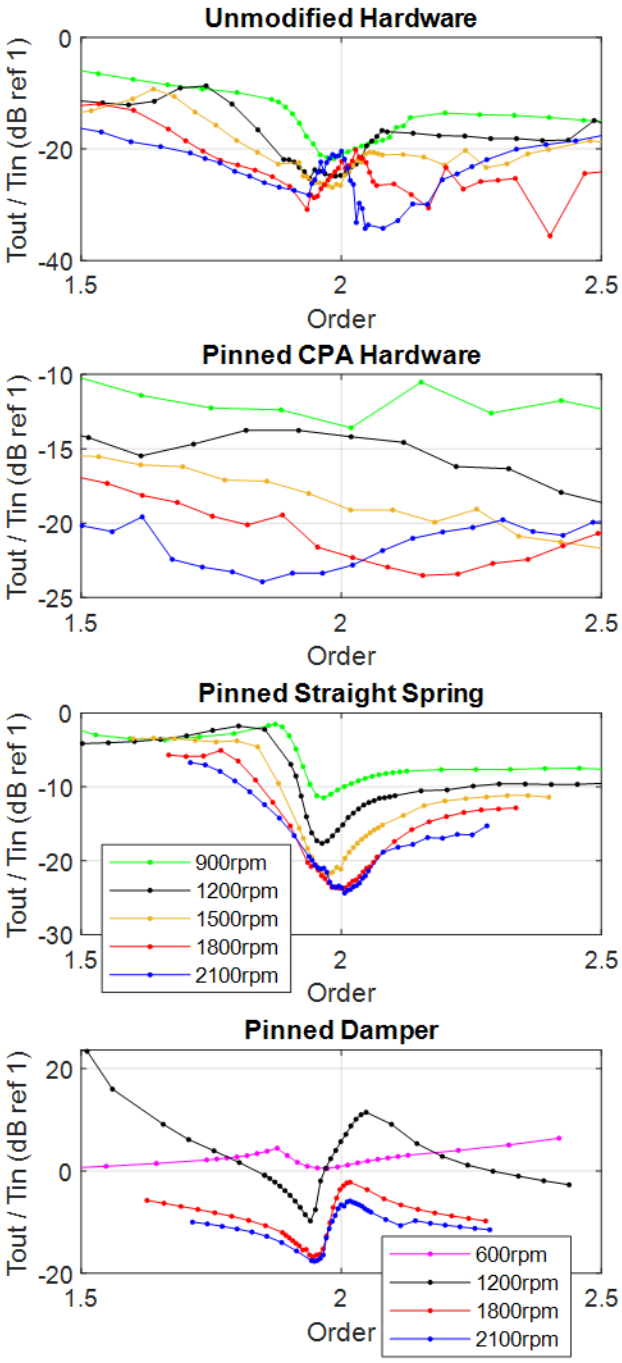

Figure 5.17: Experimental TTFRFs about 2nd order of all hardware iterations.

The pinned CPA hardware displayed a consistent anti-resonance over the 900-1500rpm range (at 1.96 order), but at 1800 and 2100rpm the anti-resonance increased to 2nd order. Again, there appears to be some influence on the CPA performance due to the damper springs. As operating speed increased, 2nd order moved further away from the arc spring

resonance resulting in decreased in amplitude in the TTFRF with increased speed. The results converged at 1800 and 2100rpm.

As expected, the pinned damper displayed the most consistent CPA anti-resonance behavior. However, the torsion mode of the test setup heavily influenced the shape of the TTFRF at 900 and 1200rpm. As the operating speed increased to 1800 and 2100rpm, the TTFRF converges to approximately the same value (when plotted vs order). This indicates that when the CPA anti-resonance is well spaced from the torsion mode, the underlying assumption of a single degree of freedom system holds true.

The pinned CPA hardware was investigated further by measuring the TTFRF at two torsional excitation amplitudes (Figure 5.18). The main differences in the results are the anti-resonant frequency (and order) and the bandwidth of the anti-resonance. This may indicate that friction is larger than the centrifugal force can overcome at the low excitations. This would cause the pendulum to attenuate vibration only near second order.

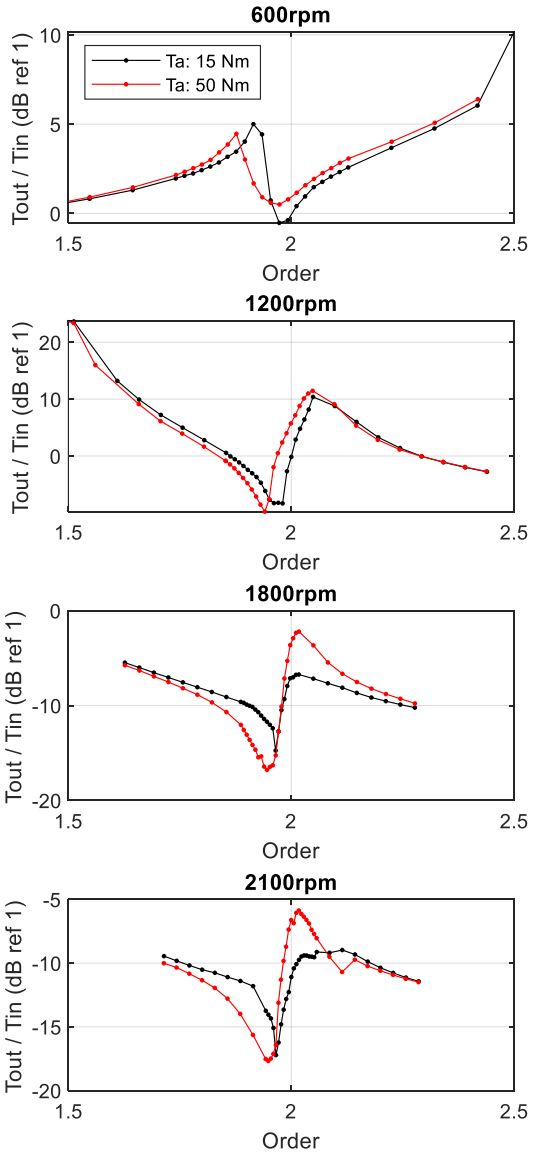

Figure 5.18: TTFRFs of the pinned damper hardware at two levels of dynamic torque input.

5.5.3 Estimating Viscous Damping

Two methods were deployed for estimating the equivalent viscous damping coefficient of the CPA mechanism from the measured TTFRFs. First, equation 7 computed the damping coefficient using experimental damping ratio and experimental tuning order—using the pinned damper hardware (Table 5.2). The second method involved manually tuning the viscous damping coefficient in the simulation until the simulated TTFRF matched the experimental TTFRF (Table 5.3).

Table 5.2: Equivalent viscous damping of the CPA mechanism estimated using equation 7.

Speed (rpm)	C (Nm/(rad/s)) at Ta=15 Nm	C (Nm/(rad/s)) at Ta=50 Nm
600	0.0024	0.0039
1200	0.0012	0.0008
1800	0.0011	0.0025
2100	0.0012	0.0033

Table 5.3: Equivalent viscous damping of the CPA mechanism estimated by tuning C to match experimental TTFRFs.

Speed (rpm)	C (Nm/(rad/s)) at Ta=15 Nm	C (Nm/(rad/s)) at Ta=50 Nm
600	0.0005	0.001
1200	0.0015	0.003
1800	0.005	0.002
2100	0.005	0.003

The viscous damping coefficients at 900 and 1500rpm were tuned to match the TTFRFs of the pinned straight spring hardware. The TTFRFs in question were acquired Ta = 120 Nm, and the estimated damping coefficients place into the tuned viscous damping table for Ta = 50 Nm (Table 5.4).

Table 5.4: Equivalent viscous damping coefficients of the CPA mechanism.

Speed (rpm)	C (Nm/(rad/s))
600	0.001
900	0.002
1200	0.003
1500	0.003
1800	0.002
2100	0.003

5.5.4 Simulated TTFRFs

The TTFRFs of the pinned damper hardware were simulated using the updated viscous damping coefficients acquired via tuning and computation. The viscous damping coefficients computed from the 15 Nm input amplitude test underestimated the damping at 1800 and 2100rpm, overestimated damping at 600rpm, and at 1200rpm, predicted the TTFRF well (Figure 5.19). The tuned damping coefficients predicted the TTFRF better

than the computed coefficients when simulating 600, 1800, and 2000 rpm. As previously noted, the friction in the CPA mechanism prevents free oscillation of the CPA when testing at low excitation amplitudes. Therefore, the equivalent viscous damping coefficients estimated from the low input torque tests were questionable.

For the high input torque tests (Ta = 50 Nm, Figure 5.20), the computed and tuned damping estimates agreed at 1800 and 2100rpm, and replicated the experimental TTFRF well. At 600 and 1200 rpm the computed damping values again did not replicate the experimental TTFRF well. At these operating speeds, the tuned damping estimates achieved much better correlation between simulation and test.

A critical assumption behind equation 7, used to estimate damping coefficients, was that the CPA was a single degree of freedom system rotating at a constant speed (refer back to Figure 5.6). This assumption made it possible to use the single degree of freedom characteristic equation (equation 3) to formulate equation 7. When operating the CPA near another system mode, the assumption fell apart, and the damping estimate produced a poorly correlated TTFRF.

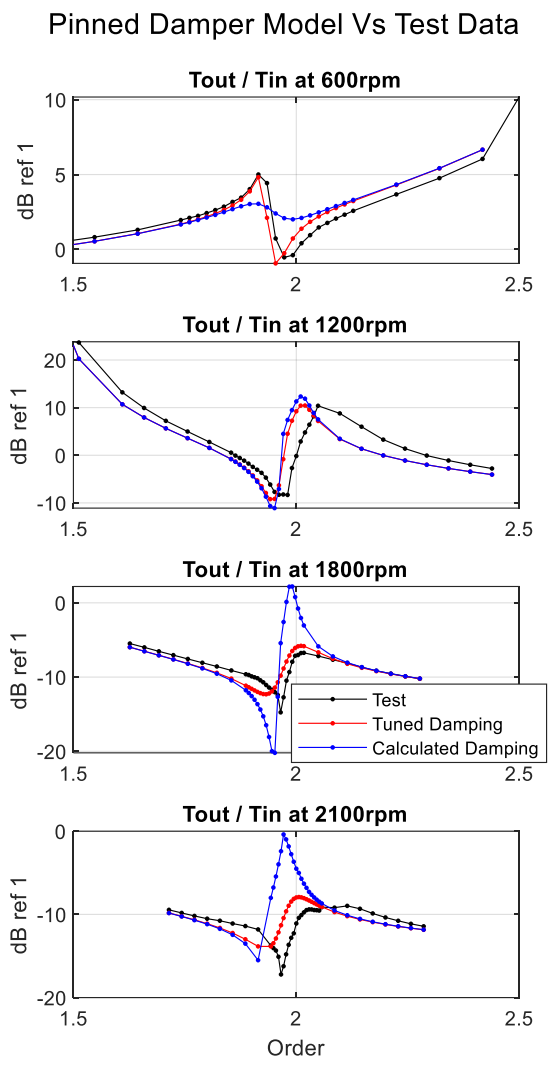

Figure 5.19: Comparing the simulated TTFRFs, using tuned and calculated damping values, against the respective test data. Ta = 15 Nm.

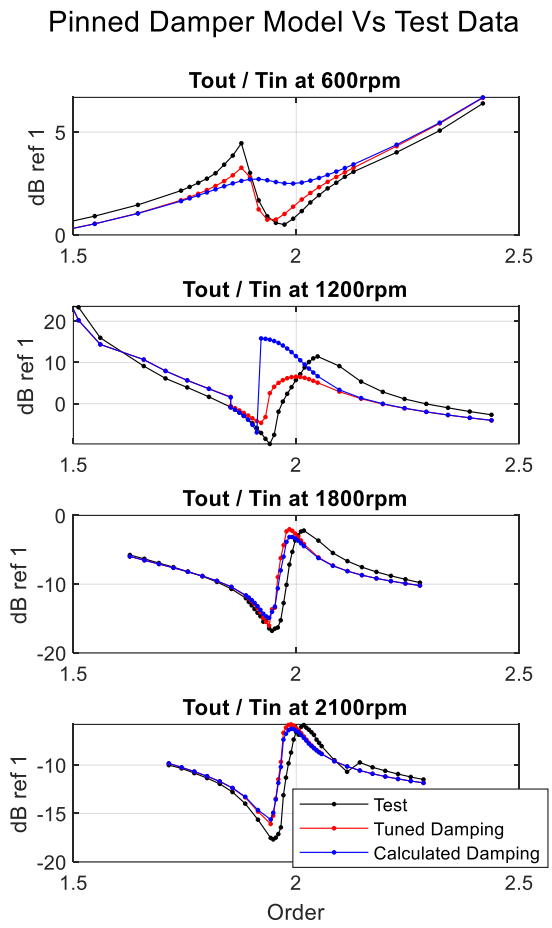

Figure 5.20: Comparing the simulated TTFRFs, using tuned and calculated damping values, against the respective test data. Ta = 50 Nm.

Since the pinned CPA hardware wasn't tested or damping characterized at 900 and 1500 rpm, the damping coefficient table was tuned further in the pinned straight spring hardware model. The simulated TTFRFs (Figure 5.21), achieved good model to data correlation using the damping coefficients in Table 5.4. At 1800 and 2100rpm, the pinned straight spring model under predicted the tuning order and the damping was too low. The pinned straight spring hardware had more friction due to the active arc spring. Friction in the arc spring likely caused the error in the model at 1800 and 2100 rpm. This investigation did not thoroughly investigate damper spring friction parameters.

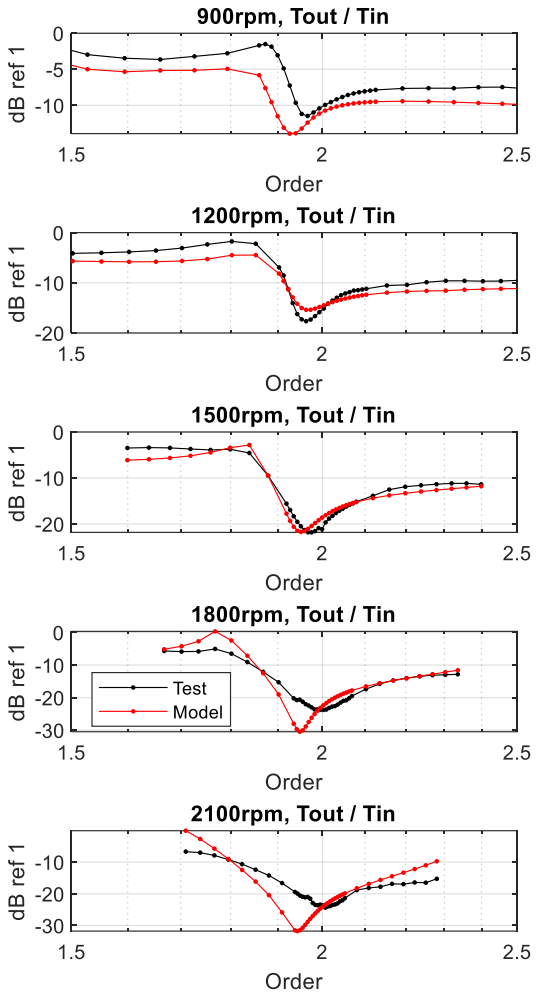

Figure 5.21: Experimental and simulated TTFRFs of the pinned straight spring hardware (C) about 2nd order. Using the newly tuned CPA damping lookup table.

5.6 Discussion

The equivalent viscous damping coefficient of a CPA installed in a torque converter damper is now quantified with experimental data acquired on custom torque converter hardware. Of the two methods used to estimate equivalent viscous damping, the manual tuning method is the most robust to the influence of other system dynamics. Compared to other works involving the experimental characterization of CPA's in a torque converter [46], this research provides test results over a broad range of operating conditions, and a validated estimate for CPA damping. This research also provides insight into the effect of damper friction on the CPA performance, but does not separate friction in the CPA mechanism from the viscous damping. The viscous damping coefficients effectively account for all losses in the CPA mechanism.

A final validation of the viscous damping coefficients involved simulating the unmodified hardware using the new CPA damping table (Table 5.4). While the damper designs differed between the unmodified hardware and the custom hardware, the CPA design remained the same across all hardware. The TTFRF results are only shown about 2nd order to demonstrate the improvement of the simulation in replicating the CPA's anti-resonance (Figure 5.22). For speeds 900-1500rpm, the new damping table achieved better correlation than the original damping table. At 1800rpm both the new and old simulations had identical damping coefficients, and at 2100, the change very minor. Again, difficulty in comparing at the higher speeds could be largely due to the poor quality of the test data acquired on the unmodified hardware at these speeds. The TTFRFs at 1800 and 2100 rpm were acquired using the tri-tone method, and the dynamic torque (Ta = 20 Nm) not large enough to meaningful response amplitudes.

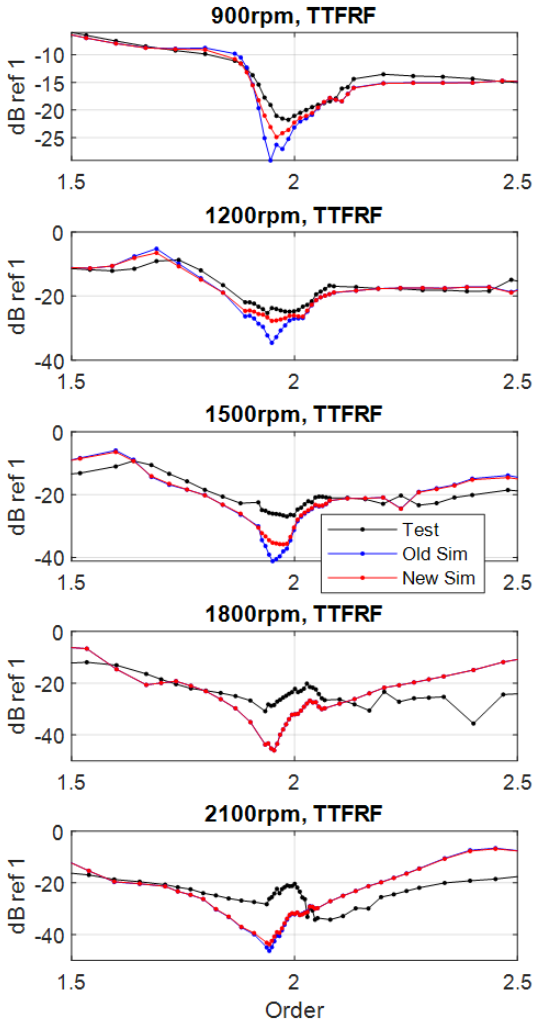

Figure 5.22: Simulated and experimental TTFRFs of the unmodified hardware (A). Two sets of simulation results are shown comparing old and new damping coefficients.

An unexpected finding involving the tuning order of the CPA was the fact that the anti-resonant frequency in the TTFRF did not correspond to the maximum displacement in the pendulum. Figure 5.23 contains cursors at the specific excitation order where the pendulum displacement reaches maximum in the model (Figure 5.24), and the model consistently shows that maximum displacement does not occur at the anti-resonance.

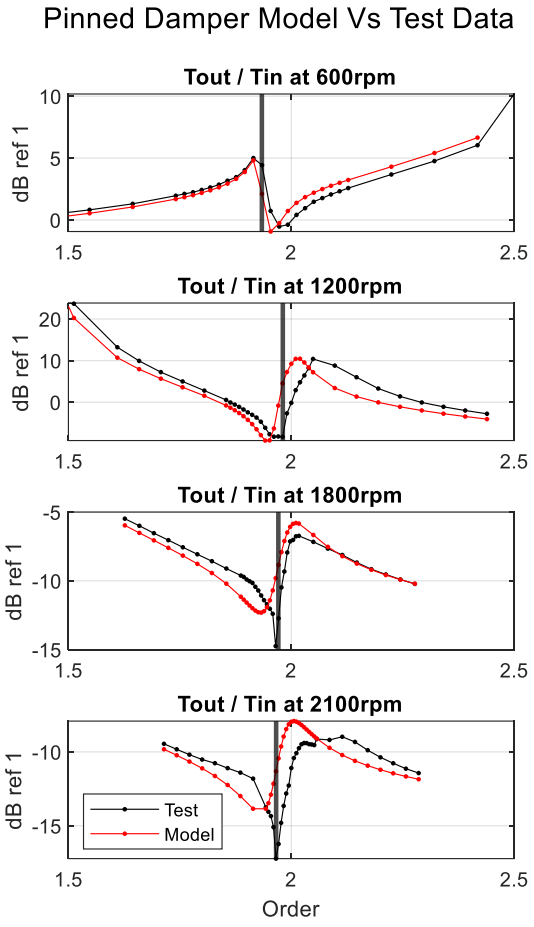

Figure 5.23: Simulated vs experimental TTFRF. Damping in these simulation results were tuned to achieve best match with test data. Cursor denotes where largest pendulum displacement happens in the simulation (see also Figure 5.24). Tm: 150 Nm, Ta: 15 Nm

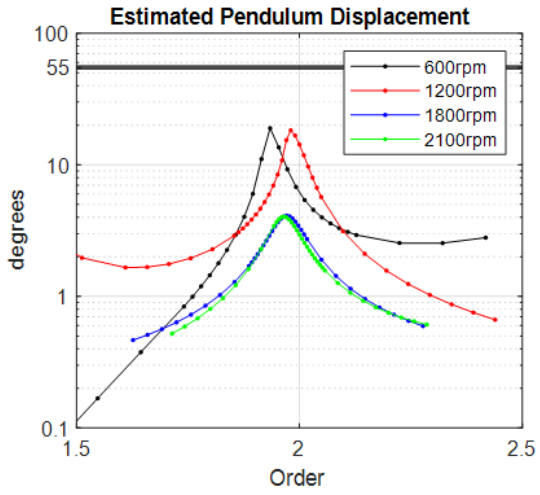

Figure 5.24: Estimated pendulum displacement from the CPA sub-model. Cursor denotes maximum displacement of the CPA mechanism. Tm: 150 Nm, Ta: 15 Nm.

Since the excitation order corresponding with maximum pendulum displacement did not coincide with the anti-resonance in the simulated TTFRF (tuning order), the other measured signals were compared to pendulum displacement to see if one particular measurement indicates max pendulum displacement. It was found that the relative phase between input and output torque (likewise input and output speed) reliably indicates the excitation order corresponding to maximum pendulum displacement (Figure 5.25). The CPA creates a peak (or valley) in the relative phase, and the local extreme of this feature in the phase measurement accurately predicts the excitation order (or frequency) of max displacement. This predictor of maximum pendulum displacement is useful in situations where pendulum displacement can't be directly measured.

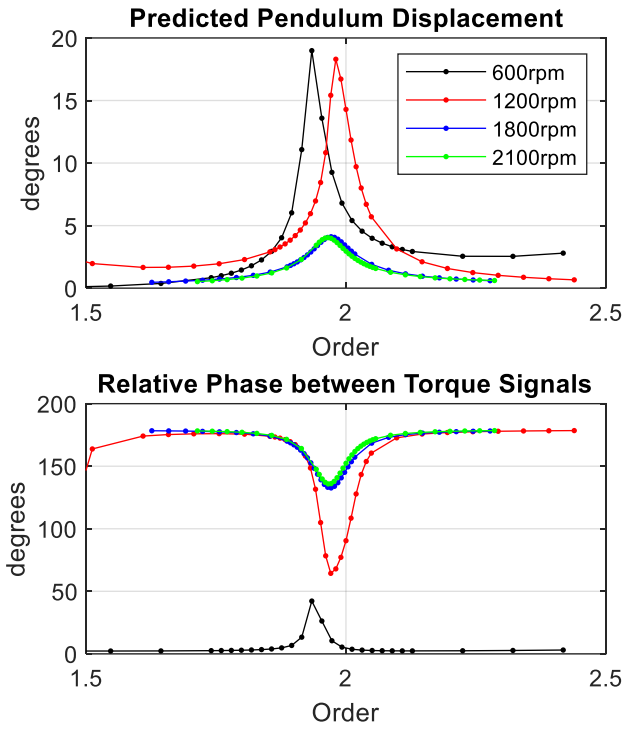

Figure 5.25: Top: Predicted pendulum displacement angle from the pinned CPA model. Bottom: Relative phase between input and output torque signals (also from the pinned CPA model). Ta = 15 Nm.

5.7 Conclusion

For the first time, a CPA was characterized, operating in a torque converter clutch, submerged in ATF. The TTFRFs were measured on pinned damper hardware, pinned CPA hardware, and pinned straight spring hardware. A viscous damping look-up table was estimated for the CPA component of the torque converter damper, and model correlation improved. An interesting finding was the ability of the relative phase between input torque and output torque signals in predicting the order or frequency of maximum pendulum displacement.

6 Conclusions

6.1 Original Contributions

The experimental and analytical works presented in this dissertation contributed to the understanding of torque converter and CPA dynamics, and introduced a unique torsional vibration absorber. The new vibration absorber concept reduces the added mass of a TVA tuned to low frequencies, and the experimental TTFRFs of torque converters and a CPA were used to estimate friction and damping, thus improving model accuracy.

A design and test of a unique vibration absorber configuration proves the utility of a planetary gear set in targeting low frequency vibrations. The planetary gear set allows for packaging space savings by taking advantage of reflected inertia across a fixed gear ratio. The spring and mass of the absorber was coupled to the freely spinning gear of the planetary gear set, and the gear set pinned to the rotating shaft. Thus the prototype configuration also reflected the spring stiffness across the gear ratio. A different configuration with the spring between the shaft and gear set would achieve reflected inertia gains, without changing the apparent spring stiffness.

TTFRFs measured at several operating speeds—clutch open and applied—characterized the speed dependent friction in a torque converter clutch. The open torque converter TTFRFs predicted a lower level of damper friction than the locked torque converter TTFRFs. Thus, an additional viscous damping term compensated for additional damping effects when operating clutch locked in the model. Relative motion between the ATF and torque converter elements, under torsional excitation, justified the additional viscous damping term.

The open torque converter TTFRFs also showed an unexpected resonance, unique to turbine damper lockup clutch architectures, which was later confirmed as the damper resonance (decoupled from the pump and input shafting). The presence of the damper mode demonstrates that while heavily attenuated, torsional vibrations get transmitted across the open torque converter. The open torque converter TTFRFs validated a widely used hydrodynamic torque converter model in the low frequency range (0-20 Hz). However, the model predicted a consistently higher natural frequency damper mode than shown in experimental results. Initial investigation suggested that the ATF undergoing toroidal flow may reflect additional inertia on the turbine, and explain the natural frequency error.

The equivalent viscous damping of a CPA submerged in ATF was characterized by measuring the TTFRF of a customized torque converter. The torque converter clutch damper featured two spring stages (arc spring and straight spring) in series, with a CPA coupled to the turbine inertia. The custom hardware had the springs pinned, leaving only the CPA active. Other customized hardware includes: pinned CPA and pinned straight spring. The TTFRFs of the fully pinned damper yielded a viscous damping estimate uninfluenced by damper friction. A mismatch in tuning frequency of the CPA and

frequency of maximum pendulum displacement was noted, and further investigation revealed that the relative phase measurement (between input and response signals) accurately predicts maximum pendulum displacement frequency.

6.2 Future Work

The research discussed in this dissertation has generated more questions for future research. Future work includes testing a modified pTVA mechanism, using the TTFRFs of torque converter dampers to validate several friction models, modelling friction losses of the CPA mechanism, deriving a new system of equations for a hydrodynamic torque converter model, and validating other hydrodynamic TC models.

The pTVA as presented in chapter 2 was limited by the fact that the gear ratio didn't influence the tuning of the absorber device. By modifying the pTVA—locating the gearset between spring and absorber—the gearset effectively changes the tuning frequency by a factor of the gear ratio. This allows for a stiffer, more physically realizable spring at a given tuning frequency. The pTVA could be modified to physically realize the described configuration, but rather than fabricating and testing a new prototype, the equations of motion—validated by test data—can be modified to reflect the proposed change. Then, the difference in stiffness and inertia parameters (between pTVA and modified pTVA) to achieve the same tuning frequency would indicate the preferred configuration (the goal being to minimize absorber inertia and maximize absorber stiffness).

In Chapter 3, friction in the torque converter damper was typically modelled using a hyperbolic tangent friction model. Two different trends were observed experimentally regarding friction. All test data showed increased resonance attenuation with increasing speed (i.e. increased friction torque), but the two stage turbine damper showed a decrease in resonant frequency, while the conventional damper and damper with CPA showed an increase in resonant frequency. This indicates stiction effects, and a survey of friction models would improve understanding of how different friction models influence simulated TTFRF results.

The CPA model did not account for friction, and the model correlation suffered at low amplitude dynamic torque inputs. When operating in a clutch damper or dual mass flywheel, the CPA is not exposed to raw engine torsionals. The springs used in the damper (or dual mass flywheel), attenuate the engine torsionals, and much lower dynamic torque amplitudes excite the CPA. By accounting for friction in the CPA model, the amplitude sensitivity of the CPA is captured.

Open torque converter testing and modelling specific to turbine damper architectures revealed a consistent natural frequency error in the turbine damper mode. A hypothesis regarding reflected inertia of ATF in toroidal flow, at low speed ratios, was presented. An updated derivation of the torque converter system equations (accounting for any reflected inertia effects at low speed ratio) is necessary to justify the hypothesis and eliminate

natural frequency error in the turbine damper mode. Prior to deriving a new dynamic torque converter model, a survey of other published torque converter models should be conducted and their respective TTFRFs compared to experimental data.

7 Reference List

1. Hula, A., et al., *The 2019 EPA Automotive Trends Report - Greenhouse Gas Emissions, Fuel Economy, and Technolgy since 1975*. 2020, United States Environmental Protection Agency.
2. Swank, M. and P. Lindemann, *Dynamic Absorbers for Modern Powertrains*. 2011, SAE International.
3. Den Hartog, J.P., *Mechanical vibrations*. 1956: McGraw-Hill.
4. Swank, M.G. and P. Lindemann, *Torque converter with turbine mass absorber*, USPTO, Editor. 2012, Schaeffler Technologies AG & Co. KG: US.
5. Meingaßner, G.J., H. Pflaum, and K. Stahl, *Innovative Torsional Vibration Reduction Devices - Vehicle-Related Design and Component Strength Analysis*. 2014, SAE International.
6. Brzeski, P., et al., *The application of inerter in tuned mass absorber.* International Journal of Non-Linear Mechanics, 2015. **70**: p. 20-29.
7. Brzeski, P., T. Kapitaniak, and P. Perlikowski, *Novel type of tuned mass damper with inerter which enables changes of inertance.* Journal of Sound and Vibration, 2015. **349**: p. 56-66.
8. Smith, M.C., *Synthesis of mechanical networks: the inerter.* IEEE Transactions on Automatic Control, 2002. **47**(10): p. 1648-1662.
9. Ogawa, A. and K. Adachi, *Theoretical Studies of Influence of the Configuration on the Function of Planetary Gear Inerter for Rotating Drivetrain.* International Journal of Automotive Engineering, 2018. **9**(2): p. 48-55.
10. Mark A. Gehringer, D.L.R., *Planetary Torsional Vibration Absorber System for a Vehicle*, USPTO, Editor. 2019, GM Global Technolgy Operations LLC: US.
11. Jurmu, L., et al., *Design and test of a torsional vibration absorber in series with a planetary gearset.* Journal of Vibration and Control, 2020: p. 1077546320943801.
12. Couderc, P., et al., *VEHICLE DRIVELINE DYNAMIC BEHAVIOUR: EXPERIMENTATION AND SIMULATION.* Journal of Sound and Vibration, 1998. **218**(1): p. 133-157.
13. Farshidianfar, A., M. Ebrahimi, and H. Bartlett, *Hybrid modelling and simulation of the torsional vibration of vehicle driveline systems.* Proceedings of the Institution of Mechanical Engineers, Part D: Journal of Automobile Engineering, 2001. **215**(2): p. 217-229.
14. Hage, A., A. Szatkowski, and Z. Li, *Improving Low Frequency Torsional Vibrations NVH Performance through Analysis and Test*. 2007, SAE International.
15. Girstmair, J., et al., *Improved Comfort Analysis and Drivability Assessment by the Use of an Extended Power Train Model for Automatic Transmissions.* SAE International Journal of Passenger Cars - Mechanical Systems, 2012. **5**(3): p. 1073-1083.
16. Yoon, J.-Y. and R. Singh, *Effect of the multi-staged clutch damper characteristics on the transmission gear rattle under two engine conditions.* Proceedings of the Institution of Mechanical Engineers, Part D: Journal of Automobile Engineering, 2013. **227**(9): p. 1273-1294.
17. Huwei Wu, G.W., *Drivelin Torsional Analysis and Clutch Damper Optimization for Reducing Gear Rattle.* Shock and Vibration, 2016. **2016**: p. 24.
18. Furlich, J., J. Blough, and D. Robinette, *Torsional Vibration Analysis of Six Speed MT Transmission and Driveline from Road to Lab*. 2017, SAE International.

19. Li, M., M. Khonsari, and R. Yang, *Dynamics Analysis of Torsional Vibration Induced by Clutch and Gear Set in Automatic Transmission.* International Journal of Automotive Technology, 2018. **19**(3): p. 473-488.
20. Krak, M., J. Dreyer, and R. Singh, *Development of a Non-Linear Clutch Damper Experiment Exhibiting Transient Dynamics*. 2015, SAE International.
21. Krak, M.D., J.T. Dreyer, and R. Singh, *Step-response of a torsional device with multiple discontinuous non-linearities: Formulation of a vibratory experiment.* Mechanical Systems and Signal Processing, 2016. **70-71**: p. 1117-1130.
22. Aurora-Smith, A., *The Simulation and Experimental Characterisation of the Torque Converter Damper System*. 2017.
23. Ngoc, M.V., S.C. Shin, and G.W. Kim, *Comparative study on non-traditional torsional vibration isolators for automotive clutch dampers.* Noise Control Engineering Journal, 2018. **66**(6): p. 541-550.
24. Gi-Woo, K. and K. Jung-June, *NON-TRADITIONAL TORSIONAL ISOLATORS FOR TRANSMISSION CLUTCH DAMPER*. 2016, FISITA (UK) Limited: Stansted.
25. Kim, G.-W. and S.-C. Shin, *Research on the torque transmissibility of the passive torsional vibration isolator in an automotive clutch damper.* Proceedings of the Institution of Mechanical Engineers, Part D: Journal of Automobile Engineering, 2015. **229**(13): p. 1840-1847.
26. Ishihara, T. and R.I. Emori, *Torque Converter as a Vibration Damper and Its Transient Characteristics*. 1966, SAE International.
27. Hrovat, D. and W.E. Tobler, *Bond graph modeling and computer simulation of automotive torque converters.* Journal of the Franklin Institute, 1985. **319**(1): p. 93-114.
28. Cameron, T.M., et al., *ATF Effects on Friction Stability in Slip-Controlled Torque Converter Clutches*. 2003, SAE International.
29. Janarthanan, B., C. Padmanabhan, and C. Sujatha, *Longitudinal dynamics of a tracked vehicle: Simulation and experiment.* Journal of Terramechanics, 2012. **49**(2): p. 63-72.
30. Koprubasi, K., *Modeling and Control of a Hybrid-Electric Vehicle for Drivability and Fuel Economy Improvements*. 2008, The Ohio State University.
31. Deur, J., et al., *Recent Advances in Control-Oriented Modeling of Automotive Power Train Dynamics.* IEEE/ASME Transactions on Mechatronics, 2006. **11**(5): p. 513-523.
32. Cho, D. and J.K. Hedrick, *Automotive Powertrain Modeling for Control.* Journal of Dynamic Systems, Measurement, and Control, 1989. **111**(4): p. 568-576.
33. Pohl, B., *Transient Torque Converter Performance, Testing, Simulation and Reverse Engineering.* SAE Transactions, 2003. **112**: p. 201-216.
34. Robinette, D., M. Grimmer, and R. Beikmann, *Dynamic Torque Characteristics of the Hydrodynamic Torque Converter*. 2011, SAE International.
35. Sarazin, R.R.R., *Means Adapted To Reduce The Torsional Oscillations of Crankshafts*, USPTO, Editor. 1937: USA.
36. Kooy, A., *Isolation is the Key*, in *Solving the Powertrain Puzzle: 10th Schaeffler Symposium April 3/4, 2014*, H. Schaeffler Technologies Gmb and K.G. Co, Editors. 2014, Springer Fachmedien Wiesbaden: Wiesbaden. p. 78-93.
37. Shi, C. and R.G. Parker, *Modal properties and stability of centrifugal pendulum vibration absorber systems with equally spaced, identical absorbers.* Journal of Sound and Vibration, 2012. **331**(21): p. 4807-4824.
38. Madden, J.F., *Constant frequency bifilar vibration absorber*. 1980, Google Patents.

39. Denman, H.H., *Tautochronic bifilar pendulum torsion absorbers for reciprocating engines.* Journal of Sound and Vibration, 1992. **159**(2): p. 251-277.
40. Mayet, J. and H. Ulbrich, *Tautochronic centrifugal pendulum vibration absorbers: General design and analysis.* Journal of Sound and Vibration, 2014. **333**(3): p. 711-729.
41. Maguire, J.M., S. Bai, and H. Peng, *Dynamic Analysis and Control System Design of Automatic Transmissions*. 2013: SAE International.
42. Cirelli, M., et al., *A Design Chart Approach for the Tuning of Parallel and Trapezoidal Bifilar Centrifugal Pendulum.* Mechanism and Machine Theory, 2019. **140**: p. 711-729.
43. Haddow, A.G. and S.W. Shaw, *Centrifugal Pendulum Vibration Absorbers: An Experimental and Theoretical Investigation.* Nonlinear Dynamics, 2003. **34**(3): p. 293-307.
44. Vidmar, B.J., et al., *The effects of Coulomb friction on the performance of centrifugal pendulum vibration absorbers.* Nonlinear Dynamics, 2012. **69**(1): p. 589-600.
45. Gomez, E.R., I.L. Arteaga, and L. Kari, *Normal-force dependant friction in centrifugal pendulum vibration absorbers: Simulation and experimental investigations.* Journal of Sound and Vibration, 2021. **492**: p. 115815.
46. Song, S.-Y., S.-C. Shin, and G.-W. Kim, *Torsional Vibration Isolation Performance Evaluation of Centrifugal Pendulum Absorbers for Clutch Dampers.* Transactions of the Korean Society for Noise and Vibration Engineering, 2016. **26**: p. 436-442.
47. Wellmann, T., et al., *Aspects of Driveline Integration for Optimized Vehicle NVH Characteristics*. 2007, SAE International.
48. Kooy, A., *Solving the Powertrain Puzzle.* 2014: p. 78-93.
49. Albright, M., T. Crawford, and F. Speckhart, *Dynamic Testing and Evaluation of the Torsional Vibration Absorber*. 1994, SAE International.
50. Amdall, J.K. and W.O. Jankovsky, *Drive line vibration absorber*, USPTO, Editor. 1976, Caterpillar Tractor Co: US.
51. Igusa, T. and K. Xu, *Vibration Control Using Multiple Tuned Mass Dampers.* Journal of Sound and Vibration, 1994. **175**(4): p. 491-503.
52. Garrido, H., O. Curadelli, and D. Ambrosini, *Improvement of tuned mass damper by using rotational inertia through tuned viscous mass damper.* Engineering Structures, 2013. **56**: p. 2149-2153.
53. Ivanco, T.G., *Compact vibration damper*, USPTO, Editor. 2014, The United States of America as represented by the Administrator of the National Aeronautics and Space Administration: US.
54. Hosek, M., H. Elmali, and N. Olgac, *A TUNABLE TORSIONAL VIBRATION ABSORBER: THE CENTRIFUGAL DELAYED RESONATOR.* Journal of Sound and Vibration, 1997. **205**(2): p. 151-165.
55. Hoang, N., N. Zhang, and H. Du, *A dynamic absorber with a soft magnetorheological elastomer for powertrain vibration suppression.* Smart Materials and Structures, 2009. **18**(7): p. 074009.
56. Stahl, K., et al. *Planetary Centrifugal Pendulum Absorber (pCPA) – New type of Centrifugal Pendulum Absorber for Applications in Highly Downsized Hybrid and Range Extender Combustion Engines*. in *Conference on Future Automotive Technology*. 2013. Wiesbaden: Springer Fachmedien Wiesbaden.
57. Marian, L. and A. Giaralis, *Optimal design of a novel tuned mass-damper–inerter (TMDI) passive vibration control configuration for stochastically support-excited structural systems.* Probabilistic Engineering Mechanics, 2014. **38**: p. 156-164.

58. Lazar, I.F., S.A. Neild, and D.J. Wagg, *Using an inerter-based device for structural vibration suppression.* Earthquake Engineering & Structural Dynamics, 2014. **43**(8): p. 1129-1147.
59. Hu, Y. and M.Z.Q. Chen, *Performance evaluation for inerter-based dynamic vibration absorbers.* International Journal of Mechanical Sciences, 2015. **99**: p. 297-307.
60. Pietrosanti, D., M. De Angelis, and M. Basili, *Optimal design and performance evaluation of systems with Tuned Mass Damper Inerter (TMDI).* Earthquake Engineering & Structural Dynamics, 2017. **46**(8): p. 1367-1388.
61. Eimani Kalehsar, H. and N. Khodaie, *Optimization of Response of a Dynamic Vibration Absorber Forming Part of the Main System by the Fixed-point Theory*. Vol. 22. 2017.
62. Mordorski, E.R., *Development of a Dynamic Torsional Actuator for Torque Converter Clutch Characterization*. 2018, Michigan Technological University.
63. Greiner, J. and M. Grumbach, *Automatic Transmission Systems Beyond 2020 - Challenges and Competition*. 2013, SAE International.
64. McGrath, M.H., Jeff; Bailey, George; George, Philip; Swank, Mike; Krause, Thorsten, *Torque Converters -Comfort and Fuel Economy in Tight Corners*, in *Luk Symposium*. 2006.
65. Robinette, D., et al., *Torque Converter Clutch Optimization: Improving Fuel Economy and Reducing Noise and Vibration*. 2011, SAE International.
66. *Mobility for tomorrow*. in *Schaeffler Symposium*. 2018. Baden-Baden, Germany: Schaeffler Technologies AG & Co. KG.
67. Gaillard, C.L. and R. Singh, *Dynamic analysis of automotive clutch dampers.* Applied Acoustics, 2000. **60**(4): p. 399-424.
68. Park, T., et al., *Dynamic Analysis of Damper System in Torque Converter*. 2007, SAE International.
69. Shi, W.K., et al., *The Influence of Torsional Damper Performance Parameter on Transmission System Torsional Vibration.* Applied Mechanics and Materials, 2012. **241-244**: p. 2015.
70. Li, Z. and J. Sandhu, *Transmission Torque Converter Arc Spring Damper Dynamic Characteristics for Driveline Torsional Vibration Evaluation*. 2013, SAE International.
71. Li, L. and R. Singh, *Analysis of vibration amplification in a multi-staged clutch damper during engine start-up.* Proceedings of the Institution of Mechanical Engineers, Part D: Journal of Automobile Engineering, 2014. **229**(10): p. 1406-1418.
72. Kabilan, V.S., et al., *Dynamics of a Single Degree of Freedom Clutch Damper System with Multiple Discontinuous Nonlinearities.* IOP Conference Series: Materials Science and Engineering, 2018. **310**: p. 012093.
73. Zink, M. and M. Hausner, *The centrifugal pendulum-type absorber.* ATZ worldwide, 2009. **111**(7): p. 42-47.
74. Lindemann, P., et al. *Torque Converters: Launching over new challenges*. in *Schaeffler Luk Symposium*. 2010.
75. Kooy, A. and J. Kroll. *Drive Train Vibrations: Solving the Conflict Between Efficiency and Drivability*. in *Proceedings of the FISITA 2012 World Automotive Congress*. 2013. Berlin, Heidelberg: Springer Berlin Heidelberg.
76. Jurmu, L., et al. *Measurement Methods for Evaluating the Frequency Response Function of a Torque Converter Clutch*. in *Rotating Machinery, Optical Methods & Scanning LDV Methods, Volume 6*. 2020. Cham: Springer International Publishing.

77. Kesy, Z. and A. Kesy, *Application of numerical methods to the modelling of transmission systems with hydrodynamic torque converter.* International Journal of Computer Applications in Technology, 2008. **31**(3-4): p. 275-283.
78. Adibi Asl, H., N. Lashgarian Azad, and J. McPhee, *Math-based torque converter modelling to evaluate damping characteristics and reverse flow mode operation.* International Journal of Vehicle Systems Modelling and Testing, 2014. **9**(1): p. 36-55.
79. Banerjee, J. and J. McPhee, *System dynamic modelling and simulation of hydrodynamic machines.* Mathematical and Computer Modelling of Dynamical Systems, 2016. **22**(1): p. 54-86.

A Appendix

A.1 Post Processing Time Data

Time data was acquired in LMS Test.Lab, and exported into .mat file format. The following Matlab script processes all of the acquired time domain measurements (acquired on one torque converter) into FRF measurements. Excitation frequencies change with the hardware tested.

```
% Time Data Post Processing
%
close all
clear
clc
%% Load data
Tin = load('Time_Tin_02_12_21.mat');
Sin = load('Time_Sin_02_12_21.mat');
Tout = load('Time_Tout_02_12_21.mat');
Sout = load('Time_Sout_02_12_21.mat');

%% convert to cell array
a = struct2cell(Tin);
b = struct2cell(Sin);
c = struct2cell(Tout);
d = struct2cell(Sout);
%% extract time vector, fft parameters
t = (a{1,1}.x_values.increment:a{1,1}.x_values.increment:...
    (a{1,1}.x_values.number_of_values-1)*a{1,1}.x_values.increment);
dt = t(2)-t(1);,fs = 1/dt;,df = 0.1;
%% excitation frequencies
freq = [(1:15)/5,4:7,(40:60)/5,13:20,22:2:100];
test = freq(1:30);
f_mat(:,1) = test';
f_mat(:,2) = freq(31:60)';
f_mat(:,3) = [freq(61:end),0,0]';
%% Organize time data into matrix format
for n = 1:length(a);
    tin(:,n) = a{n,1}.y_values.values(1:7680)'.*...
        a{n, 1}.y_values.quantity.unit_transformation.factor; % Nm
    sin(:,n) = b{n,1}.y_values.values(1:7680)'.*...
        b{n, 1}.y_values.quantity.unit_transformation.factor; % rpm
    tout(:,n) = c{n,1}.y_values.values(1:7680)'.*...
        c{n, 1}.y_values.quantity.unit_transformation.factor; % Nm
    sout(:,n) = d{n,1}.y_values.values(1:7680)'.*...
        d{n, 1}.y_values.quantity.unit_transformation.factor; % rpm
end
%% Calculate avg autopowers and cross powers
OL = 0.5; % percent overlap
Ntot = length(t);
N = 1/(df*dt); % length of each average
Neff = N*OL;
avg = (Ntot)/Neff; % number of averages
window = 'uniform';
```

```
for n = 1:length(a);
    [G_Tin(:,n),f] = AvgAutopower(tin(:,n),avg,N,Neff,fs,window); % Nm
    G_Tout(:,n) = AvgAutopower(tout(:,n),avg,N,Neff,fs,window);
    G_Sin(:,n) = AvgAutopower(sin(:,n),avg,N,Neff,fs,window);
    G_Sout(:,n) = AvgAutopower(sout(:,n),avg,N,Neff,fs,window);
    [G_tito(:,n),G_toti(:,n)] =
AvgCrossPower(tin(:,n),tout(:,n),avg,N,Neff,fs,window);
    [G_tiso(:,n),G_soti(:,n)] =
AvgCrossPower(tin(:,n),sout(:,n),avg,N,Neff,fs,window);
    [G_sito(:,n),G_tosi(:,n)] =
AvgCrossPower(sin(:,n),tout(:,n),avg,N,Neff,fs,window);
    [G_siso(:,n),G_sosi(:,n)] =
AvgCrossPower(sin(:,n),sout(:,n),avg,N,Neff,fs,window);
end
%% calculate FRFs
% H1 = Gio/Gii
ToTi_h1 = G_tito./G_Tin;% Tout/Tin
SoTi_h1 = G_tiso./G_Tin;% Sout/Tin
ToSi_h1 = G_sito./G_Sin;% Tout/Sin
SoSi_h1 = G_siso./G_Sin;% Sout/Sin
% H2 = Goo/Goi
ToTi_h2 = G_Tout./G_toti;% Tout/Tin
SoTi_h2 = G_Sout./G_soti;% Sout/Tin
ToSi_h2 = G_Tout./G_tosi;% Tout/Sin
SoSi_h2 = G_Sout./G_sosi;% Sout/Sin
%% Extract excitation frequency data points
Ti = sqrt(TC_extract(G_Tin,f_mat,f));
Si = sqrt(TC_extract(G_Sin,f_mat,f));
To = sqrt(TC_extract(G_Tout,f_mat,f));
So = sqrt(TC_extract(G_Sout,f_mat,f));

toti_h1 = TC_extract(ToTi_h1,f_mat,f);
soti_h1 = TC_extract(SoTi_h1,f_mat,f);
tosi_h1 = TC_extract(ToSi_h1,f_mat,f);
sosi_h1 = TC_extract(SoSi_h1,f_mat,f);

toti_h2 = TC_extract(ToTi_h2,f_mat,f);
soti_h2 = TC_extract(SoTi_h2,f_mat,f);
tosi_h2 = TC_extract(ToSi_h2,f_mat,f);
sosi_h2 = TC_extract(SoSi_h2,f_mat,f);
%% compute phase
phz_toti = unwrap(angle(toti_h2)).*180/pi;
phz_soti = unwrap(angle(soti_h2)).*180/pi;
phz_tosi = unwrap(angle(tosi_h2)).*180/pi;
phz_sosi = unwrap(angle(sosi_h2)).*180/pi;
%% compute frfs using the ratio of autopower spectra
toti = To./Ti;
tosi = To./Si;
soti = So./Ti;
sosi = So./Si;
siti = Si./Ti;
tisi = Ti./Si;
%% plot results
figure
```

```
subplot(2,4,1)
semilogy(freq,abs(toti_h1),'k--o',freq,abs(toti_h2),'r--.',...
    freq,toti),grid on
ylabel('Tout/Tin')

subplot(2,4,2)
semilogy(freq,abs(soti_h1),'k--o',freq,abs(soti_h2),'r--.',...
    freq,soti),grid on
ylabel('Sout/Tin (rpm/Nm)')
subplot(2,4,3)
semilogy(freq,abs(tosi_h1),'k--o',freq,abs(tosi_h2),'r--.',...
    freq,tosi),grid on
ylabel('Tout/Sin (Nm/rpm)')

subplot(2,4,4)
semilogy(freq,abs(sosi_h1),'k--o',freq,abs(sosi_h2),'r--.',...
    freq,sosi),grid on
ylabel('Sout/Sin')

subplot(2,4,5)
plot(freq,phz_toti,'b-'),grid on

subplot(2,4,6)
plot(freq,phz_soti,'b-'),grid on

subplot(2,4,7)
plot(freq,phz_tosi,'b-'),grid on

subplot(2,4,8)
plot(freq,phz_sosi,'b-'),grid on
%% plot autopowers
figure
semilogy(freq,Ti)
%% save frf data
save('FileName','toti','tosi','soti','sosi',...
    'phz_toti','phz_tosi','phz_soti','phz_sosi','Ti','To','Si','So',...
    'freq')
```

The above test script use three custom functions: TC_extract.m, AvgAutopower.m, and AvgCrossPower.m. Their respective codes are shown below.

A.1.1 TC_extract Function

```
function [Extract] = TC_extract(data,test,f)
%
y = size(data);

for n = 1:y(2);
    index1 = find(f<=test(n,1)+.01&f>=test(n,1)-.01);
    index2 = find(f<=test(n,2)+.01&f>=test(n,2)-.01);
    index3 = find(f<=test(n,3)+.01&f>=test(n,3)-.01);
    x1(n) = data(index1,n);
    x2(n) = data(index2,n);
```

```
    x3(n) = data(index3,n);
end

Extract = [x1, x2, x3(1:28)];
end
```

A.1.2 AvgAutopower Function

```
function [result,f] = AvgAutopower(time,avg,N,Neff,Fs,window)
% Calculates averaged autopower spectrum.
% Input column vector of time data, # of averages,
% and actual and effective lengths of each average.
Ntot = length(time);

% Reshape data for averaging.
Newin_1 = reshape(time,[N,Ntot/N]);
in2 = time(Neff+1:end-Neff);
Newin_2 = reshape(in2,[N,length(in2)/N]);
in_new = [Newin_1,Newin_2];
% Create window matrix.
x = size(in_new);
switch window
    case 'hanning'
        win = hann(N);
        W = repmat(win,[1,avg]);
        acf = 1/mean(win);
    case 'uniform'
        win = ones(N,1);
        W = repmat(win,[1,avg]);
        acf = 1/mean(win);
    case 'flattop'
        win = flattopwin(N);
        W = repmat(win,[1,avg]);
        acf = 1/mean(win);
end

% apply window and compute one sided linear spectra.
Winput = in_new.*win;
[Gi,f] = DSP_fft(Winput,Fs);
Gi = Gi.*acf;
% Compute averaged auto power
Gxx = conj(Gi).*Gi;
if avg>1
    result = mean(Gxx');
else
    result = Gxx;
end
end
```

A.1.3 AvgCrossPower Function

```
function [result1,result2,f] =
AvgCrossPower(time1,time2,avg,N,Neff,Fs,window)
```

```
% Calculates averaged crosspower spectrum.
% Input column vector of time data, # of averages,
% and actual and effective lengths of each average.
Ntot1 = length(time1);
Ntot2 = length(time2);

%% Reshape data for averaging.
Newin_1 = reshape(time1,[N,Ntot1/N]);
in2 = time1(Neff+1:end-Neff);
Newin_2 = reshape(in2,[N,length(in2)/N]);
in_new1 = [Newin_1,Newin_2];

Newin_1 = reshape(time2,[N,Ntot2/N]);
in2 = time2(Neff+1:end-Neff);
Newin_2 = reshape(in2,[N,length(in2)/N]);
in_new2 = [Newin_1,Newin_2];
%% Create window matrix.
switch window
    case 'hanning'
        win = hann(N);
        W = repmat(win,[1,avg]);
        acf = 1/mean(win);
    case 'uniform'
        win = ones(N,1);
        W = repmat(win,[1,avg]);
        acf = 1/mean(win);
    case 'flattop'
        win = flattopwin(N);
        W = repmat(win,[1,avg]);
        acf = 1/mean(win);
end
% apply window and compute one sided linear spectra.
Winput1 = in_new1.*win;
Winput2 = in_new2.*win;
[Gi,f] = DSP_fft(Winput1,Fs);
Go = DSP_fft(Winput2,Fs);
Gi = Gi.*acf;
Go = Go.*acf;
%% Compute averaged cross powers
Goi = conj(Go).*Gi;
Gio = conj(Gi).*Go;

if avg>1
    result1 = mean(Gio');
    result2 = mean(Goi');
else
    result1 = Gio;
    result2 = Goi;
end
end
```

A.1.4 DSP_fft Function

```
function [result,f] = DSP_fft(timeData,fs)
```

```
x = size(timeData);
N = x(1);
a = mod(N,2);
df = fs/N;
switch a
    case 0
        P = fft(timeData)/N;
        result = P(1:N/2+1,:);
        result(2:end,:) = result(2:end,:)*2;
        f = [0:N/2]*df;
    otherwise
        P = fft(timeData)/N;
        result = P(1:(N+1)/2,:);
        result(2:end,:) = result(2:end,:)*2;
        f = [0:(N-1)/2]*df;
end
end
```

A.2 Post Processing Model Data

Amesim software was used to simulate the torsional response of the hardware models. Time domain data was exported from the Amesim model in .data file format. The model data was then post processed into FRFs and compared to test FRFs.

```
% AMESIM Correlation
close all
clear
clc
%%
speed = 2000;
% Read AMESIM Time data.
Torque = dlmread(['Tin_Tout_',num2str(speed),'rpm.data'],'',3,0);
Speed = dlmread(['Sin_Sout_',num2str(speed),'rpm.data'],'',3,0);
% Torque = dlmread(['Tin_Tout_',num2str(speed),'rpm_a.data'],'',3,0);
% Speed = dlmread(['Sin_Sout_',num2str(speed),'rpm_a.data'],'',3,0);

z = find(Torque(:,1)==6);
dt = Torque(2,1)-Torque(1,1);
fs = 1/dt;
 % set boundary condition
test = [(1:15)/5,4:7,(40:50)/5];
%% Truncate Data
t = [6:dt:26];
Torque = Torque(z+1:end,2:end);
Speed = Speed (z+1:end,2:end);
Tin = Torque(:,1:30);
Tout = Torque(:,31:end);
Sin = Speed(:,1:30);
Sout = Speed(:,31:end);
x = size(Tin);
%% Calculate avg autopowers
OL = .5; % 50% overlap
Ntot = x(1);
N = 1280; % length of each average
Neff = N*OL;
```

```
avg = (Ntot)/Neff-1; % number of averages
for n = 1:length(test)
    [G_Tin(:,n),f] = AvgAutopower(Tin(:,n),avg,N,Neff,fs);
    G_Tout(:,n) = AvgAutopower(Tout(:,n),avg,N,Neff,fs);
    G_Sin(:,n) = AvgAutopower(Sin(:,n),avg,N,Neff,fs);
    G_Sout(:,n) = AvgAutopower(Sout(:,n),avg,N,Neff,fs);
    [G_Tio(:,n),G_Toi(:,n)] =
AvgCrossPower(Tin(:,n),Tout(:,n),avg,N,Neff,fs);
    [G_Sio(:,n),G_Soi(:,n)] =
AvgCrossPower(Tin(:,n),Sout(:,n),avg,N,Neff,fs);
    [G_sito(:,n),G_tosi(:,n)] =
AvgCrossPower(Sin(:,n),Tout(:,n),avg,N,Neff,fs);
    [G_siso(:,n),G_sosi(:,n)] =
AvgCrossPower(Sin(:,n),Sout(:,n),avg,N,Neff,fs);
end
% Calculate coherence
CohT = (G_Tio.*G_Toi)./(G_Tin.*G_Tout);
CohS = (G_Sio.*G_Soi)./(G_Tin.*G_Sout);
% Take sqrt of autopowers
G_Tin = sqrt(G_Tin);
G_Tout = sqrt(G_Tout);
G_Sin = sqrt(G_Sin);
G_Sout = sqrt(G_Sout);
% Calculate phase
phz_toti = angle(G_Tio);
phz_soti = angle(G_Sio);
phz_sosi = angle(G_siso);
phz_tosi = angle(G_sito);
% calculate TR, SR, and K factor
% TR = mean(G_Tout(1,:)./G_Tin(1,:));
% SR = mean(G_Sout(1,:)./G_Sin(1,:));
% K = mean(G_Sin(1,:)./sqrt(G_Tin(1,:)));
%% Calculate FRFs, Coherence, Phase
f_mat = test';
f_mat(:,2) = [(51:60)/5,13:20,22:2:44]';
f_mat(:,3) = [46:2:100,0,0]';

[toti, soti, Ti, To, So] = TC_FRFs(G_Tin, G_Tout,G_Sout,f_mat,f);
[sosi, tosi, Si, ~, ~] = TC_FRFs(G_Sin, G_Sout,G_Tout,f_mat,f);
freq = [f_mat(:,1)',f_mat(:,2)',f_mat(:,3)'];
[CohT] = TC_Coh(CohT,f_mat,f);
[CohS] = TC_Coh(CohS,f_mat,f);
[phz_toti] = TC_Coh(phz_toti,f_mat,f);
[phz_soti] = TC_Coh(phz_soti,f_mat,f);
[phz_sosi] = TC_Coh(phz_sosi,f_mat,f);
[phz_tosi] = TC_Coh(phz_tosi,f_mat,f);

% sort data
[freq2,I] = sort(freq);
toti = toti(I);
soti = soti(I);
Ti = Ti(I);
To = To(I);
Si = Si(I);
```

```
So = So(I);
CohT = CohT(I);
CohS = CohS(I);
phz_toti = phz_toti(I);
phz_soti = phz_soti(I);
phz_sosi = phz_sosi(I);
phz_tosi = phz_tosi(I);
% get rid of 0 freq points
freq = freq2(2:end);
toti = toti(2:end);
soti = soti(2:end);
Ti = Ti(2:end);
To = To(2:end);
Si = Si(2:end);
So = So(2:end);
CohT = CohT(2:end);
CohS = CohS(2:end);
phz_toti = phz_toti(2:end);
phz_soti = phz_soti(2:end);
phz_sosi = phz_sosi(2:end);
phz_tosi = phz_tosi(2:end);
phz_toti = unwrap(phz_toti).*(180/pi);
phz_soti = unwrap(phz_soti).*(180/pi);
phz_sosi = unwrap(phz_sosi).*(180/pi);
phz_tosi = unwrap(phz_tosi).*(180/pi);
%% Load appropriate Data set and save processed model data
switch speed
    case 500
        Exp = load('testData.mat');
        save('filename','toti','soti','sosi','tosi','phz_toti',...
            'phz_soti','phz_sosi','phz_tosi','CohT','CohS',...
            'Ti','To','Si','So','freq');
    case 1000
        Exp = load('testData.mat');
        save('filename','toti','soti','sosi','tosi','phz_toti',...
            'phz_soti','phz_sosi','phz_tosi','CohT','CohS',...
            'Ti','To','Si','So','freq');
    case 1500
        Exp = load('testData.mat');
        save('filename','toti','soti','sosi','tosi','phz_toti',...
            'phz_soti','phz_sosi','phz_tosi','CohT','CohS',...
            'Ti','To','Si','So','freq');
    case 2000
        Exp = load('TestData.mat');
        save('filename','toti','soti','sosi','tosi','phz_toti',...
            'phz_soti','phz_sosi','phz_tosi','CohT','CohS',...
            'Ti','To','Si','So','freq');
    otherwise
        disp('Choose Valid Output Speed');
end
%% Make plots for comparison
a = 0;
b = 100;
figure
```

```
subplot(2,1,1)
semilogy(Exp.freq,Exp.toti,'k*-.',freq,toti,'r*-.'),grid on
xlabel('Frequency (Hz)')
ylabel('Output Torque / Input Torque')
title(['Hardware: ',num2str(speed),' rpm'])
legend('Exp','Model')
xlim([a b])
subplot(2,1,2)
plot(Exp.freq,Exp.phz_toti,'k*-.',freq,phz_toti,'r*-.'),grid on
xlabel('Frequency (Hz)')
ylabel('Phase (Deg)')
xlim([a b])

figure
subplot(2,1,1)
semilogy(Exp.freq,Exp.soti,'k*-.',freq,soti,'r*-.'),grid on
xlabel('Frequency (Hz)')
ylabel('Output Speed / Input Torque (rpm/Nm)')
title(['Hardware: ',num2str(speed),' rpm'])
legend('Exp','Model')
xlim([a b])
subplot(2,1,2)
plot(Exp.freq,Exp.phz_soti,'k*-.',freq,phz_soti,'r*-.'),grid on
xlabel('Frequency (Hz)')
ylabel('Phase (Deg)')
xlim([a b])
%% plot autopowers
figure
subplot(2,2,1)
semilogy(Exp.freq,Exp.Ti,'k*-.',freq,Ti,'r*-.'),grid on
xlabel('Frequency (Hz)')
ylabel('Nm')
title('Input Torque')
subplot(2,2,2)
semilogy(Exp.freq,Exp.Si,'k*-.',freq,Si,'r*-.'),grid on
xlabel('Frequency (Hz)')
ylabel('Nm')
title('Input Speed')
subplot(2,2,3)
semilogy(Exp.freq,Exp.To,'k*-.',freq,To,'r*-.'),grid on
xlabel('Frequency (Hz)')
ylabel('Nm')
title('Output Torque')
subplot(2,2,4)
semilogy(Exp.freq,Exp.So,'k*-.',freq,So,'r*-.'),grid on
xlabel('Frequency (Hz)')
ylabel('Nm')
title('Output Speed')
```

Similar to the test data post processing, AvgAutopower and AvgCrossPower functions were used in processing the Amesim data. Other functions that were used include TC_FRFs.m and TC_Coh.m.

A.2.1 TC_FRFs Function

```
function [TFRF, SFRF, Ti, To, So] = TC_FRFs(data1,data2,data3,f_mat,f)
% Outputs Torque ratio frf and speed/torque frf.


for n = 1:length(f_mat)
    index_f1(n) = find(f<f_mat(n,1)+.01 & f>f_mat(n,1)-.01);
    index_f2(n) = find(f<f_mat(n,2)+.01 & f>f_mat(n,2)-.01);
    index_f3(n) = find(f<f_mat(n,3)+.01 & f>f_mat(n,3)-.01);
    Ti1(n) = data1(index_f1(n),n);
    To1(n) = data2(index_f1(n),n);
    So1(n) = data3(index_f1(n),n);
    Ti2(n) = data1(index_f2(n),n);
    To2(n) = data2(index_f2(n),n);
    So2(n) = data3(index_f2(n),n);
    Ti3(n) = data1(index_f3(n),n);
    To3(n) = data2(index_f3(n),n);
    So3(n) = data3(index_f3(n),n);
end

Ti = [Ti1,Ti2,Ti3];
To = [To1,To2,To3];
So = [So1,So2,So3];
TFRF = To./Ti; % Nm/Nm
SFRF = So./Ti; % rpm/Nm
end
```

A.2.2 TC_Coh Function

```
function [Coherence] = TC_Coh(Coh,test,f)
%
x = size(test);

for n = 1:x(1)
    index_f1(n) = find(f<=test(n,1)+.01&f>=test(n,1)-.01);
    index_f2(n) = find(f<=test(n,2)+.01&f>=test(n,2)-.01);
    index_f3(n) = find(f<=test(n,3)+.01&f>=test(n,3)-.01);
    x1(n) = Coh(index_f1(n),n);
    x2(n) = Coh(index_f2(n),n);
    x3(n) = Coh(index_f3(n),n);
end

Coherence = [x1,x2,x3];
end
```

A.3 Generating Test Scripts

The torque converter test cell has the capability to run automated test scripts. Unique test scripts were written for each device under test using another Matlab script. The torque converter test cell runs on a LabVIEW program, and the test scripts are written in a .tc file format. In the Matlab script, the user selects the frequency vector of excitation, the number of sine tones per measurement, tone spacing, the amplitude of each dynamic torque, mean torque, operating speed, clutch state, the time between test points, and the

time at each test point. The test script is then automatically written using the following Matlab code.

```
% Create automated test scripts from user defined test conditions and
test
% points.
clear
clc
close all
%% Test Conditions
name = 'ScriptTitle.tc';
clutch = 1; % 1:locked, 0:open
spacing = 1; % 1:spaced freqs, 0:sequential freqs

freqs = [1:7,(40:60)/5,13:27,(140:160)/5,33:40,42:2:100]; % Hardware
specific
phase = round(rand(1,length(freqs))*359); % degrees
%phase = zeros(1,length(freqs));
tones = 3;
ACtrq = 20;
speed = 905;
Meantrq = 150;
% load tp time
t_L = 10; % seconds
% tp time
t_T = 15; % seconds
%% Open appropriate file
switch clutch
    case 1
        [FID,msg] = fopen('Locked_TC_Torsional_200F.tc','r+');
        A = fread(FID,'*char')';
        fclose(FID);
        % Figure out step architecture
        start = strfind(A,'<Name>Program Item</Name>');
        start = start-11;
        load_tp = A(start(13):start(14)-3);
        tp = A(start(14):start(15)-3);
        startup = A(1:start(13)-3);
        shutdown = A(start(15):end);
    case 0
        [FID,msg] = fopen('Open_TC_Torsional.tc','r+');
        A = fread(FID,'*char')';
        fclose(FID);
        % Figure out step architecture
        start = strfind(A,'<Name>Program Item</Name>');
        start = start-11;
        load_tp = A(start(11):start(12)-3);
        tp = A(start(12):start(13)-3);
        startup = A(1:start(11)-3);
        shutdown = A(start(13):end);
end
%% modify the speed value in the startup and shutdown scripts
% startup script
start = Startup(startup,speed,Meantrq,clutch);
```

```
% shutdown script
stop = Shutdown(shutdown,speed,Meantrq,clutch);
% load and test scripts
tp1 = load_tp;
tp2 = tp;
%% Create test matrix
N = ceil(length(freqs)/tones); % compute number of test points
fmat = zeros(N,tones);
pmat = zeros(N,tones);
j = 1;
switch spacing
    case 1 % Tones spaced
        for n = 1:tones
            if (j+N-1)>length(freqs)
                x = length(freqs(j:end));
                fmat(1:x,n) = freqs(j:end)';
                pmat(1:x,n) = phase(j:end)';
            else
                fmat(:,n) = freqs(j:j+N-1)';
                pmat(:,n) = phase(j:j+N-1)';
            end
            j = j+N;
        end
    case 0 % Tones not spaced
        for n = 1:N
            if (j+tones-1)>length(freqs)
                x = length(freqs(j:end));
                fmat(n,1:x) = freqs(j:end);
                pmat(n,1:x) = phase(j:end);
            else
                fmat(n,:) = freqs(j:j+tones-1);
                pmat(n,:) = phase(j:j+tones-1);
            end
            j = j+tones;
        end
end
%% custom fmat
%fmat = [];
%% generate test points for script and create complete test script
middle = '';
for n = 1:N
    TP =
psuedo(tp1,tp2,ACtrq,Meantrq,speed,fmat(n,:),pmat(n,:),t_L,t_T);
    TP = strrep(TP,'LoadTest pt 1',['LoadTest pt ',num2str(n)]);
    TP = strrep(TP,'>Test pt 1',['>Test pt ',num2str(n)]);
    middle = [middle,TP,sprintf('\r')];
end
% end torsional
a = strfind(stop,'Send Trigger');a = a(1);
b = strfind(stop,'</Cluster>');b = b+10;
c = find(b>a);c = c(1);
X = stop(1:b(c));
stop = stop(b(c)+2:end);
```

```
torend =
psuedo(X,tp2,0,Meantrq,speed,zeros(1,tones),zeros(1,tones),t_L,t_T);
a = strfind(torend,'Send Trigger');a = a(1);
b = strfind(torend,'</Cluster>');b = b+10;
c = find(b>a);c = c(1);
torend = torend(1:b(c));

new = [start,sprintf('\r'),middle,torend,stop];
num = strfind(new,'Step Name');num = length(num);
D1 = strfind(new,'<Dimsize>'); D1 = D1(1)+8;
D2 = strfind(new,'</Dimsize>'); D2 = D2(1);
% new(D1:D2) = strrep(new(D1:D2),new(D1:D2),num2str(num));
new = replaceBetween(new,new(1:D1),new(D2:end),num2str(num));
%% create test script file
fid = fopen(name,'w');
fwrite(fid,new);
fclose(fid);
```

A.3.1 Startup function

```
function [new] = Startup(startup,speed,Meantrq,clutch)
% create startup script
switch clutch
    case 1
        val = strfind(startup,'<Val>');val = val+4;
        valEnd = strfind(startup,'</Val>');
        abs = strfind(startup,'Abs. Dyno');abs = abs(11);
        s = find(val>abs);s = s(1);
        x = strfind(startup,'Load Dyno System 1');
        y = strfind(startup,'Load Dyno System 2');
        z = strfind(startup,'Apply Clutch');
        start =
replaceBetween(startup,startup(z:val(s)),startup(valEnd(s):x+18),...
            num2str(speed,'%.14f'));
        val = strfind(start,'<Val>');val = val+4;
        valEnd = strfind(start,'</Val>');
        abs = strfind(start,'Abs. Dyno');abs = abs(12);
        s = find(val>abs);s = s(1);
        start =
replaceBetween(start,start(x:val(s)),start(valEnd(s):y+18),...
            num2str(speed,'%.14f'));
        val = strfind(start,'<Val>');val = val+4;
        valEnd = strfind(start,'</Val>');
        d = strfind(start,'Drive Dyno');d = d(12);
        s = find(val>d);s = s(1);
        new =
replaceBetween(start,start(x:val(s)),start(valEnd(s):y+18),...
            num2str(Meantrq,'%.14f'));
    case 0
        val = strfind(startup,'<Val>');val = val+4;
        valEnd = strfind(startup,'</Val>');
        abs = strfind(startup,'Abs. Dyno');abs = abs(10);
        s = find(val>abs);s = s(1);
        x = strfind(startup,'Dyno System SS');
        y = strfind(startup,'Load Dyno System');
```

```
        start =
replaceBetween(startup,startup(x:val(s)),startup(valEnd(s):y+16),...
            num2str(speed,'%.14f'));
        val = strfind(start,'<Val>');val = val+4;
        valEnd = strfind(start,'</Val>');
        d = strfind(start,'Drive Dyno');d = d(10);
        s = find(val>d);s = s(1);
        new =
replaceBetween(start,start(x:val(s)),start(valEnd(s):y+18),...
            num2str(Meantrq,'%.14f'));
end

end
```

A.3.2 Shutdown Function

```
function [new] = Shutdown(shutdown,speed,Meantrq,clutch)
switch clutch
    case 1
        val = strfind(shutdown,'<Val>');val = val+4;
        valEnd = strfind(shutdown,'</Val>');
        abs = strfind(shutdown,'Abs. Dyno');abs = abs(1);
        s = find(val>abs);s = s(1);
        x = strfind(shutdown,'End Torsional');
        shutdown =
replaceBetween(shutdown,shutdown(abs:val(s)),shutdown(valEnd(s):x+16),.
..
            num2str(speed,'%.14f'));
        val = strfind(shutdown,'<Val>');val = val+4;
        valEnd = strfind(shutdown,'</Val>');
        d = strfind(shutdown,'Drive Dyno');d = d(1);
        s = find(val>d);s = s(1);
        new =
replaceBetween(shutdown,shutdown(d:val(s)),shutdown(valEnd(s):x+16),...
            num2str(Meantrq,'%.14f'));
    case 0
        val = strfind(shutdown,'<Val>');val = val+4;
        valEnd = strfind(shutdown,'</Val>');
        abs = strfind(shutdown,'Abs. Dyno');abs = abs(1);
        s = find(val>abs);s = s(1);
        x = strfind(shutdown,'End Torsional');
        shutdown =
replaceBetween(shutdown,shutdown(abs:val(s)),shutdown(valEnd(s):x+16),.
..
            num2str(speed,'%.14f'));
        val = strfind(shutdown,'<Val>');val = val+4;
        valEnd = strfind(shutdown,'</Val>');
        d = strfind(shutdown,'Drive Dyno');d = d(1);
        s = find(val>d);s = s(1);
        new =
replaceBetween(shutdown,shutdown(d:val(s)),shutdown(valEnd(s):x+16),...
            num2str(Meantrq,'%.14f'));
end

end
```

A.3.3 pseudo Function

```
function [new] = psuedo(tp1,tp2,ACtrq,Meantrq,speed,freq,phase,t_L,t_T)
% generate test point for psuedo random method
%% extract begining and end of test point scripts
val = strfind(tp1,'<Val>');val = val+5;
valEnd = strfind(tp1,'</Val>');valEnd = valEnd-1;
tones = strfind(tp1,'<Name>Tones</Name>');tones = tones(1);
m = strfind(tp1,'<Name>Mode</Name>');m = m(2);
L_start = tp1(1:tones-1);
L_stop = tp1(m:end);
tones = strfind(tp2,'<Name>Tones</Name>');tones = tones(1);
m = strfind(tp2,'<Name>Mode</Name>');m = m(2);
T_start = tp2(1:tones-1);
T_stop = tp2(m:end);
%% define tone script
Num = length(freq);
t = tp2(tones:m-1);
t = replaceBetween(t,'<Dimsize>','</Dimsize>',num2str(Num));
a = strfind(t,'</Dimsize>');a = a+10;
b = strfind(t,'</Cluster>');b = b(1)+10;
c = strfind(t,'</Array>'); c = c(end);
begin = t(1:a);
tone = t(a+2:b);
last = t(c:end);
%% create tones
sig = '';
for n = 1:Num
    v = strfind(tone,'<Val>');v = v+4;
    vEnd = strfind(tone,'</Val>');
    f = strfind(tone,'<Name>Frequency</Name>');
    i = find(v>f);i = i(1);
    L =
replaceBetween(tone,tone(f:v(i)),tone(vEnd(i):end),num2str(freq(n),'%.1
4f'));
    v = strfind(L,'<Val>');v = v+4;
    vEnd = strfind(L,'</Val>');
    p = strfind(L,'<Name>Phase</Name>');
    i = find(v>p);i = i(1);
    L =
replaceBetween(L,L(p:v(i)),L(vEnd(i):end),num2str(phase(n),'%.14f'));
    v = strfind(L,'<Val>');v = v+4;
    vEnd = strfind(L,'</Val>');
    a = strfind(tone,'<Name>Amplitude</Name>');
    i = find(v>a);i = i(1);
    if freq(n)==0
        ACtrq = 0;
    end
    L =
replaceBetween(L,L(a:v(i)),L(vEnd(i):end),num2str(ACtrq,'%.14f'));
    sig = [sig,L];
end
sig = [begin,sig,last];
%% load test point script
v = strfind(L_start,'<Val>');v = v+4;
```

```
vEnd = strfind(L_start,'</Val>');
A = strfind(L_start,'<Name>Drive Dyno</Name>');
a = find(v>A);a = a(1);
L_start =
replaceBetween(L_start,L_start(A:v(a)),L_start(vEnd(a):end),num2str(Mea
ntrq,'%.14f'));
v = strfind(L_start,'<Val>');v = v+4;
vEnd = strfind(L_start,'</Val>');
A = strfind(L_start,'<Name>Time delta (s)</Name>');
a = find(v>A);a = a(1);
L_start =
replaceBetween(L_start,L_start(A:v(a)),L_start(vEnd(a):end),num2str(t_L
,'%.14f'));
v = strfind(L_stop,'<Val>');v = v+4;
vEnd = strfind(L_stop,'</Val>');
A = strfind(L_stop,'<Name>Abs. Dyno</Name>');
a = find(v>A);a = a(1);
L_stop =
replaceBetween(L_stop,L_stop(A:v(a)),L_stop(vEnd(a):end),num2str(speed,
'%.14f'));
Load = [L_start,sig,L_stop];
%% test point script
v = strfind(T_start,'<Val>');v = v+4;
vEnd = strfind(T_start,'</Val>');
A = strfind(T_start,'<Name>Drive Dyno</Name>');
a = find(v>A);a = a(1);
T_start =
replaceBetween(T_start,T_start(A:v(a)),T_start(vEnd(a):end),num2str(Mea
ntrq,'%.14f'));
v = strfind(T_start,'<Val>');v = v+4;
vEnd = strfind(T_start,'</Val>');
A = strfind(T_start,'<Name>Time delta (s)</Name>');
a = find(v>A);a = a(1);
T_start =
replaceBetween(T_start,T_start(A:v(a)),T_start(vEnd(a):end),num2str(t_T
,'%.14f'));
v = strfind(T_stop,'<Val>');v = v+4;
vEnd = strfind(T_stop,'</Val>');
A = strfind(T_stop,'<Name>Abs. Dyno</Name>');
a = find(v>A);a = a(1);
T_stop =
replaceBetween(T_stop,T_stop(A:v(a)),T_stop(vEnd(a):end),num2str(speed,
'%.14f'));
Test = [T_start,sig,T_stop];
%%
new = [Load,Test];
end
```